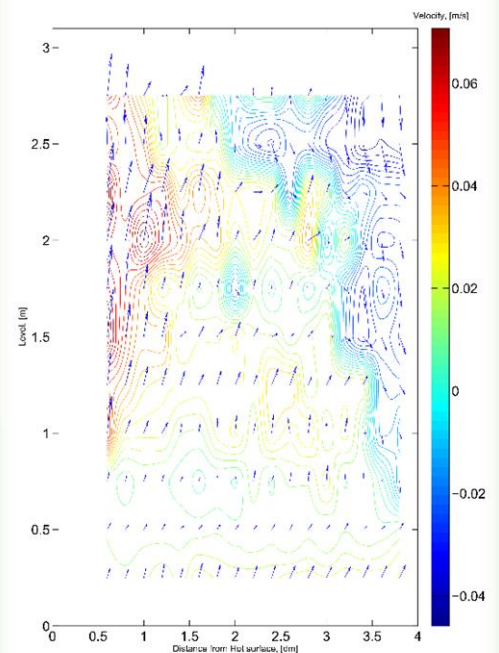
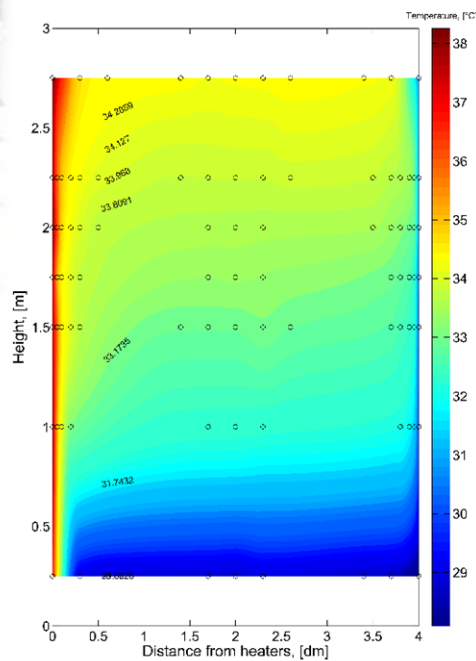


Flow nature inside vertical asymmetrically heated channel

Master Thesis Project



School of Engineering and Science,
Aalborg University – Denmark

Indoor Environmental and Energy
Engineering

Written by:

Nikol Todorova

Radi Dimitrov

Aalborg University
Engineering and Science
Sofiendalsvej 9-11
9200 Aalborg SV
Phone No.: 99 40 84 84
<http://www.byggeri.aau.dk>

Title: Flow nature inside vertical
asymmetrically heated channel

Synopsis:

Project period: 01.09.2015 - 09.06.2016

Authors:

Nikol Todorova
Radi Dimitrov

Supervisors:

Olena Kalyanova
Li Liu

Report pages: 124

Appendix pages: 23

Completed: 09.06.2016

The project examines turbulent natural convection flow in an asymmetrically heated, vertical, non-convergent channel. The work is performed on a scaled experimental setup of a Double Skin Facade, located in laboratory conditions. The analysis focuses on measurements of the thermal and velocity profiles inside the cavity. Experiments are done based on one factor at a time variation, allowing observation of the parameters influence on the flow. Dimensionless numbers are used for classification of the flow and convection regimes. The analysis aims to link possible recirculation phenomenon, with specific boundary conditions.

The content of the report is available but the publication can only happen in agreement with the authors.

Preface

The idea for this report came from the necessity of proper prediction of the flow phenomena in a Double Skin Facade. It is not a rare case that DSF are build with intention to minimize energy uses and increase the comfort, but in the process of work the facade just does not perform as expected. The problem comes from the aim to make it free convection ventilated, which by default is highly dependent on the ambient conditions. The variation of wind forces, temperature at the surfaces and inlet temperature are shown in many studies as relevant for the unstable behavior of the flow in the cavity of a DSF. Therefore, those parameters are chosen as leading in the current report. The aim is simply to determine why and under which conditions the existence of flow irregularities occur.

This report is written by Nikol Todorova and Radi Dimitrov, master students in Indoor Environmental and Energy Engineering at Aalborg University. The project documentation consists of a printed report and a flash drive, which could be found attached to the last page of the report. The flash drive contains all plots and video footages produced for the project. The flash drive content list is included in the report's appendix.

Special acknowledgments should be given to the supervisors of this project - Olena Kalyanova Larsen and Li Liu for their guidance and useful advices during the empirical and analytical work of this project. Their efforts helped to highlight important statements and improve the presentation of the results. The authors would like to thank also to Hicham Johra for his competent and timely help with experiments and experimental equipment.

Nikol Todorova

Radi Dimitrov

Abstract

In this report is present a study of a flow nature inside vertical, asymmetrically heated, non-convergent channel. The measured variables are temperatures and velocities inside the cavity. The purpose of the work is to contribute to the understanding of the flow patterns inside enclosed channels and more specifically to Double-Skin facade structures, with supply and exhaust openings located at the vertical surfaces.

A literature review is done, where dimensionless criteria for the characterization of the flow are derived. Based on them all of the experiments are confirmed to result in turbulent natural convection driven flow. The literature review serves also as prerequisite for the assumption of two-dimensional flow inside the cavity, which facilitates the experimental procedure.

To obtain overview and basic knowledge about the physical process and flow patterns inside the cavity is performed a video capturing before the actual experiments. These videos enrich the understanding and help to clarify unexpected flow patterns.

Specific flow structures are examined in a vertical 2D plane, where the focus is set to the boundary layers development on both hot and cold surfaces and in the top part of the experimental cavity. According to literature the current case is characterized as a wide cavity, where the boundary layers along the surfaces are developing separately from each other. Simultaneously, the general flow pattern is connecting the two boundary layers in a global recirculating flow.

To summarize the results from the presented experiments is derived a statement, which generalizes the observed processes of flow movement inside the cavity.

Table of contents

Preface	iii
Abstract	v
Chapter 1 Introduction	1
I Theory and literature review	3
Chapter 2 Physical processes and dimensionless numbers	5
2.1 Free and forced convection principle	5
2.1.1 Free convection principle	5
2.1.2 Forced convection principle	6
2.2 Convection boundary layers	7
2.2.1 Velocity boundary layer	7
2.2.2 Thermal boundary layer	9
2.2.3 Boundary layer influence on a flow	10
2.3 Dimensionless numbers	11
Chapter 3 Purpose and applicability of DSF	15
3.1 Double skin emergence in buildings design	15
3.2 DSF classification	15
3.3 Advantages and disadvantages of Double Skin Facades	17
3.3.1 Disadvantages of DSF constructions	17
3.3.2 Advantages of Double Skin Facades	17
Chapter 4 Flow between parallel vertical plates	19
II Experimental study	30
Chapter 5 Problem formulation	31
Chapter 6 Experimental set up	33
6.1 Geometry	33
6.2 Equipment	34
6.3 Boundary conditions	39
Chapter 7 Experimental results and analysis	43

7.1	Baseline experiment	49
7.1.1	Video flow visualization	51
7.1.2	Temperature distribution	54
7.1.3	Velocity distribution	60
7.1.4	Dimensionless analysis	70
7.2	Comparison group one - air-change rate variation	71
7.2.1	Temperature distribution	72
7.2.2	Velocity distribution	74
7.2.3	Dimensionless analysis	87
7.3	Comparison group two - surface temperature variation	87
7.3.1	Temperature distribution	88
7.3.2	Velocity distributions	92
7.3.3	Dimensionless criteria	102
7.4	Comparison group three inlet temperature variation	103
7.4.1	Temperature distribution	103
7.4.2	Velocity distribution	105
7.4.3	Dimensionless analysis	111
7.5	Summary of experimental results	112
 III Conclusion and discussion		116
Chapter 8 Limitations		117
Chapter 9 Proposals for further work		119
Chapter 10 Conclusion		121
Bibliography		123
 IV Appendix		125
Appendix A Temperature Measurements		
A.1	Thermocouples and PT100 Sensors Calibration	126
A.2	Thermocouples location	128
Appendix B Velocity Measurements characteristics		
B.1	Laser Doppler Anemometry Performance Principle	129
B.2	Orifice plate regression curve	131
Appendix C Experimental setup pictures		
Appendix D Experimental results - Air-change rate variation		
D.1	Temperature distributions	134
D.2	Velocities distributions	136
D.3	Pressure difference histograms	137
Appendix E Experimental results - Hot surface temperature variation		

E.1	Temperature distributions	138
E.2	Velocities distributions	139
E.3	Pressure difference	140

Appendix F Experimental results - Inlet temperature variation

F.1	Velocities distributions	142
F.2	Pressure difference	143

Appendix G Dry air properties

Appendix H Electronic appendix

Introduction

1

Double Skin Facades are known under different names - Dynamic facade, Energy saving facade, Wall-Filter facade etc., but in all cases it means multiple layers of glass surface facades serving for reduction of energy consumption, sound insulation or ventilation. The most common structures consist of two layers of glazing, with intermediate distance from 0.20 m to more than 2.00 m.

The Double Skin Facade (DSF) concept is not recent, but during the past decades has become an intensively discussed topic. The interest is more visible in Europe and especially in the Nordic countries. The economical stability and environmental conditions promote such an elaborate architectural feature, which requires thoughtful planning and proper exploitation.

The arising problems with these facades are mainly related to the ventilation of the intermediate space between the glass layers by means of natural forces. The mechanisms of natural ventilation are more than clear, but still quite hard to be efficiently harnessed. The lack of driving forces during specific periods of time causes the poor performance of the facade, thus provoking dissatisfaction of the user and owner of the building. A consequence from the poor ventilation is the issue of overheating due to solar radiation during warm seasons.

The focus of this project is to conduct experiments and analyze data for specific boundary conditions of a scaled DSF setup. The experimental setup, limitations and completed experiments are summarized and presented in the most convenient way. The properties of interest are air velocity and temperature inside the cavity.

In the first part is reviewed the physics of flows based on the book Incropera et al. [2011]. As an introduction to the matter and the terms used later are considered as most relevant the convection principles and the boundary layer development on a flat plate. The different dimensionless criteria used for the analysis of the flow are briefly explained and presented, together with the used ratios of dimensionless numbers and concepts. The available literature on the topic of flow in vertical channels is also summarized in this part. It includes a literature review of similar articles and a summary of the most relevant for the current project. In this chapter is explained as well briefly about the functions and applicability of the DSF structures in buildings. Advantages and disadvantages are enumerated for the better understanding of the DSF constructions in building design.

Further in the second part is presented the problem formulation for the report including the goals and objectives of the work. After it are explained the experimental setup and the assumptions following it. The used equipment is specified and the work principles explained. A description of all data treatment techniques and analysis is summarized for convenience. In this part are presented also all experimental results and analysis. The experiments are sorted in groups, based on their varied parameter.

The third part includes a discussion of the obtained results and analysis taking into account the limitations of the experimental work. Proposals for future work are also summarized with regards to both improvement of experimental set-up, measurement and analysis procedure. At the end of the chapter a conclusion of the project is presented.

In Appendix are included all of the results cited inside the report, but not included in the main body, as well as the content of the electronic appendix attached to the report.

Part I

Theory and literature review

This part contains an introduction to the scientific background of the problem. It includes explanation of the physical processes and the dimensionless numbers relevant for the flow description. Additionally are presented explanations of the Double Skin Facade principle and advantages and disadvantages of the concept. The literature review consists of articles relevant to the topic of flow nature in vertical channels.

Physical processes and dimensionless numbers 2

The following chapter is based on the book - *Fundamentals of Heat and Mass Transfer 7th edition* by Incropera, Bergman, DeWitt and Lavine. Incropera et al. [2011]

2.1 Free and forced convection principle

2.1.1 Free convection principle

Free or natural convection is a type of heat transfer process between a body force and surrounding fluid in which density gradients are present. The phenomenon is called buoyancy and the corresponding force - buoyancy force. Normally, the considered body force is gravity, however it could be centrifugal force from a rotating machine or a Coriolis force due to atmospheric and oceanic rotational motions. The buoyancy force is driven by a density gradient, which most commonly is due to existence of temperature or composition differences.

For the forward explanation the focus is on the density dependence on temperature and as a body force is used gravity. However, the presence of fluid density difference in a gravitational field does not ensure the existence of free convection flow. If we take a case, where the fluid is enclosed by two large, horizontal plates with different temperature ($T_1 \neq T_2$), the existence of free convection flow will depend only on the position of the heated plates. The example is visualized on figure 2.1 .

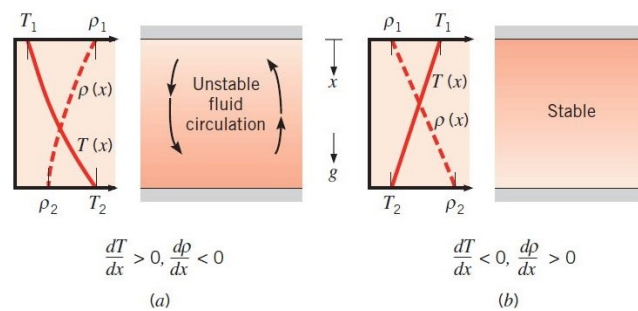


Figure 2.1. Conditions in a fluid between plates at different temperatures: (a) Unstable temperature gradient, (b) Stable temperature gradient. Incropera et al. [2011]

Case (a) represents a temperature gradient, where the lower plate has a higher temperature than the upper one. On the contrary, the density decreases from the upper to the lower plate. If the temperature difference exceeds a critical value, the buoyancy forces will overcome the viscous forces and the fluid will start to circulate due to the density gradient. The process will stop when the temperature difference decreases under the critical one. However, if we change the position of the plates, like in case (b), there would be no free convection flow, but a heat transfer due to conduction.

An example for free convection flow is the plume flow. This is flow, which rises above heated objects like people or heat sources. It entrains surrounding air and as a result the plume dimensions increase. However, it will eventually dissipate horizontally due to viscous effects and decreased buoyancy force, caused by cooling of the fluid in the plume. On figure 2.2 is present the thermal plume.

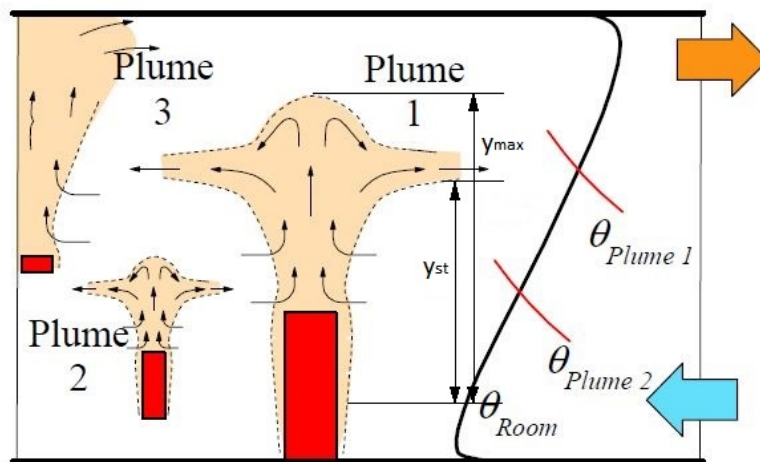


Figure 2.2. Thermal plume above a heat source, Skistad et al. [2004]

On figure 2.2 is visible another type of free convection flow - Plume 3, where the flow is attached to a surface. In this case near the surface is formed the so called boundary layer, which has different flow pattern than the one in the non disturbed region of the flow. Based on the fluid and surface properties the boundary layer can have a significant effect on the flow. More precise explanation of a boundary layer can be found in section 2.2 on the facing page .

Free convection flow is characterized as a low speed process. This means that in comparison with forced convection the heat transfer and the velocities are slower. With the rising expectation for low energy consumption in buildings, the free convection flow is not only preferred due to decreased risk of draughts, but also due to low energy necessities.

2.1.2 Forced convection principle

Forced convection is called the process in which the driving force of the flow is induced by a fan or other mechanical device, which can guide the fluid in a given direction. On figure 2.3 is shown the principle of forced convection flow, which typically is described with an increased heat transfer between the fluid and the body:

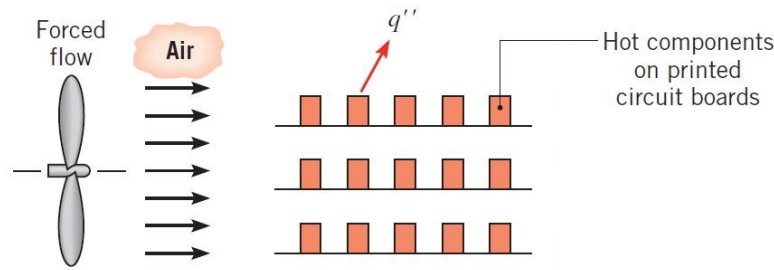


Figure 2.3. Forced convection heat transfer from a hot body, Incropera et al. [2011]

The speed of the forced convection flow is strictly dependent on the position of the fan and the forces which assist or oppose the flow. Buoyancy or gravity forces are just a few which can affect the flow to reach a given target. This combination of forced and natural convection is classified as a mixed convection flow. To verify which driving forces are dominant Gr/Re^2 ratio should be calculated, which gives the relation. This is further explained in section 2.3 on page 11 .

2.2 Convection boundary layers

2.2.1 Velocity boundary layer

The easiest way to explain the velocity boundary layer is to consider a flow over a flat plate, like in figure 2.4 . The fluid particles, which contact the surface, decrease significantly their velocity, in most cases it is valid to assume zero velocity at the surface. These particles then affect the velocity of the neighboring particles in the adjoining fluid layer by retarding them. This retardation starts spreading layer after layer until at distance $y = \delta$ from the surface the effect becomes negligible. This is caused by shear stresses τ , which act in planes parallel to the fluid velocity. From the surface in y-direction the velocity component u starts increasing until it reaches the velocity of the free stream outside the velocity boundary layer - u_∞ .

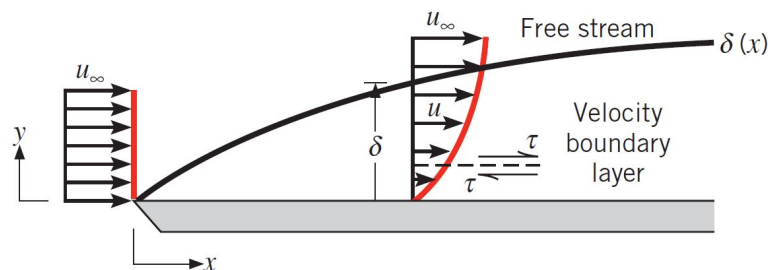


Figure 2.4. Velocity boundary layer developed on a flat plate, Incropera et al. [2011]

The velocity boundary layer thickness is expressed by δ , which is defined as the value of

y for which $u = 0.99u_\infty$. The flow is divided on two distinct regions: velocity boundary layer, in which the shear stresses and the velocity gradients are large, and free stream, where the shear stresses and the velocity gradient are negligible. The velocity boundary layer thickness δ increases with the distance from the leading edge (x-direction) due to further penetration of the viscosity into the free stream.

The flow in the boundary layer over a flat plate has three stages of development as shown on figure 2.5 - laminar, transition and turbulent flow.

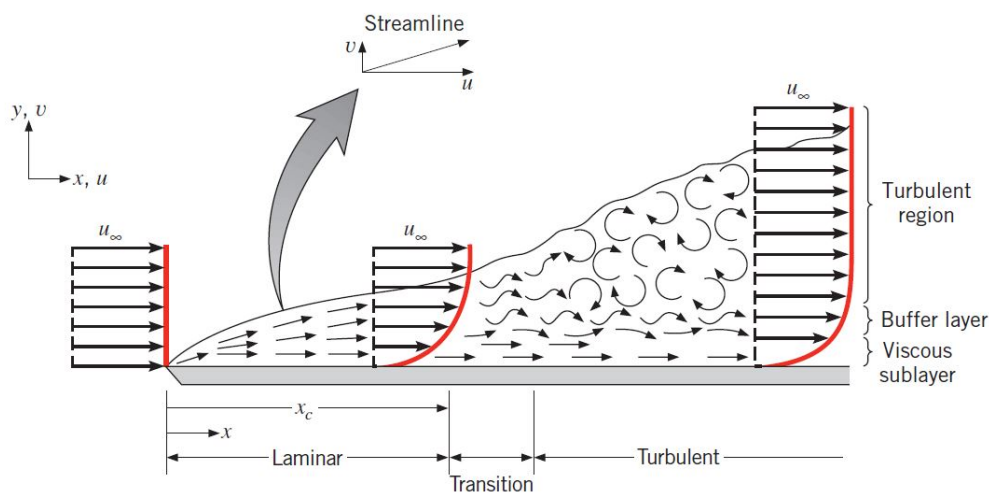


Figure 2.5. Velocity boundary layer development on a flat plate, Incropera et al. [2011]

The laminar boundary layer is characterized with a highly ordered fluid flow in form of streamlines and proceeds to increase until it reaches the transition zone. In the transition zone the flow changes with time from laminar to turbulent.

The fully turbulent boundary layer is described by a chaotic movement of the fluid particles called mixing. It carries high-speed fluid toward the solid surface and slow-speed fluid farther into the free stream. Significant part of the mixing is due to stream wise vortices generated intermittently near the flat plate. In y-direction the turbulent boundary layer can be divided on three sub layers. The first is the viscous sublayer in which the velocity profile is nearly linear and the motion is diffusion driven. The second sublayer is buffer layer which is a transition layer between the viscous sublayer and the turbulent region. In the turbulent region the flow is driven by turbulent mixing. A comparison between laminar and turbulent velocity profile is shown on figure 2.6.

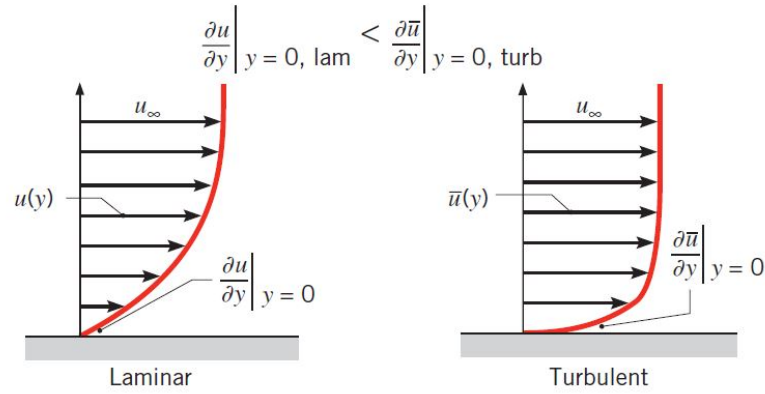


Figure 2.6. Comparison of laminar and turbulent velocity boundary layer profiles for the same free stream velocity, Incropera et al. [2011]

The figure shows that the turbulent boundary layer curve is relatively flat in comparison with laminar. This is due to mixing within the buffer layer and the turbulent region. As a result this affects the viscous sublayer by increasing the velocity gradients within.

2.2.2 Thermal boundary layer

A thermal boundary layer develops when there is a temperature difference between free stream fluid flow and adjacent surface. Lets consider a flow over an isothermal flat plate as shown on figure 2.7. At the leading edge an uniform temperature distribution profile is supplied, where $T(y) = T_\infty$.

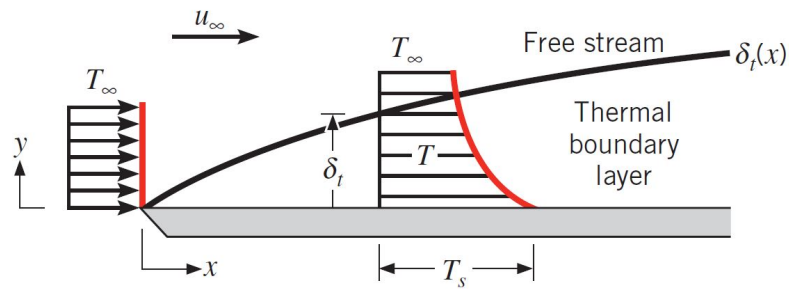


Figure 2.7. Thermal boundary layer development on an isothermal flat plate, Incropera et al. [2011]

Similar to the velocity boundary layer, the particles which contact the isothermal surface achieve thermal equilibrium with it. These particles exchange energy with the adjacent fluid layers and develop a temperature gradient. The region in which a temperature gradient exists is called thermal boundary layer. Its thickness δ_t is defined as the value of y for which:

$$\frac{T_s - T}{T_s - T_\infty} = 0.99 \quad (2.1)$$

where:

T_s	Surface temperature, [K]
T	Temperature within the thermal boundary layer, [K]
T_∞	Temperature outside the thermal boundary layer, [K]

With increasing distance from the leading edge (x) the effect of heat transfer penetrate further into the free stream, which increases the thermal boundary layer.

The local surface heat flux is expressed from Fourier's law to the fluid at $y = 0$, where the surface velocity is zero and the energy transfer occurs only by conduction:

$$q_s'' = -k_f \frac{\partial T}{\partial y} \Big|_{y=0} \quad (2.2)$$

Additionally, the surface heat flux can be obtained from Newtown's law of cooling, where:

$$q_s'' = h(T_s - T_\infty) \quad (2.3)$$

Combining the two previous equations the convective heat transfer coefficient gets the following form:

$$h = \frac{-k_f \partial T / \partial y \Big|_{y=0}}{T_s - T_\infty} \quad (2.4)$$

where:

q_s''	local surface heat flux, [W/m ²]
k_f	thermal conductivity of the fluid, [W/(m.K)]
T	fluid temperature, [K]
h	convection heat transfer coefficient, [W/(m ² .K)]
T_s	surface temperature, [K]
T_∞	temperature outside the thermal boundary layer, [K]

As a result can be stated that the magnitude of $\partial T / \partial y \Big|_{y=0}$ decreases with increase of x, which leads to decrease of q_s'' and h .

2.2.3 Boundary layer influence on a flow

Considering the flow three regimes can be delimited: laminar, transient and turbulent flow, which mainly depend on the velocity. In most cases the flow is restricted by a surface, which leads to a development of a boundary layer. Lets consider a laminar flow in a pipe of radius r_o with an uniform velocity on the entrance. When the fluid contacts the surface, due to the viscous forces a boundary layer will develop towards the length of the pipe (x). This development cause the inviscid flow to shrink until it finally disappears and the boundary layers merge. The region of inviscid flow shrinkage is called entrance region. The zone after the merge of boundary layer is classified as a fully developed region, where

the viscous effects extend over the entire cross section. A visualization is presented on figure 2.8.

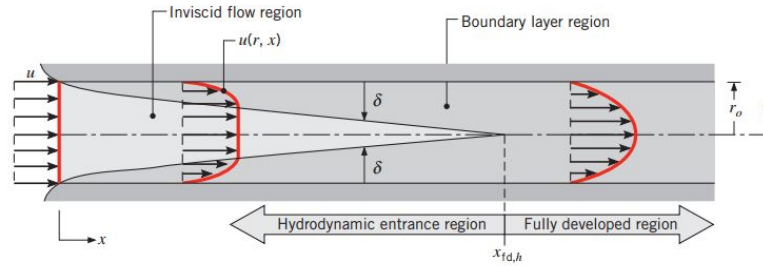


Figure 2.8. Laminar boundary layer development in a pipe, Incropera et al. [2011]

The fully developed flow can be both laminar or turbulent, which depending on the type of the flow will cause the velocity profile to change shape from sharper to flatter. To characterize the flow regime in case of forced convection is normally used Reynolds number, on the other hand in case of free convection it is preferred to work with Rayleigh number. More information about the dimensionless number can be found in section 2.3.

2.3 Dimensionless numbers

This section is necessary for the current paper to make the results as widely applicable as possible. The concept of similitude plays an important role for cases, where only analysis can not solve the problem, but a combination between analysis and experimental data. As a result an experiments made on one system can be used to describe the behavior of another similar one, however a relationship between the systems is necessary.

This paper is focused on fluid flow characterization and the following dimensionless numbers are normally used for achieving that target:

- Reynolds number

Reynolds number is important for all types of fluid dynamics problems. It expresses the relation between inertial forces and viscous forces. Reynolds number is preferred dimensionless number for force convection problems.

$$Re = \frac{\rho V l}{\mu} = \frac{V l}{\nu} = \frac{\text{inertial forces}}{\text{viscous forces}} \quad (2.5)$$

where:

ρ	fluid density, $[kg/m^3]$
V	fluid velocity, $[m/s]$
μ	dynamic viscosity, $[N.s/m^2]$
l	characteristic dimension, $[m]$
ν	kinematic viscosity, $[m^2/s]$

- Grashof number

Grashof number is used to characterize problems in fluid dynamics and heat transfer. It express the ratio of buoyancy forces to viscous ones. In case of free convection problem Grashof number is widely used.

$$Gr = \frac{g\beta(T_s - T_\infty)l^3}{\nu^2} = \frac{\text{buoyancy forces}}{\text{viscous forces}} \quad (2.6)$$

where:

g	gravity acceleration, [m^2/s]
β	coefficient of thermal expansion, [$1/K$]
T_s	surface temperature, [K]
T_∞	bulk temperature, [K]
l	characteristic dimension, [m]
ν	kinematic viscosity, [m^2/s]

- Prandtl number

Prandtl number is defined as the ratio of momentum diffusivity to thermal diffusivity. It is dependent only on the fluid properties and fluid state and contains no characteristic dimension. Therefore, it is often given in property tables.

$$Pr = \frac{\nu}{\alpha} = \frac{C_p\mu}{k} = \frac{\text{viscous diffusion rate}}{\text{thermal diffusion rate}} \quad (2.7)$$

where:

ν	kinematic viscosity, [m^2/s]
α	convective heat transfer coefficient, [$W/(m^2.K)$]
μ	dynamic viscosity, [$N.s/m^2$]
k	thermal conductivity, [$W/(m.K)$]
C_p	specific heat capacity, [$J/(kg.K)$]

- Rayleigh number

Rayleigh number characterizes free convection flows. It is described as the ratio of buoyancy against viscous forces multiplied by the ratio of momentum diffusivity and thermal diffusivity. Either laminar or turbulent flow regime can be estimated based on the relative magnitude of the Rayleigh number. It is the product of multiplication of Grashof number with Prandtl number.

$$Ra = Gr.Pr = \frac{g\beta(T_s - T_\infty)l^3}{\nu\alpha} = \frac{\text{buoyancy forces}}{\text{viscous forces}} \cdot \frac{\text{viscous diffusion rate}}{\text{thermal diffusion rate}} \quad (2.8)$$

- Dimensionless number $\frac{Gr}{Re^2}$

This dimensionless number is used to characterize the convection regime in the flow. Grashof number is used to describe the buoyancy forces in the flow in case of free convection, while Reynolds number does the same for forced convection flow. In this way the relation between those two dimensionless numbers will give the possibility to mathematically distinguish the flow regimes:

$$\frac{Gr}{Re^2} \ll 1 \Rightarrow \text{forced convection} \quad (2.9)$$

$$\frac{Gr}{Re^2} \gg 1 \Rightarrow \text{free convection} \quad (2.10)$$

$$\frac{Gr}{Re^2} \approx 1 \Rightarrow \text{mixed convection} \quad (2.11)$$

To be precise, a free convection flow is the one in which there are no forced convection velocities, which leads to expression: $Gr/Re^2 = \infty$. However values above one are also accepted as a free convection flow.

Purpose and applicability of DSF 3

3.1 Double skin emergence in buildings design

Double skin facade appears in central Europe, where the box-type double windows were a viable way to increase the envelope thermal insulation. Early examples can be seen in farmhouses, where the box-windows were used in combination with external shutters creating buffer space, which served as a mean of increasing the thermal comfort. Based on the records and articles from 19-th century, can be judged that the idea of expanding this type of windows was arising in the progressive minds. Saelens [2002] described a version of mechanically ventilated multiple skin facade, where the main focus was to be overheated the cold winter air before entering the premises.

Another example is cited by Crespo [1999], where the main idea behind the double skin facade was to utilize daylight in the Steiff Factory in Giengen, Germany, while protecting from the high heat gains through the glass. These examples all date back to the beginning of the 20-th century. Other structures in the early 20-th century were designed in Russia, France, Austria and in all of the cases the reasoning behind them is the same, to adapt to the surrounding environment, by regulating heat, cold, light and wind.

Later in the 70's and early 80's the DSF started gaining popularity again, this time not with daylight and insulation improvement in mind. This time the argumentation was based on environmental or aesthetic concerns. Later with the development of urban infrastructure, another application of the DSF arose. The sound insulating properties of it began to intrigue architects and engineers. [Poirazis, 2004]

From the very beginning until the present times the functions and desires for DSF have increased, but follow the same basic principles. With the development of technology an improvement of materials higher goals are set-up in front of the DSF structures.

3.2 DSF classification

Double skin facade concept has a lot to offer to users. The main advantages are distinguished among other facade solutions with their multi-purpose use. The DSF was originally developed as an increasing daylight feature of buildings. Later with the development designers realized that the sound protection and natural ventilation in the

facade cavity are an asset to the construction. At the moment these three features are the most favorable properties of the facade.

According to literature the various authors have created own categorization of the types of double skin facades. The categorization is based on construction, origin, type of flow in the cavity etc. Here the categories according to Oesterle [2001] are presented.

- Box window type: This construction is specific with the horizontal and vertical partitioning dividing the facade into small and independent boxes
- Shaft box type: Prefabricated window elements are placed in the facade and connected with vertical shafts, forming a high channel for providing the stack effect.
- Corridor facade: In this type of facade the separation is done horizontally only, providing the option, depending on the gap's thickness, to be utilized the space for a walk path. Still partitioning is necessary for fire safety, acoustical and ventilation reasons.
- Multi storey DSF: No partitioning in the facade's cavity, the ventilation air circulates from the bottom to the top of the building.

If we consider a simple cut of the facade for example one floor, in terms of natural ventilation, usually a pair of openings are designed in the bottom and the top of the facade, on both internal and external surfaces. This determines the facade type as an *Active facade*. Looking deeper in the aspect can be distinguished several regimes of the flow. They are depending on the facade openings scheme.

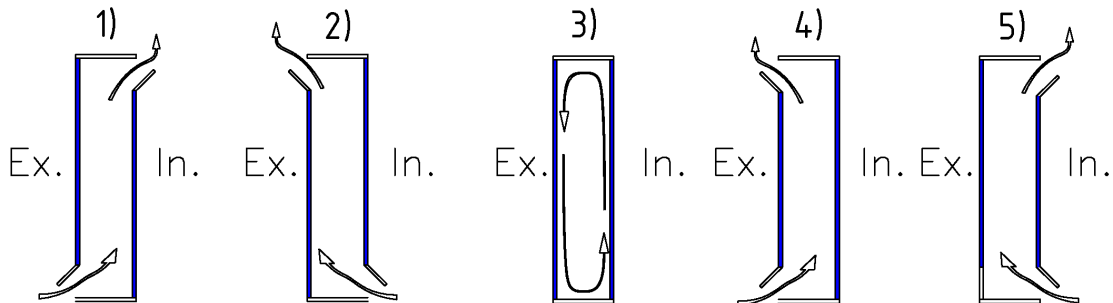


Figure 3.1. Double skin facade basic operating principles Larsen [2008]

In the following points are explained the above enumerated schemes.

1. Used to overheat the external air before supplying into the room or in most cases into the HVAC system. This scheme is the most frequently used during heating period. The idea is that buoyancy is enhanced in the gap, due to the heat transfer from the inner glass and the sun radiation through the external glass. This in combination with the wind pressure helps the natural ventilation effect.
2. Here the exhaust indoor air is driven through the DSF. In case of solar radiation it enhances the naturally driven flow, even during the heating period.

3. This scheme utilizes the gap air as an insulation layer. Still in the cavity a flow due to convection is creating recirculation, the direction of which depends on temperature conditions on both sides of the DSF.
4. This case is named - External air curtain, where the air cavity is ventilated with external air. It is useful during the cooling season, when because of the sun radiation strong buoyant forces are generated between the glass surfaces. Together with the wind induced pressure they force the cooling of the gap. Ventilation is necessary, because overheating will lead to discomfort on the inner side of the facade.
5. Internal air curtain - the same as above counts for the stack effect but in this case the mode is used during the heating season. In that way the internal glass pane is kept at higher temperature than usual, providing comfort feeling.

3.3 Advantages and disadvantages of Double Skin Facades

Double skin facades are a very controversial topic with regards to the usage and applicability. A lot of architects and engineers think that with the higher level of complexity comes the bigger risk of failure and misuse. Others count on the better materials to ensure the proper performance. However a short list of disadvantages and advantages of the DSF systems can be summarized from the literature sources, in the following pages.

3.3.1 Disadvantages of DSF constructions

- **Construction costs**
- **Reduction of useful building space**
- **Maintenance and operational costs**
- **Overheating problems**

A famous businessman, philanthropist and writer once said:

"To every disadvantage there is a corresponding advantage."

W. Clement Stone

3.3.2 Advantages of Double Skin Facades

- **Acoustic insulation**
- **Natural and Night time ventilation**
- **Energy savings**
 - Lighting energy
 - Heating/Cooling energy
 - Ventilation energy
- **Protection of shading devices**
- **Architectural properties - Transparency of building appearance**

Flow between parallel vertical plates 4

Various authors have worked on the topic of flow in vertical channels, which describes the flow in the DSF. As clarified before, there appear different boundary layers and flow regimes. The majority of articles describe laminar natural convection flow in the cavity between the asymmetrically heated plates, however the turbulent natural convection is considered of bigger importance in that case. An attempt to summarize the most relevant papers is made in the next paragraphs.

The work of Fedorov and Viskanta [1997], over a buoyancy driven turbulent flow in a vertical non-convergent channel, is considered one of the fundamental works in the field. According to the author the numerical model was sufficient to predict with certain precision the happening in the channel. The model depicted an asymmetrically heated channel, with open horizontal sides. The channel was maintained with isoflux condition at the heated surface, and adiabatic at the opposite one. The purpose of the work was to be established the heat transfer characteristics inside the channel. The numerical model was compared with experimental data from Miyamoto et al. [1986].

The experimental setup in Miyamoto et al. [1986] consisted of a channel with height of 4980 *mm* and 950 *mm* in length. The experimental widths were 50, 100, and 200 *mm*. Heat transfer coefficients were determined for the uniformly distributed heat flux. An observation made by Fedorov and Viskanta [1997] is that depending on turbulence intensity at the channel's inlet the transition from laminar to turbulent flow and the heat transfer coefficient vary. Location of the transition point from laminar to turbulent flow was not determined with certainty. The research of Fedorov and Viskanta [1997] was done for the field of electronics and power equipment cooling.

For the same type of channel flow as above in the work of Yilmaz and Fraser [2007] are studied the temperature and velocity profiles inside the gap and turbulent kinetic energy by comparing both experimental data from LDA measurement and CFD model. The experimental setup is depicted in another article from Yilmaz and Gilchrist [2007]. The article reveals similar experimental setup as Miyamoto et al. [1986], though with different dimensions. LDA system is used for non-intrusive measurements of velocities in the channel. The channel itself was built in a separate enclosure for avoiding external draughts. The used set-up consists of glass wall, electric heaters polished aluminum plate for the back wall and insulated sidewalls. The width of the channel was set to 0.1 m and

the experimental temperatures for the heated wall varied from 60 to 130 ° C.

From the analysis the author concludes that based on the kinetic energy profiles derived from the CFD model the flow close to the outlet is fully turbulent. The model developed by Yilmaz and Fraser [2007] as well confirms the empirical results within the limits of the experimental uncertainty.

Another crucial topic in the present study is the flow reversal in the gap, referred also as recirculation. None of the previous authors observed this phenomenon in the experimental or numerical studies. The flow reversal (recirculation) is illustrated on the following scheme.

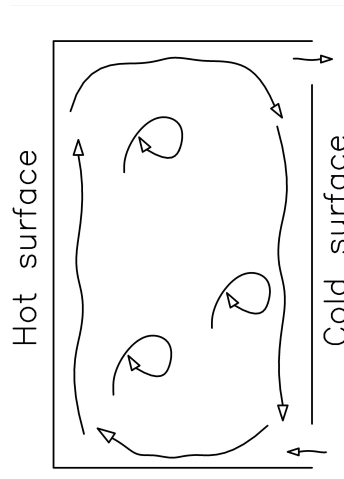


Figure 4.1. Schematic diagram of flow reversal (recirculation) and vortexes (eddies)

The recirculation consists of upward direction flow along the hot surface of the channel, and opposite direction flow along the cold surface. Recirculation concerns the flow reversal in global scale, while the local changes in flow direction (fig:4.1) are named vortexes or eddies.

The recirculation phenomenon is observed by Desrayaud and Lauriat [2009] whose article on the topic was only based on a numerical study of flow reversal in symmetrically heated vertical plate channel. Extensive dimensional analysis is done over the custom made CFD model. Different Gr and Re numbers are simulated and according to the authors there can be observed recirculation in the entrance region of the gap. The reversed flow arises from the sharp increase of the air temperature when entering the channel. However according to the model the flow reversal disappears before reaching the end of the channel. The parametric study done over the model in Desrayaud and Lauriat [2009] gave the idea that flow reversal is independent of the Peclet number for $Pe > 200$, but occurs for $Gr/Re \geq 300$.

In a small scale experiment of turbulent natural convection in asymmetrically heated channel, Ayinde et al. [2007] presented vector fields from a PIV (Photo Image Velocimetry) measurements where could be seen a flow reversal at the top and bottom of the channel. The authors worked over a small scale experimental setup with one surface heated above and one cooled bellow ambient temperature. Figure 4.2 and 4.3 show the top and bottom

of the experimental cavity.

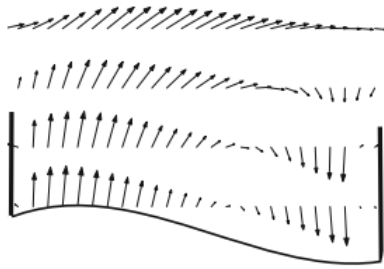


Figure 4.2. Top of cavity

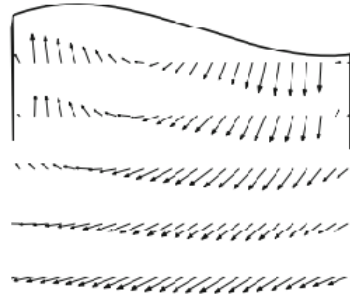


Figure 4.3. Bottom of cavity

Photo Image Velocimetry of gap between asymmetrically heated plates Ayinde et al. [2007]

As can be seen from the figure the flow is moving upwards along the hot surface then shifts downwards along the cold creating circulating movement between the plates. At half the height of the gap are observed simultaneous upward and downward-flows close to the respective surfaces, and nearly stagnant zone in the core.

A Numerical analysis was done by Badr et al. [2006] based on turbulent flow in non-convergent channel with asymmetrical heating with different Rayleigh numbers and aspect ratios. The simulations included aspect ratios from 12.5 to 100 and two cases of isothermal and isoflux heating conditions. The numerical models are compared with experimental studies of Miyamoto et al. [1986] and Habib et al. [2002]. A recirculating flow was observed for the case with one heated and one cooled surface. According to the author the developed CFD model shows good agreement with the empirical results.

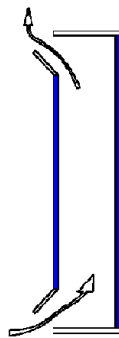


Figure 4.4. Most common DSF structure

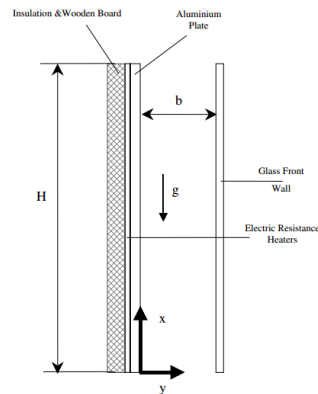


Figure 4.5. Experimental scheme Yilmaz and Fraser [2007]

Difference between reviewed articles and common DSF structures

The articles above refer to a flow between parallel plates, meaning the inlet flow has a vertical direction (Fig. 4.5), where for the most of the DSF structures the inlet and outlet are situated on the vertical sides of the channel, meaning - the flow direction at the inlet and outlet is horizontal (Fig.4.4). This is done for the utilization of wind pressure as much as possible. Due to this difference in the inlet and exhaust openings occurs an entrance flow region, which influence cannot be established by the before-mentioned experiments and simulations.

In another study by Zollner et al. [2002] the focus is over a functioning segment of a DSF structure, in an externally based experimental facility. The report is done with the purpose of determining heat transfer coefficients taking into account the solar radiation through the external layer and turbulent mixed convection inside the gap. A variation of different aspect ratios is conducted together with measurements of the flow rate. At the end a dimensional analysis is done for all of the results. Based on the experimental results the author states that the flow is strongly dependent of the aspect ratios H/S , H/h , S/h of the facade.

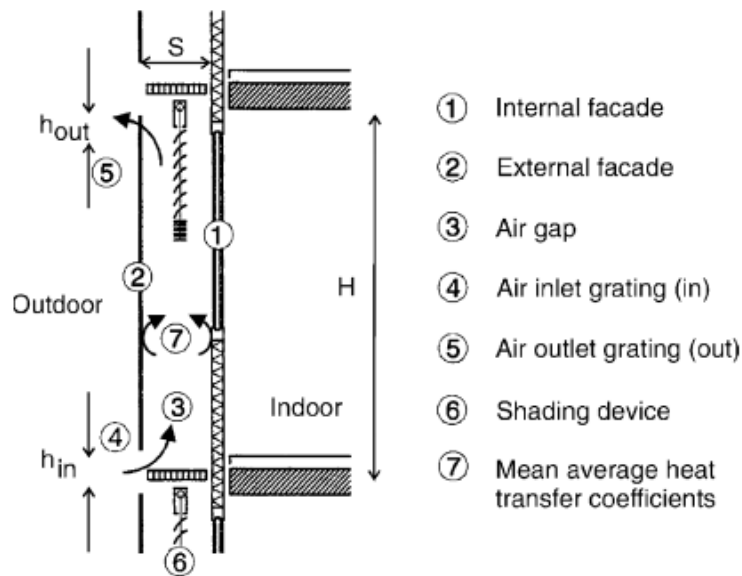


Figure 4.6. Schematic diagram of double-skin-facade, Zollner et al. [2002]

Another conclusion drawn from this research is that there is a highly circulating flow inside the gap. The flow is upwards directed near the internal facade, and downwards directed close to the external facade. Due to this recirculation the results for the temperature distribution showed highest temperatures not in the exhaust region, but in the middle height of the gap. The results obtained from the experimental setup in the work of Zollner et al. [2002] are analyzed by the author by dividing the gap thickness into four layers.

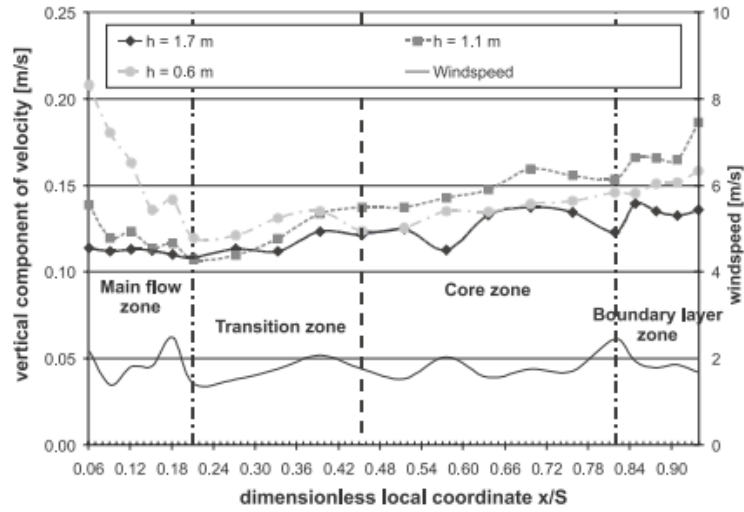


Figure 4.7. Velocity distribution for experimental DSF (0.33m thickness, 0.04m inlet height) (Zollner et al. [2002])

Investigation of flow between vertical plates was done by [Habib et al., 2002]. The article is examining the turbulent natural convection between two symmetrically and asymmetrically heated plates. The application is again in the field of electronics, and the experimental setup has rather small dimensions compared to a functional section of a facade element. However, the results obtained by the author for the asymmetrical case show the pattern of recirculation between the plates. Moreover, the Rayleigh number is investigated and compared to other authors. For the Rayleigh number is considered a value of $Ra \geq 10^5$ for beginning the development of turbulent flow. The temperature difference, between the hot and cold plates is 20°C .

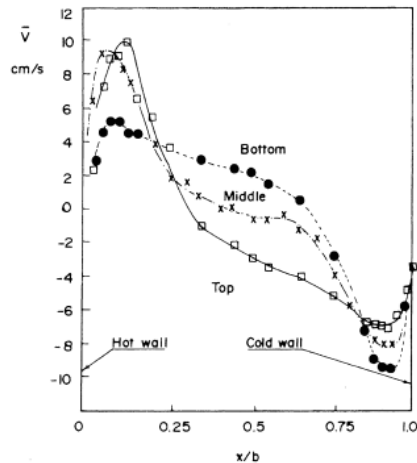


Figure 4.8. Mean vertical velocity for asymmetrical flow with $Ra=2 \cdot 10^6$ for different heights [Habib et al., 2002]

On figure 4.8 can be seen that the flow accelerates over the hot side and decelerates on

the cold. This implies that there are developing two opposing boundary layers.

An extensive work about Double-skin facade in external environment is done by [Larsen, 2008]. The experimental work aimed to investigate the flow characteristics within the gap of the facade in external curtain mode (figure 3.1). The convective flow regime inside the gap is regarded as undeveloped turbulent, and the channel is considered wide, according to its aspect ratio. On figure 4.10 can be seen the experimental room used in the research. Three air flow measurements principles were used in the work. Velocity profile method, tracer gas and pressure difference method. The experimental results showed that in major part of the time the flow in the cavity was wind dominant, and only for wind velocities under 4 m/s could be noticed a buoyancy dominant flow.

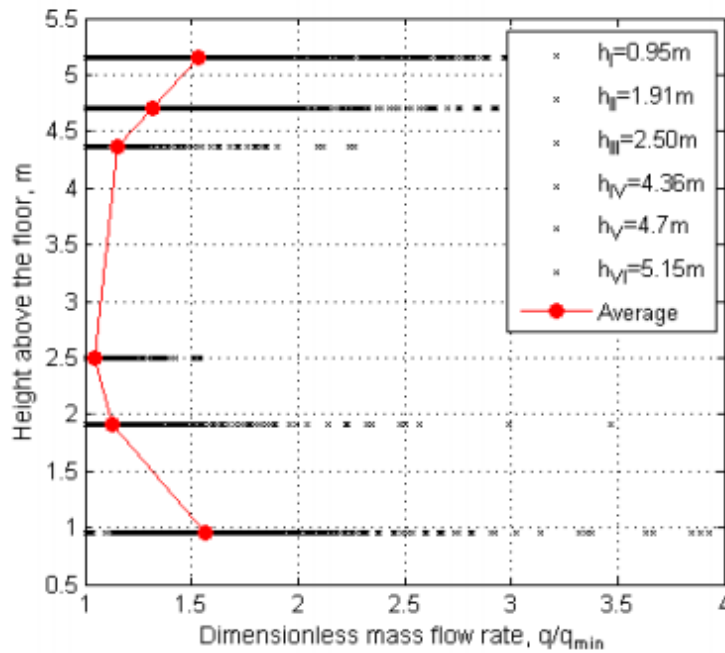


Figure 4.9. Velocity measurements at different heights Larsen, 2008

The velocity profile method on figure 4.9 showed that inside the cavity at lowest and highest levels the flow is bigger than at the middle. This is explained with the wind washout effect over the inlet and exhaust openings. The dimensionless mass flow rate is expressed as the measured value over the lowest one in the cavity.

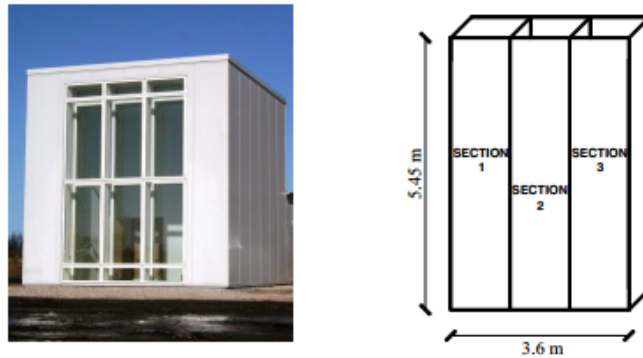


Figure 4.10. Experimental facility - "The Cube" Larsen, 2008

Furthermore based on the ratio Gr/Re^2 and the temperature in the cavity, the author established the flow regime for different operation modes (equation 2.9 to 2.11). The ratio Gr/Re^2 is an important parameter, because as stated in section 2.3 it gives information for the flow convection regime - if it is buoyancy driven or momentum driven. In the work of Larsen 2008 is developed as well a concept of flow recirculation inside the facade. The assumption made by the author is that the flow reversal is not a steady happening, but rather fluctuating flow variation with periodical cycle.

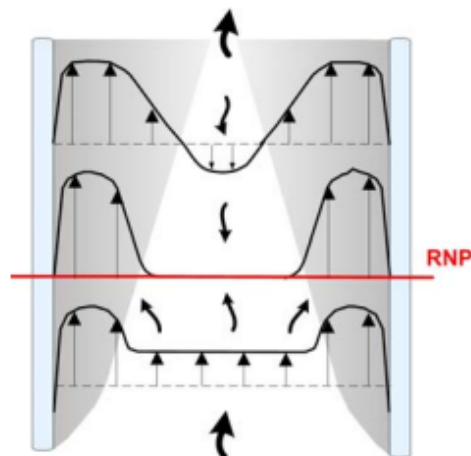


Figure 4.11. Flow reversal hypothesis Larsen, 2008

Figure 4.11 shows the basic idea of recirculation in the DSF. In this case the example given is considering a symmetrically heated wide channel. According to the hypothesis, a boundary layer starts developing in the entrance of the gap. With the penetration further due to the dominating velocities in the boundary layer, the velocity in the core will decrease in order to maintain the mass balance.

The next occurrence is equalizing the mass flows in the boundary layer and at the entrance of the cavity, which leads to the conclusion that a Recirculation Neutral Plane (RNP)

exists,(Based on continuity equation) where velocity and mass flow rate are equal to zero.

The last step is for the boundary layer mass flow rate to overcome the entrance flow rate, which leads to reversing the flow from above that section in order to maintain the continuity criteria. Here it is assumed that in the entrance of the cavity the flow is driven due to forced/mixed convection, while later with development of the boundary layer the movement is caused entirely by free convection.

Based on the literature review in the work of Larsen [2008], the author enumerated several conclusions for the flow recirculation appearance.

- Increasing Grashof number enhances flow recirculation.
- Flow recirculation is present at the end of the channel
- Recirculation occurs at the colder surface in asymmetrically heated channel

Based on the recirculation theory in the work of Larsen [2008] is proposed the assumption that for the region of recirculation can be judged by the vertical temperature gradient. On fig 4.12 are presented the cases:

- a - linear temperature profile in the cavity(No recirculation)
- b - recirculation profile, average temperature in the cavity is increasing, due to the increase of convective heat transfer. However, temperature gradient disappears in the zone of recirculation, due to the mixing.
- c - after the recirculation in b, the flow temperature drops the profile will accept the form in fig. 4.12 c and the mass flow will be reduced.

Taking into account the previous statements it is derived that the recirculating flow inside the cavity has an unsteady fluctuating manner. The vertical temperature profile will vary from b) to c) through a) during the recirculation period. (Larsen [2008])

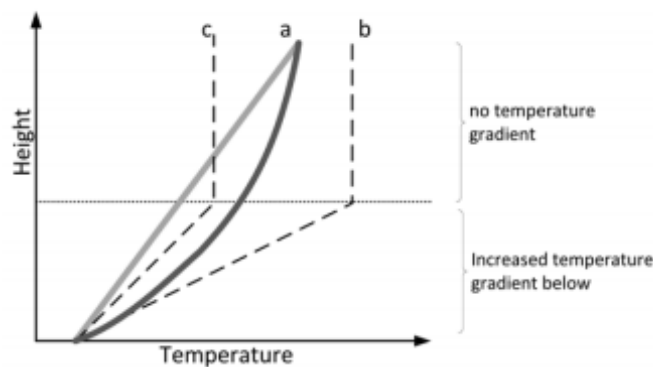


Figure 4.12. Vertical temperature gradient assumption (Larsen [2008])

The DSF is considered vulnerable to recirculating flow in periods with strong solar radiation or low wind pressure. The problem is marked by an insufficient driving force for the development of boundary layer (Larsen 2008).

In the work of Mikkelsen [2015] turbulent natural convection was examined between asymmetrically heated vertical plates. The experimental setup consisted of a facade

construction in laboratory conditions, where the heating was assured by electrical heaters. The flow was analyzed based on precise measurements of temperatures at discrete points inside the cavity. According to analyzes the most relevant parameters for the flow in the cavity were regarded - the Rayleigh number, Reynolds number and Gr/Re^2 ratio.

The case presented below is named Test 5 in the project and has the following boundary conditions:

	Test 5
Ra_H [-]	$7.11 \cdot 10^{12}$
Gr_H [-]	$9.55 \cdot 10^{12}$
Re_H [-]	$8.03 \cdot 10^5$
Gr_H/Re_H^2 - ratio [-]	14.81
$T_{heater,SP}$ [°C]	30.00
$T_{heater,meas.}$ [°C]	25.95
$T_{inlet,SP}$ [°C]	15.00
$T_{inlet,meas.}$ [°C]	15.76
ACH [h ⁻¹]	4.00
$T_{heater,meas.} - T_{inlet,meas.}$ [°C]	10.18
$T_{heater,meas.} - T_{glass,meas.}$ [°C]	1.11

Figure 4.13. Experiment 5 test conditions (Mikkelsen, 2015)

On figure 4.14 can be seen the results for the same test in terms of temperatures stability.

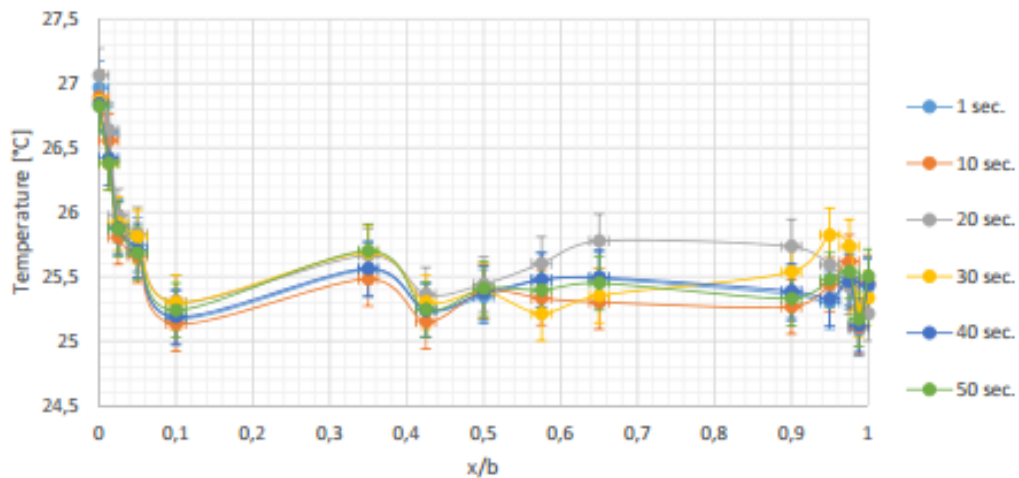


Figure 4.14. Stability in horizontal temperature profile at height 2.25m Mikkelsen, 2015

The stability analyze shows an average temperature for the chosen measurement intervals, thus presenting the instabilities inside the flow. Here the horizontal axis is presented as dimensionless distance from 0 to 1, where zero indicates the hot surface and one the cold. The cold surface has obviously highly fluctuating temperatures, which according to the author are caused by fluctuating pattern of the flow. The fluctuations are noticed at levels of 1.00m and 1.50m, in the entire horizontal plane, but above these heights are restricted to only the cold surface.

The terms regarding recirculation employed in the previous mentioned research by Mikkelsen [2015] were: "major recirculation" and "recirculation", respectively describing the flow reversal in global and local scales. Figure 4.15 left shows the "major recirculation", and to the right are shown both of the types.

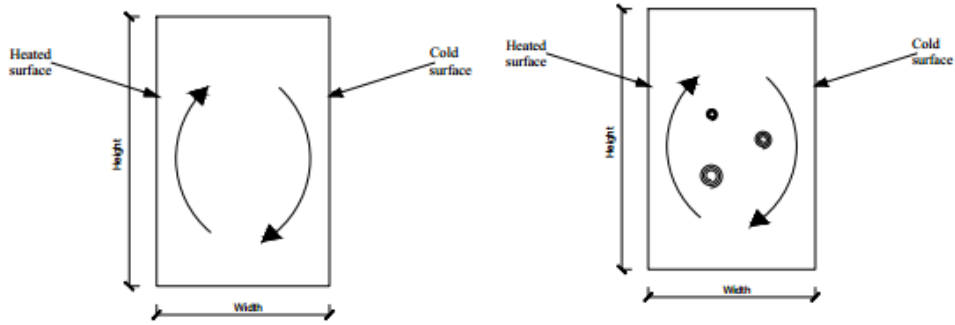


Figure 4.15. Recirculation types according to Mikkelsen, 2015

However, in this paper different terms will be employed. The fluid movement in global scale is named simply recirculation, and the local flow reversals - eddies/vortex formation (Fig.4.1).

Based on the literature review is made a comparison of the results in terms of Rayleigh number for some of the above mentioned authors. As explained in section 2.3 Rayleigh number is important as it represents transition from laminar to turbulent natural flow. Due to lack of information about specific parameters used in the calculation of Rayleigh number in some articles, assumptions are made. For comparing the results a modified Rayleigh criterion is used formed in the following way:

$$Ra^* = Gr.Pr = \frac{g\beta(T_s - T_\infty)b^3}{\nu\alpha} \frac{b}{H} \quad (4.1)$$

Where, the Gr number is calculated according to the depth of the gap (b). and the Ra number is multiplied by the inverse of the gap's aspect ratio(defined as height over depth(H/b))

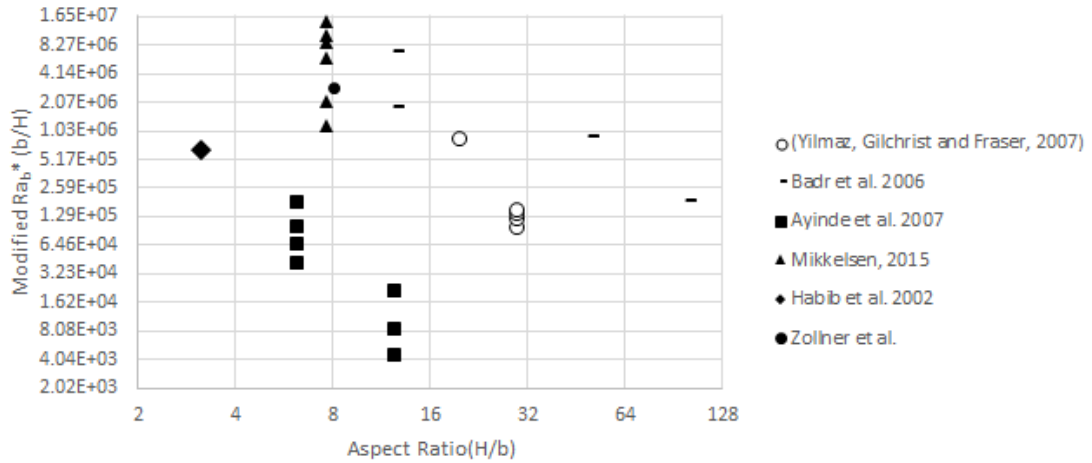


Figure 4.16. Comparison of modified Rayleigh numbers

Results with thick markers represent articles in which is mentioned or in a way observed the recirculation between the surfaces.

The results from Yilmaz and Gilchrist [2007] and Yilmaz and Fraser [2007] are bracketed in the legend, because of missing information and assumptions made about the calculation of the modified Rayleigh number. All presented authors claimed turbulent free convection flow regime between the vertical plates.

In the work of Habib et al. [2002] were assumed values of $Ra \geq 10^5$ for the transition from laminar to turbulent flow regime.

To sum up authors have considered channels with different aspect ratios and surface conditions. The researches in laboratory environment that used one heated surface and one adiabatic in most cases have not observed recirculation. The happening was reported in the cases where the surfaces were heated and cooled simultaneously. The heated surfaces were either maintained at uniform temperatures (isothermal), or with uniform flux (isoflux) conditions. Additionally the field tests conducted by Zollner et al. [2002], and Larsen [2008] give evidence of recirculating flow, but also induce uncertainty due to the unsteady boundary conditions. The CFD models according to all authors correspond to the compared experimental results.

As a further development of the work of Mikkelsen [2015], the current paper will be focused on measurement of velocities and temperatures in a similar experimental setup. The focus will be at vertical and horizontal velocity vectors between the asymmetrically heated plates. In the work of Mikkelsen [2015], was proven that the flow can be regarded as two dimensional, with sufficient precision. Therefore the velocities and temperatures at the cross section are assumed to show accurately enough the flow pattern in the cavity. The conclusion is based on infrared thermal images.

With regards to the above mentioned, in the present paper will be conducted tests, aiming to gain more knowledge about the flow recirculation in the gap between the vertical plates.

Part II

Experimental study

This part introduces the problem formulation, experimental geometry, used equipment and the conducted experiments and analyses. The analytical procedure is described in the beginning of the part and applied for all empirical results. The obtained data is divided into groups based on the varied experimental parameter. The results include temperature and velocity plots and dimensionless criteria evaluation. At the end a summary of the results and general statement for the flow pattern inside the cavity are included.

Problem formulation 5

The focus of this project is to clarify the turbulent free convection flow nature inside vertical parallel asymmetrically heated channel. The observed quantities are temperatures and velocities in the gap, while maintaining stable boundary conditions. This type of channel flow can be representative for various fields of research, for example cooling of electronics, solar chimneys, trombe walls or solar collectors. However, the application of interest in the project is for Double Skin Facades.

After introducing the concepts and terminologies linked with DSF structures and flows, can be seen that the problem lies in the air movement inside the gap. Depending on location and weather conditions, in an actual facade element both wind or solar radiation can be the dominating driving force. This creates a variable flow conditions and induces uncertainty in the predictions of the natural ventilation process.

During periods of strong winds the natural ventilation processes are predictable, however during periods of strong solar radiation, and low wind speeds, the buoyancy forces become dominant in the cavity disrupting the standard channel flow and causing uncertainty in the fluid motion. This uncertainty is a consequence of the variation of the convection coefficients and according to the employed theories it consist of strong development of boundary layers along the surfaces, eddies formations and recirculation flows inside the gap.

To simulate similar conditions to the reality is constructed a vertical channel, which is precisely described in section 6.1 on page 33. It is necessary to explain that there is initially supplied flow to the cavity, which is low-speed and fan driven. The reason for this supply flow is the essence of non-intrusive measurements (LDA), which requires a seeding particle supply in order to measure the velocity inside the cavity. In order to be precise in the classification of the flow are used dimensionless numbers like Grashof, Reynolds and Rayleigh. Depending on these criteria is classified the convection type. The authors' wish is to simulate free convection dominant flow. The values presented bellow, according to Incropera et al. [2011] bound the free convection flow characteristics.

$$\begin{array}{l|l} \text{Grashof/Reynolds}^2 & Gr_H/Re^2 \gg 1 \\ \text{Aspect ratio} & H/b > 2 \\ \text{Critical Rayleigh number} & Ra_H \approx 10^9 \end{array}$$

The Gr/Re^2 ratio should be much higher than one, for the natural convection to dominate over the forced. Values equal to one are regarded as mixed convection flow regime.

With Rayleigh numbers lower than 10^9 the flow is determined as laminar. When Rayleigh number reaches values higher than 10^9 heat transfer is increased, implying that the flow regime becomes turbulent. These relations are suitable for the shown aspect ratio. The ratio for vertical channel represents the cavity height/depth, thus determining it as either narrow or wide.

For short channels or large cavities with aspect ratio bigger than 2 occurs independent boundary layer development at each surface. The conditions in this cases correspond to those for isolated plate in an infinite, quiescent medium. On figure 5.1 is presented a free convection boundary layer development on a vertical plate. Incropera et al. [2011]

The explained model is employed in the current project analysis. The cavity surfaces are viewed as two separate vertical plates, with independently developing boundary layers.

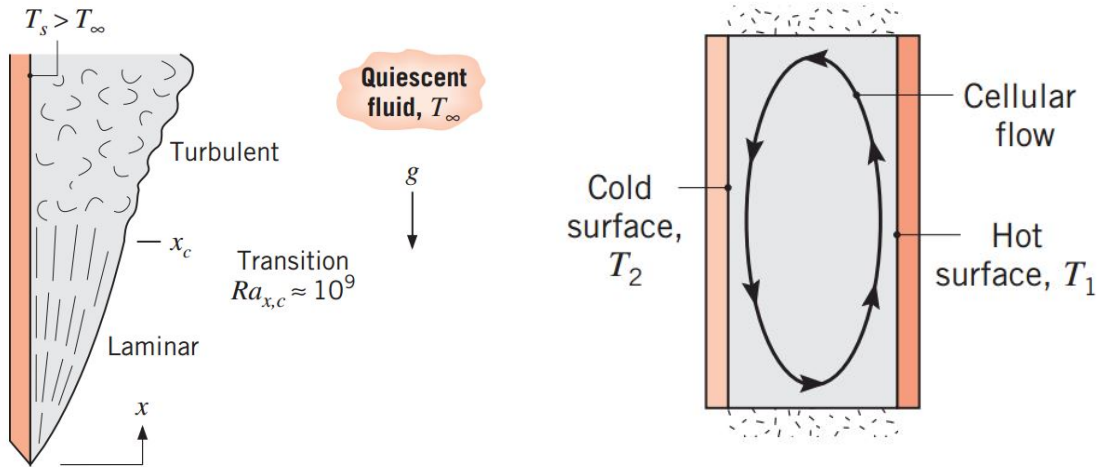


Figure 5.1. Free convection boundary layer transition on a vertical plate, Incropera et al. [2011]

Figure 5.2. Cellular flow in a vertical cavity with different sidewall temperatures, Incropera et al. [2011]

Additionally, the channel is asymmetrically heated. According to Incropera et al. [2011] the fluid motion is characterized by a recirculation or cellular flow, for which the fluid ascends along the hot surface and descends along the cold one, thus forming two opposing boundary layers. This is confirmed by Ayinde et al. [2007] and Habib et al. [2002] in section 4 on page 19 . The core becomes nearly stagnant, although additional cells can develop on the edge of the boundary layer, which causes it to become turbulent. A visualization of the flow pattern is presented on figure 5.2. Incropera et al. [2011]

The target of this report is to help clarify the conditions at which a recirculation flow occurs. The results are expected to contribute to the understanding of buoyancy dominated flow inside vertical asymmetrically heated non-convergent channel and can serve as a validation of a numerical model for predicting the DSF performance.

Experimental set up 6

6.1 Geometry

For the simulation of a DSF structure as accurate as possible, it is necessary to build a full scale setup which boundary conditions could be controlled precisely. In this case the box on figure 6.1 is situated in laboratory environment, ensuring the possibility to be applied steady boundary conditions. The box itself is referred further as "Hot box", the measurement volume - "cavity" and the measurement devices as "equipment".

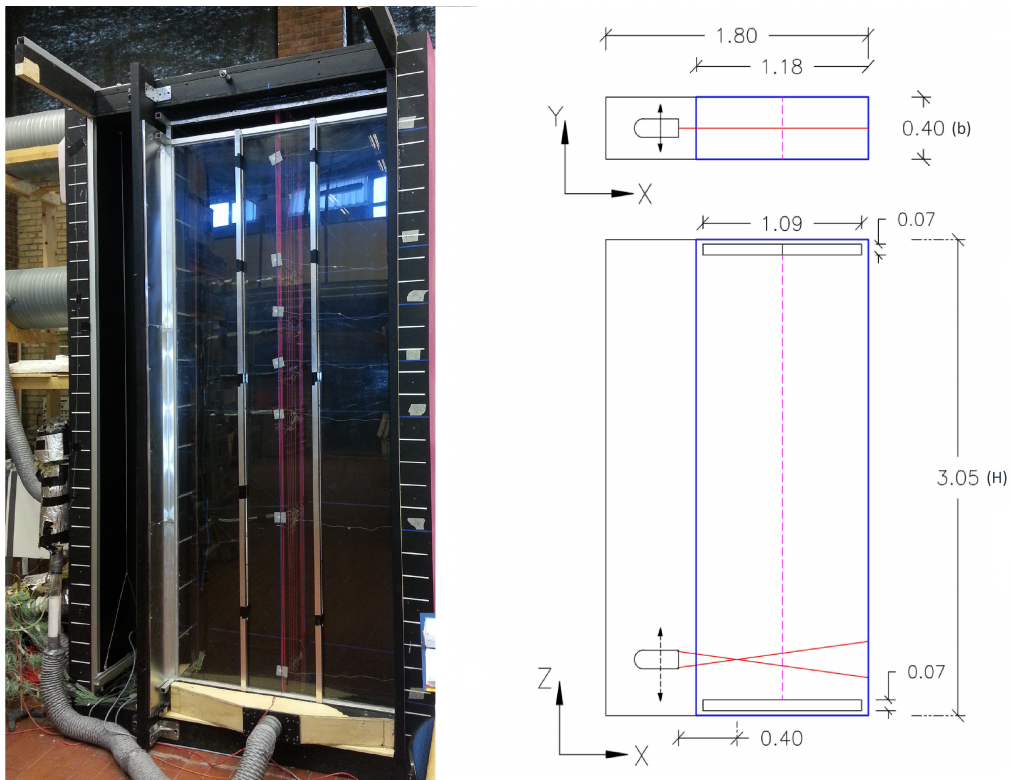


Figure 6.1. Experimental setup box geometry (meters)

On figure 6.1 - (right) can be seen the front and top view of the hot box. The values presented are the internal dimensions of the box thus not including the insulation thickness. Marked with blue is the sealed experimental volume. The laser position can be varied both

vertically and horizontally (YZ -directions). The YZ plane is the one of interest, since the flow is considered two dimensional based on the work of Mikkelsen [2015] . The aspect ratio of the cavity can be calculated as height over depth (H/b) resulting in ratio of 7,61. The inlet and outlet openings are situated on the bottom and top respectively. The thermocouples measurement are situated in the centerline of the hot box. More information about the arrangement of the thermocouples in YZ plane is available in appendix A.2.

An important note is that the thermocouples and LDA measurements are not positioned strictly in the same YZ plane. The assumption of a 2D flow is implying however, that this should not affect the results.

On figure 6.1 can be seen as well the picture of the experimental setup. It is important to note that the glass is a single piece and the framing is from the outside, serving a support function only. The glass frame is also insulated from the Plexiglas with a thin layer of EPS for the reduction of thermal bridge effects.

As it is necessary to obtain uniform heat distribution on the heated surface in the channel, the construction is formed according to figure 6.2.

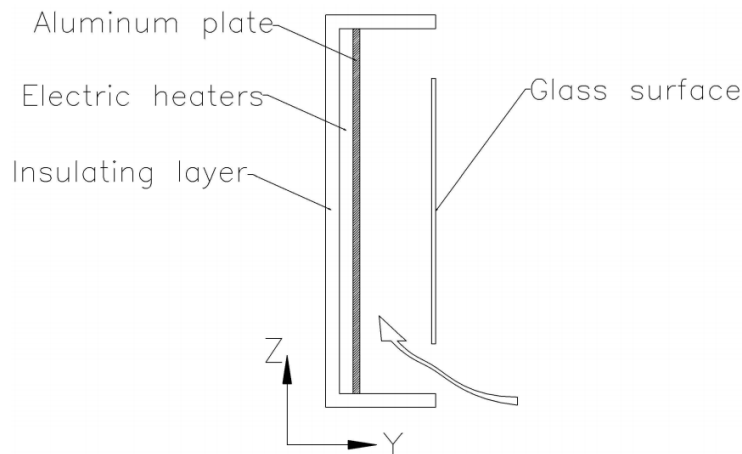


Figure 6.2. Experimental box cross section

All internal elements are painted in black, in order to be appreciated as much as possible the radiative influence from the surfaces and heaters. Additional pictures of the experimental setup can be found in appendix C on page 132

Further are explained the used equipment and measurement conditions for the considered test cases.

6.2 Equipment

On figure 6.3 is presented the scheme of the experimental setup. As mentioned before the setup is located inside a laboratory environment in a multi-functional room together with other experimental setups.

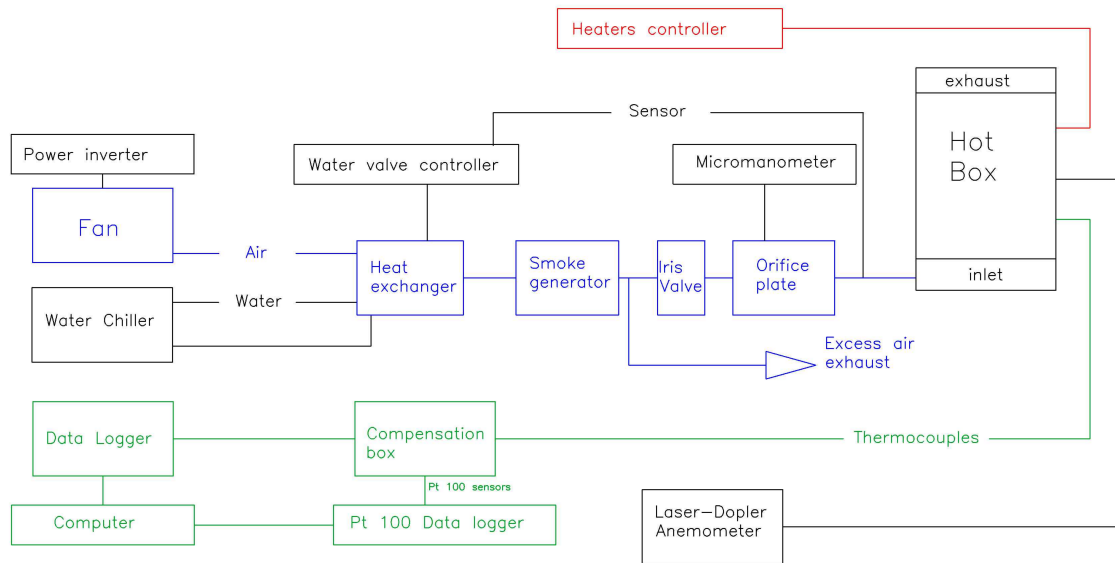


Figure 6.3. Experimental setup scheme

To perform properly the experiments, the following equipment is used:

- **Fan** - radial fan with casing
- **Inverter** - Invertec Drives IP66/NEMA 4X - controls the fan unit's flow rate.
- **Cooling machine**

The cooling machine consists of a heat exchanger (water-air) built into an insulated box, with piping for the cold water. The cold water supply is maintained at -2°C . The controller of the machine serves to operate an automatic valve for the cold water supply of the heat exchanger based on temperature measurement from PT 100 sensor. The location of the sensor is according to figure 6.3 at the inlet diffuser. The floating gain controller requires a set-point and a bandwidth settings to control the temperature. In order to maintain proper heat exchange in the cooling machine a high air flow-rate was required.

- **SAFEX - Fog Generator** - generates the seeding particles in the inlet air. According to manufacture documentation the particle dimensions vary in the range of $0.9 \div 2.5\mu\text{m}$. Due to the heating of the fog generator a supplied high air flow-rate is necessary for preventing the overheating and stop of the machine.
- **FCO510 Micromanometer**

Based on the measurements of the pressure difference on both sides of the orifice plate is estimated the supply flow-rate at the hot box inlet. The air flow-rate is controlled manually, by the air duct valves and the fan inverter.

- **Orifice plate**

Diameter of the pipe/orifice is as follow: $\phi 51.8/34\text{mm}$. According to orifice theory the pressure difference between both sides of the plate, is related to the flow-rate logarithmically. The regression of the relation can be found in appendix B.2 on page 131. Since the orifice plate regression curve was derived for 20°C a temperature

correction is necessary. The following equation gives the corrected volumetric flow:

$$q_{corrected} = q_{measured} \sqrt{\left(\frac{1.2}{\rho}\right)}, [m^3/h] \quad (6.1)$$

where:

$q_{corrected}$	volume flow - corrected, $[m^3/h]$
$q_{measured}$	volume flow - measured, $[m^3/h]$
1.2	fluid density at 20°C, $[kg/m^3]$
ρ	fluid density before the orifice plate, $[kg/m^3]$

- **Iris valve/straws duct**

To assure proper inlet flow rate a regulating device is necessary, therefore before the orifice plate is included an iris valve. The valve, in combination with the straws duct functions also as a measure to decrease turbulence in the ductwork and linearize the flow before the orifice plate. The unnecessary part of the flow is exhausted outside via an exhaust branch before the iris valve as shown on figure 6.3 .



Figure 6.4. Duct filled with straws



Figure 6.5. Iris valve

- **Carawarm Heating Mats**

The temperature of the heated wall is maintained by five electrical heating mats made from Carawarm foils and located in an insulated wooden plate. The dimensions of one mat is 600mm/1500mm and has a power of 480W. On the following figure is shown the mounting process and a thermal camera image of the functioning heaters.

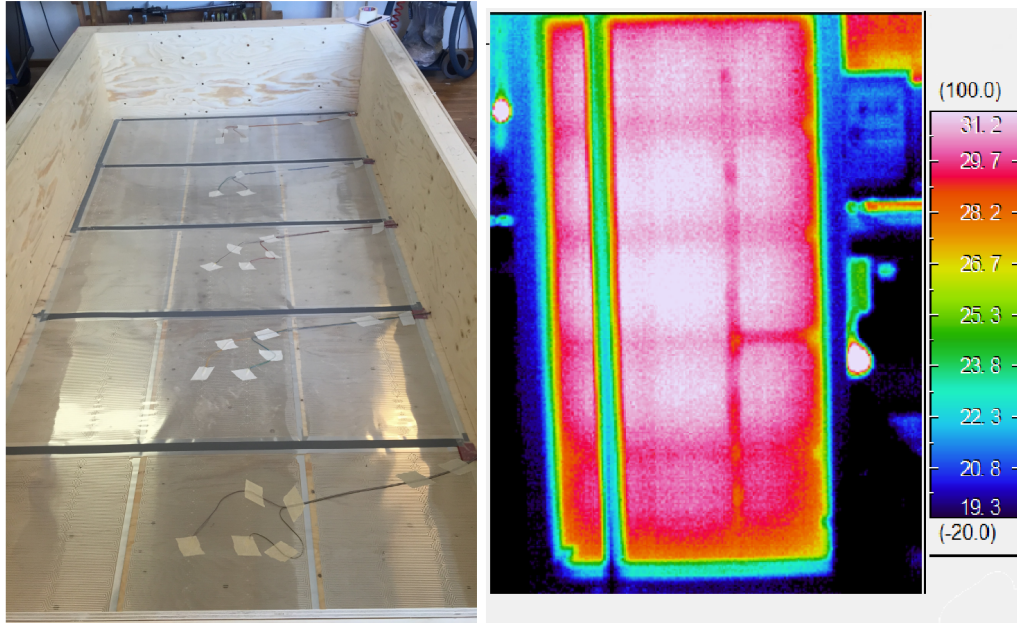


Figure 6.6. Electrical heating mats placement

The heating mats are covered with an aluminum plate to ensure a constant temperature distribution along the internal surface of the box (figure 6.2). The temperature on the aluminum plate is measured by temperature sensors - PT 100, mounted in the center of the heaters. An On/Off controller regulates the power of each heating mat with accuracy of $\pm 1^\circ\text{C}$. At later stage in the experiments the controller is upgraded to PID, with a measuring interval every 2 seconds. By changing the type of control are achieved stable temperature and the fluctuation caused by the On/Off controller is avoided.

The back of the heaters is insulated and covered with 12mm plywood. Figure 6.6 (right), shows the temperature distribution at equal set-points for all heaters. It is clear that there is small deviation from temperature for the lowest heater mat, but it is considered acceptable. Additionally it can be seen that the heaters and measurement volume centerlines do not overlap, which means that the highest temperatures achieved are situated in the left half of the volume of interest. However, the conditions are assumed acceptable.

- **Thermocouples and PT 100 sensors** For the temperature measurements of the surface and air in the box are used 97 thin type K thermocouples. They are calibrated to an accuracy of 0.086K as stated in Artmann et al. [2008] . To measure the temperature of the compensation box are used three PT 100 sensors positioned along its length. The accuracy of the sensors is estimated to 0.05K.
- **Compact Data Acquisition** - National Instruments NI cDAQ-9174, Compact data logger for PT 100 measurements
- **Compensation box** - aluminum insulated box used for thermocouples measurement.
- **Data logger** Fluke Helios Plus 2287A Data logger. Due to the large amount of thermocouples the data logger stores measurements every 10 seconds.

- **Dantec Laser Doppler Anemometer (Dantec LDA)** This device is used to measure direction and magnitude of velocity. It works on the principle of Doppler effect, where the device (LDA) emits a light beam and measures the Doppler shift of a light reflected from a moving seeding particle. Dantec-Dynamics [2002]

A basic configuration of a LDA consists of the elements shown on figure 6.7.

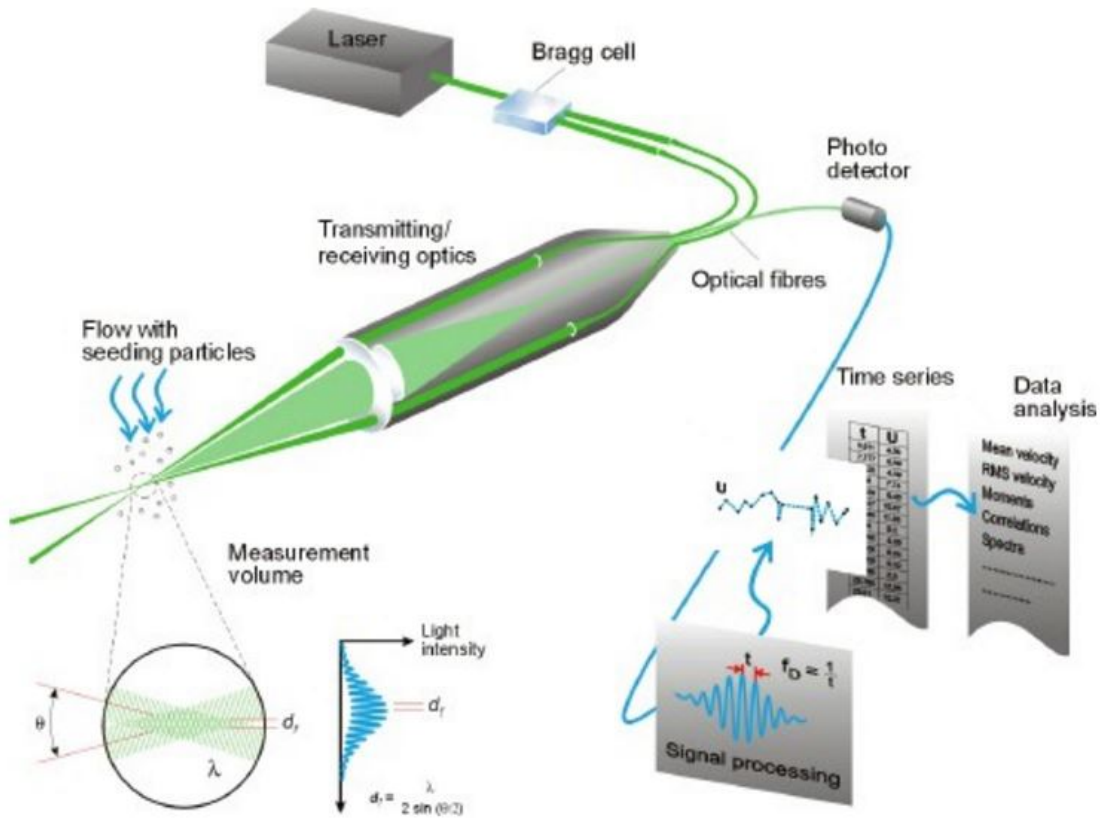


Figure 6.7. LDA configuration, Dantec-Dynamics [2016]

Explanation of the performance principle of LDA can be found in Appendix B.1. For the current experiment the following configuration is used:

Laser type	Helium-Neon laser
Wavelegth	623.8 nm (red)
Focal length	400 mm
Beam diameter	1.35 mm
Expander ratio	1
Beam spacing	38 mm

Measurements are performed in the YZ plane from the left side of the hotbox as shown on figure 6.1 , additionally the laser probe is rotated in order to measure velocities in y and z directions as illustrated on figure 6.1.

6.3 Boundary conditions

The experimental setup represents a symmetrical channel with one heated, two exposed to ambient conditions and three insulated surfaces. The setup is located in Aalborg University Clima Laboratory, where the temperature of the ambient air is maintained at 22 to 24°C during occupation hours. The setup uses laboratory air at height of 0.4 meters, and exhausts to the same at height of 3.0 meters. The excess air is exhausted outside of the building via ductwork.

Table 6.1 presents a list of the conducted experiments and their respective boundary conditions. The experiments are combined in groups depending on the varied parameter. The baseline experiment serves as a starting point for the other cases, therefore the non-varied parameters in each case are returned to the baseline set-points.

Table 6.1. Experimental cases target conditions

Group	Experiment	Heating mats temperature, [°C]	Inlet air temperature, [°C]	Air change rate, [1/h]
	Exp. 1 Baseline	28	16	4
Group I (ACH variation)	Exp. 2	28	16	3
	Exp. 3	28	16	8
	Exp. 4	28	16	12
Group II (Heater temp. variation)	Exp. 5	26	16	4
	Exp. 6	35	16	4
	Exp. 7	38	16	4
Group III (Inlet temp. variation)	Exp. 8	28	18	4
	Exp. 9	28	25	4

The controlled boundary conditions are temperature of the heated surface, inlet air temperature and ACH (air-change rate). The glass surface is exposed to laboratory conditions, therefore a temperature gradient with height is present. Other surfaces enclosing the measurement volume are considered adiabatic.

For the transparent surfaces is used cold-formed, colorless Plexiglas sheet with thickness of 6mm. The thermal conductivity of the sheet is $0.1875W/(m.K)$ and the total light transmittance - 92%, *Plexiglas - general information and physical properties* [2016].

It is well known that operative temperature is a sum of the air temperature and the mean radiant temperature. Since the inner surfaces of the hot box are painted black, the long wave radiation from all surfaces is appreciated. However it is difficult to calculate or measure the operative temperature, because it requires a different temperature transducer. Therefore, it is assumed that thermocouples are measuring only air temperature.

The experiments are considered held at steady-state conditions. Even though there occur instabilities, they mainly come from control equipment. On figure 6.8 is shown the instability due to the On/Off heaters controller. The measurement heights are labeled as in appendix A.3.

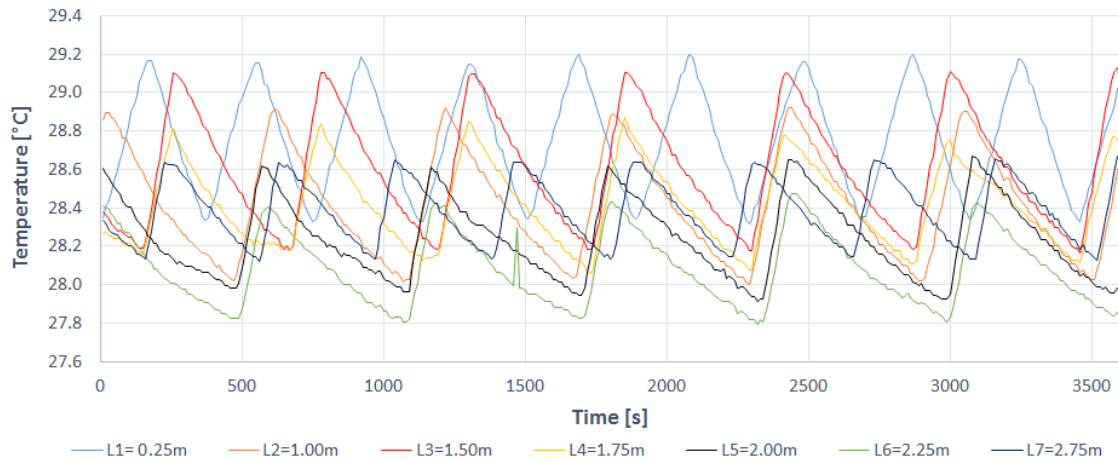


Figure 6.8. Temperatures at hot surface with On/Off controller

It is seen from the figure that the maximum value that is reached by the different heaters is around 29.2°C and minimum is 27.8°C for a set point of 28°C . After an upgrade of the experimental setup, the On/Off controller is substituted with PID. The result is stable linear temperature distribution with no fluctuations. Nevertheless the controller's step is still $\pm 1^{\circ}\text{C}$, which restricts the settings precision.

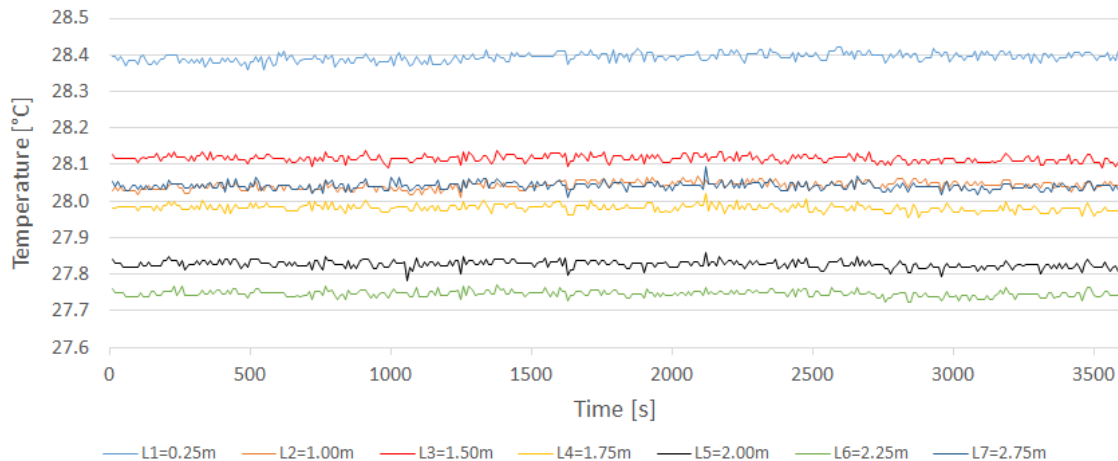


Figure 6.9. Temperatures at hot surface with PID controller

The temperatures difference arise from the before mentioned controller step of $\pm 1^{\circ}\text{C}$, and the fact that heaters temperature is higher at the center of each mat, which is visible on figure 6.6. This implies that the chosen measurement heights do not correspond to heating mats centers, therefore a deviation in the measured temperatures might be caused. However this is not considered a prerequisite for a mistake in the measurements.

Fluctuations are noticed also for the inlet air temperature. The cause is the floating gain controller used for the cooling machine. Three different temperatures are defined: upper, lower limit and set point. The margin between them is set to the lowest possible 0.1°C . This results in a varying temperature of the inlet air, which is visible on figure 6.10.

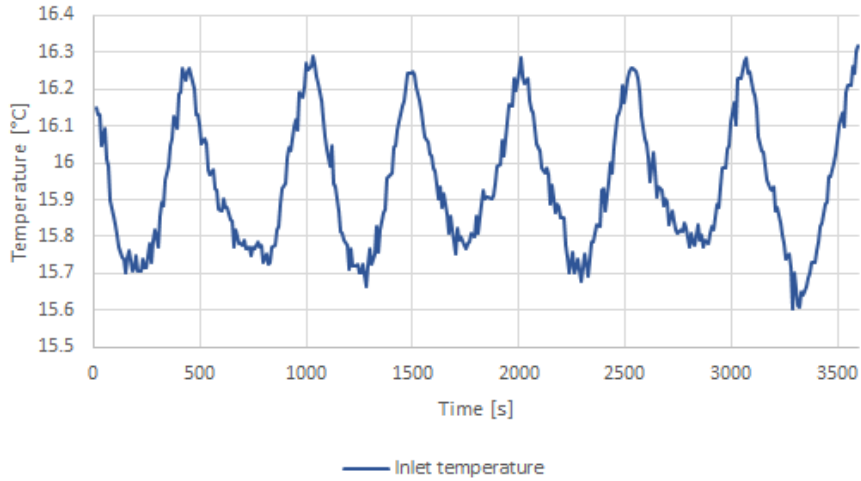


Figure 6.10. Inlet temperature fluctuation

In the cases with lower air change rate, the cooling machine was working at full power in order to maintain the necessary temperature and no control variations were noticed. In order to maintain the temperature in these cases the smoke supply was set to pulse. Nevertheless, stable seeding particles production was not interrupted.

The pressure difference at the orifice plate is measured using orifice plate and precision manometer, however the obtained value is not a constant as well. The fluctuation of the pressure difference, for the baseline experiment, during the entire experimental time is presented on the following figure.

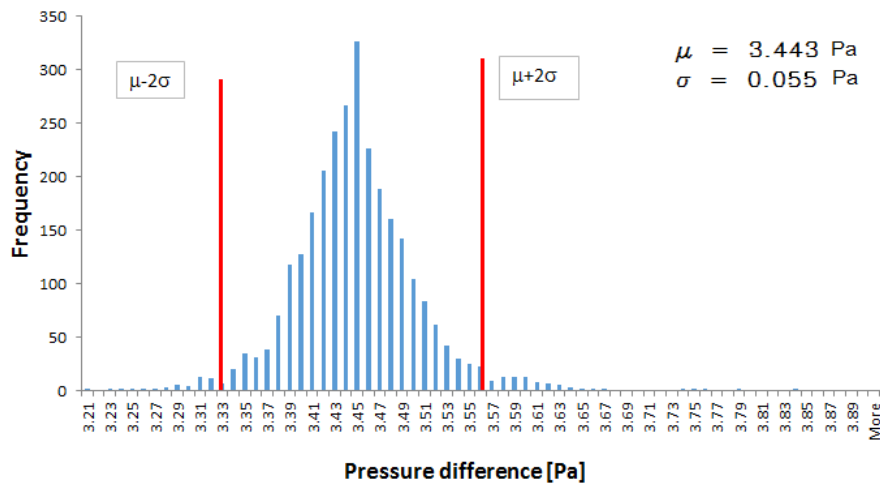


Figure 6.11. Pressure difference variation histogram - Baseline experiment

The analysis shows that 95.5% of the pressure difference falls in the area of 3.33Pa to 3.55Pa, while the mean value is calculated to 3.44Pa. In the current case the initial set-point was estimated to 3.43Pa, meaning that based on the results the flow conditions are achieved with sufficient precision. Pressure difference results can be seen graphically on the histograms in Appendix D.3, E.3 and F.2 for each of the experimental cases.

Anyway, since the regression curve for the orifice plate is not linear but logarithmic, the influence of the flow deviation can vary from negligible to significant. The logarithmic regression for the orifice plate can be found in Appendix B.2. A table with experimental results and deviation from the targeted flow-rates for all experiments is shown bellow:

Table 6.2. Volumetric flow rate deviation

Experiment	Exp. 1	Exp. 2	Exp. 3	Exp. 4	Exp. 5	Exp. 6	Exp. 7	Exp. 8	Exp. 9
ACH [1/h]	4	3	8	12	4	4	4	4	4
Vol. flow \dot{V} [m^3/h]	5.67	4.25	11.34	17.02	5.67	5.67	5.67	5.67	5.67
\dot{V} avg [m^3/h]	5.68	4.28	11.35	16.99	5.60	5.63	5.71	5.57	5.53
\dot{V}_{min} [m^3/h]	5.49	3.85	11.09	16.46	5.36	5.44	5.45	5.41	5.37
\dot{V}_{max} [m^3/h]	5.99	4.67	11.63	17.22	6.07	5.93	5.87	5.95	5.88
$\Delta\dot{V}$ [m^3/h]	0.50	0.83	0.54	0.75	0.71	0.48	0.42	0.53	0.51
$\Delta\dot{V}$ [%]	8.81	19.42	4.77	4.41	12.51	8.51	7.39	9.42	9.03

The top part of the table gives information about the expected volumetric flow according to the air-change rate. The bottom part presents the experimentally obtained values. It can be seen that with increase of the air-change the volumetric flow rate deviation decreases, due to the before mentioned pressure logarithmic relation. The data presents the entire volumetric flow rate variation (ΔV) in all of the experimental cases. The volumetric flow-rate variation ΔV is based on the extreme measured values, which constitute only small percentage of the measuring time. The biggest range for flow rate deviation is for Exp. 2 (ACH 3) with 19.42%, while the lowest one is for Exp. 4 (ACH 12) - 4.41%. Conditions with lower ACH are difficult to maintain stable during the experimental procedure, due to decreased heat exchange potential of the cooling machine, which consequently influence the inlet air temperature.

Experimental results and analysis 7

The experiments presented in this chapter are evaluated by three parameters: temperature at the surfaces and central plane of the cavity, velocity and dimensionless criteria derived from the obtained measurements.

A recent study by (Mikkelsen [2015]) proved that the flow inside the same type of channel can be approximated as two dimensional (2D) in directions along the height and the depth of the cavity (YZ-plane). Therefore, it is reasonable to present the data in a way that the mentioned above directions are leading.

As the YZ-plane is the one accommodating all measurements, for further convenience the reference point in horizontal direction is considered the hot surface. For velocity results, the index "*hot + 6 ÷ 38cm*" will mean distance from hot surface between 6 and 38 cm. In vertical direction from bottom to top the measurements start at 0.25 m to 2.75 m with spatial resolution of 0.25 m.

For temperature measurements the used indexing is as in Appendix A.3.

In the subsections for temperature measurements the focus is set on the vertical and horizontal temperature distribution inside the gap. The temperature data is logged every 10 seconds for the entire period of a velocity measurement (4 to 5 hours). Because of the big amount of data, an approximation is made for the discussed temperature graphs, for a five minute representative period from the entire data series.

The overall temperature field at the measurement plane is presented as a contour plot. A piecewise cubic spline interpolation is used to obtain information about the temperature distribution between measuring points. The polynomial has a third order of accuracy. The first step is to interpolate in horizontal direction (y direction) the temperature in all measuring levels by obtaining an exact value for every millimeter of the gap width. After that the same principle of interpolation is applied in vertical direction with a step of 0.01m.

On figure 7.1 on the next page is shown the horizontal velocity distribution for Base experiment, together with the horizontal piecewise cubic spline interpolation. For the regions with no temperature measurements, the cubic spline smooths the results and might be the cause of an error. However, this method of results presentation is considered

sufficient and representative for the temperature field inside the cavity. In the legend "L1" to "L7" represent the height of levels in ascending order where thermocouples are positioned. In appendix fig. A.3 on page 128 the levels are labeled.

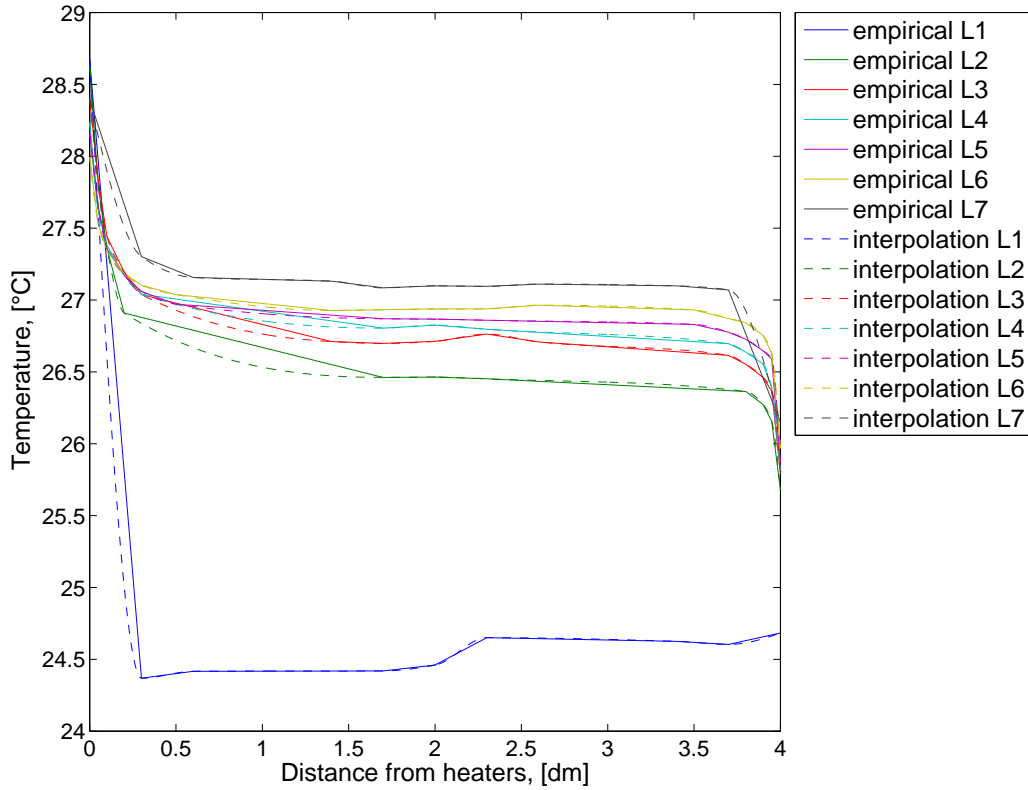


Figure 7.1. Temperature field - Piecewise interpolated based on discrete measurement points (baseline experiment)

Further in the analysis several graphs show the stability of averaged temperatures for different time periods. The aim is to show the regions with fluctuations and conclude about their cause. Intervals of 20sec, 30sec, 1min, 2min, 5min, 10min and 20min are targeted. The evaluation accounts for the instability of temperature with time for given measuring point.

In the subsections considering the velocity measurements a vector velocity plot will be used as a representative method for flow evaluation. The measurement grid constitutes of 11 levels starting from 0.25m to 2.75m in vertical direction and from 0.6dm to 3.8dm away from the heated surface, with step of 0.2dm, in horizontal direction. The measurement of velocities in the entire cavity, with the chosen step takes four to five hours. The measurements are done by consecutively moving the LDA probe at each point and logging the horizontal and vertical components of velocity vector. For each point from the velocity measurements are collected 15 000 samples, ensured validation of above 99 % and Gaussian samples distribution. The samples number is chosen based on the recommendation for statistical analysis, which requires above 10 000 samples for correct flow evaluation. The

average time for data acquisition in one point takes $1 \div 2$ minutes including the time for laser positioning and data extraction.

On figure 7.2 is presented the typical result window obtained by a single measurement of one velocity component.

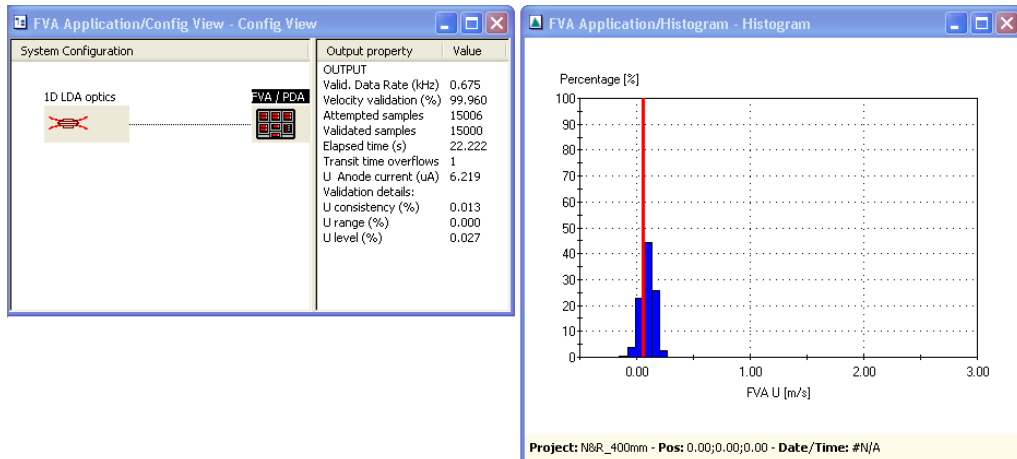


Figure 7.2. Laser Doppler Anemometer - data acquisition

Analysis of the velocity for a single point is done also in the form of histograms. The presented point in this case is at height 2.75 meters and 38 cm away from the hot surface for the base experiment case. This point is chosen only for visualization of the current plots, further will be discussed deeper the results for specific points of interest.

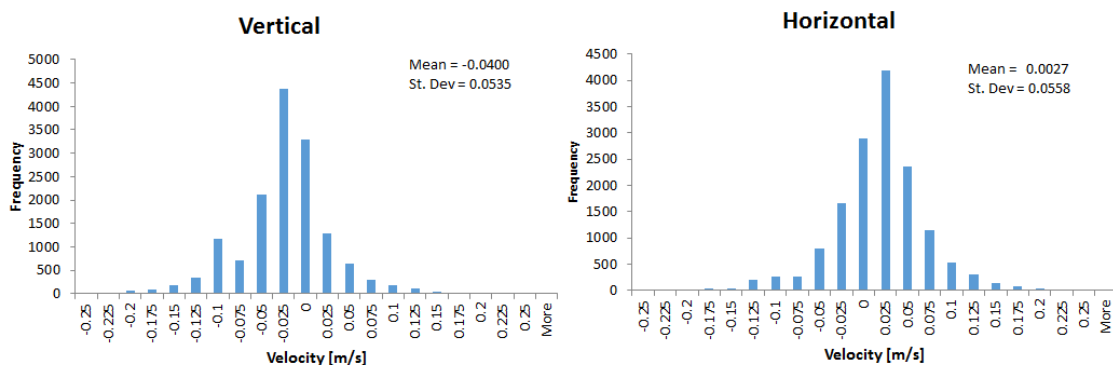


Figure 7.3. Vertical and horizontal velocity distribution (2.75m, hot+38cm, Base)

Another way to analyze the data is by observing the process of acquisition, which is presented on figure 7.4.

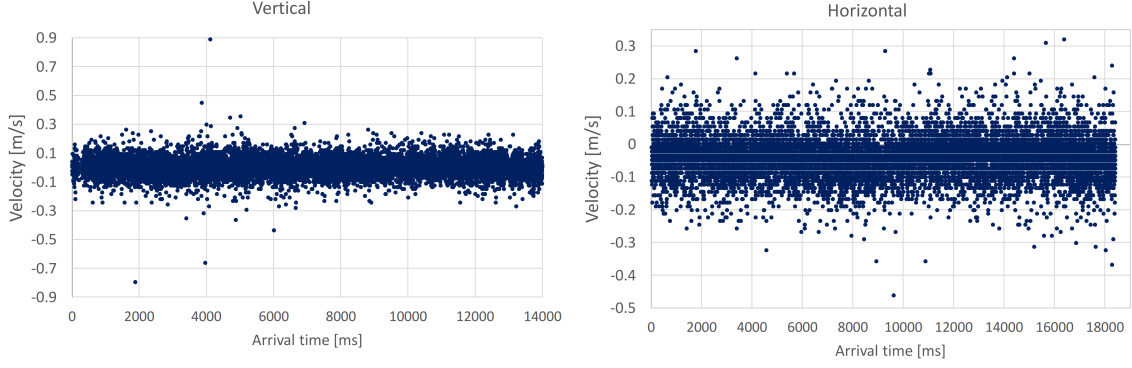


Figure 7.4. Velocity-Acquisition time plots(2.75m, hot+38cm, Base)

It can be noted that the time for collection of the samples differs for each point. Moreover, the data collection also depends of the particle density inside the cavity. As mentioned earlier stable supply of seeding particles was ensured. This can be confirmed by the continuous data arrival throughout the entire sampling period.

Figure 7.4 also shows the collected samples according to time for single point. The horizontal velocity samples are collected longer than the vertical, which is not the general case for all experiments. In the vertical data-set can be seen couple of over and under-shoots from the clustered data. Those samples represent 0.1% of the whole data set and fall outside the 3σ area, so their significance is negligible.

Analyzing the horizontal (y) and vertical (z) velocity components separately does not present the full picture. Therefore in all further analysis is used a combined vector derived from a square root of the sum of squared y and z average velocity components. It is used for qualitatively and quantitatively description of the velocities. For the vector plots is used the command "quiver" in MATLAB, which based on the coordinates of the point, plots vectors with magnitude of the combined velocity. In addition is made a contour plot, which facilitates the observation of higher and lower velocity regions and patterns. In this way the velocity zones are much easier to differentiate.

Analytical estimation of the hot surface boundary layer thickness is done and later compared to the empirical results. The calculation is performed based on the work of Eckert and Jackson [1951]. It is argued that this report has weaknesses and does not properly correspond to theory, however the results are assumed as acceptable for engineering applications. More information can be found in Larsen [2008] and in the original report. The following formula is used for calculation of the velocity boundary layer, although in Eckert and Jackson [1951] the temperature and velocity boundary layer are not clearly differentiated:

$$\delta = 0.566 \cdot z \cdot Gr_z^{-\frac{1}{10}} \cdot Pr^{-\frac{8}{15}} \cdot [1 + 0.494 \cdot Pr^{\frac{2}{3}}]^{\frac{1}{10}} \quad (7.1)$$

where:

z		Height, [m]
Gr_z		Grashof number with regard to the height of the cavity, [-]
Pr		Prandtl number, [-]

Since the flow conditions are considered highly dynamic, and the LDA measurements take relatively long time, stability of the flow analyses are necessary. For this analysis the full data-set of 15 000 samples is split into several sets of 1000, 5000, and 10 000 samples starting from the first value of the full data set. The average value from each group is compared to the full case. The comparison is presented in terms of vector plots. This is done in order to study the instabilities of the flow with time and differentiate the regions with dynamic conditions. Figure 7.5 shows a sample of the vectors stability plot for a single point from the base experimental case.

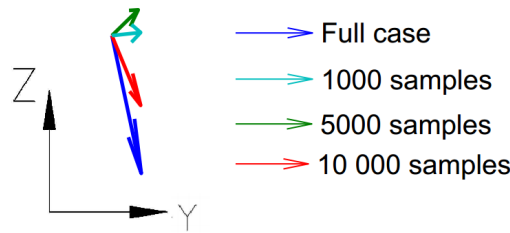


Figure 7.5. Example vector stability (2.50m, hot+34cm, Base)

The acquisition times (arrival times) for the different data-sets are extracted to show their variation with decrease of the number of samples. It is clear that the decrease of the sample number decreases the accuracy of the averaged values, but gives the opportunity to analyze the velocity fluctuations with time, which is necessary in highly dynamic flows. On figure 7.6 is visible that at different locations at the same height the acquisition time is varying unpredictably. However, with the decrease of the number of samples, the time is also decreasing, which implies that samples arrive steadily throughout the logging period. On the other hand, the acquired data needs to be transported to the computer, which leads to a delay equal to a few hundreds microseconds. This is negligible compared to the measurement time.

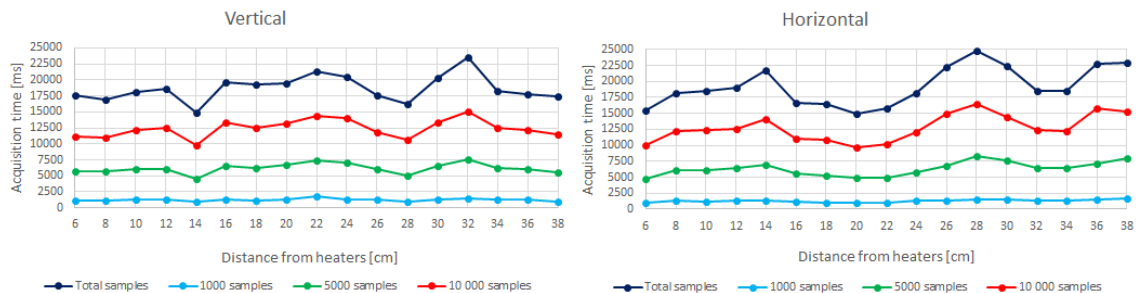


Figure 7.6. Velocity acquisition time for stability at height of 2.50m, Base exp.

Another data analysis is done with regards to the turbulence inside the cavity. Turbulent

kinetic energy and turbulence are calculated according to equations 7.2 and 7.3. In this analysis are averaged the entire data series (15 000 samples) for v -horizontal and w - vertical velocities. Simultaneously from the full datasets is calculated the standard deviation for each point and direction. The analysis are expected to show turbulence levels for the various experimental cases.

$$K(y, z) = \frac{1}{2} \cdot [v'^2 + w'^2] \quad (7.2)$$

$$T(y, z) = \sqrt{K(y, z)} \quad (7.3)$$

$$F(y, z) = \sqrt{v'^2 + w'^2} \quad (7.4)$$

where:

K	Turbulent kinetic energy [m^2/s^2]
v', w'	Standard deviation of horizontal/vertical velocity component, (STD), [m/s]
v, w	Average horizontal/vertical velocity component, [m/s]
T	Turbulence, [m/s]
F	Velocity fluctuations depending on time, [m/s]

In similar manner is done another data treatment based on the full set of 15 000 samples. In this case is estimated the average velocity fluctuation with time. To do so, are averaged each 1000 samples of the full dataset, and based on the standard deviation of the averaged values are estimated the fluctuations. It should be noted that the standard deviation is presented as an absolute value, so no information about the direction of the fluctuation is present. The figure bellow gives simple overview of the process.

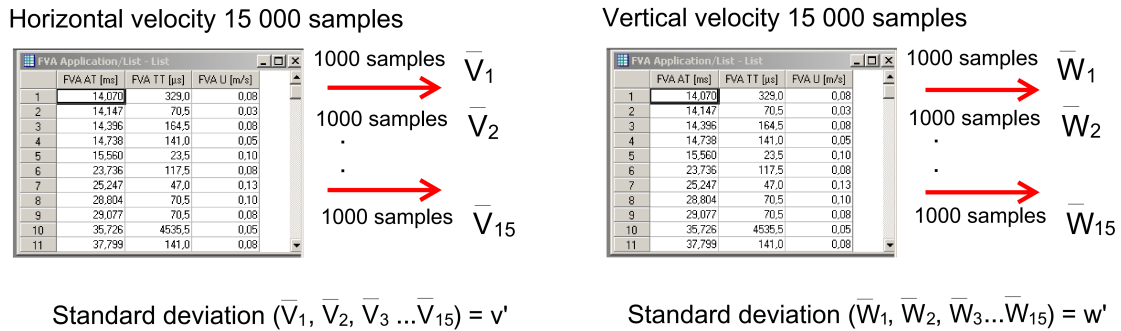


Figure 7.7. Data treatment for velocity fluctuations plots

The used \bar{V} and \bar{W} denote the averaged value of each set of 1000 samples. After obtaining the fluctuations v' and w' equation 7.4 is used for the calculations of the

velocity instabilities with time. With this equation are combined the horizontal and vertical instability from the results. In this way can be seen the zones where the measured velocities were varying the most throughout the acquisition period.

Also a short description of the moving average concept is included as a used method for data treatment. The analysis is done by creating a subset of 500 samples out of the full datasets (15 000), and then averaging it. After that to the subset is included the next entry of the full dataset and is removed the first entry of the previous subset. This leads to the same number of samples inside the subset, and a different average value. In this way it is easier to be visualized the velocity throughout the measurement period.

Further the dimensionless analysis include calculation of Rayleigh, Grashof, Reynolds, Prandtl and Gr/Re^2 criteria. This allows a comparison between different experimental cases and other investigations. It is worth mentioning that for those calculations are used:

- V - Velocity at the cross-section of the cavity based on measured volumetric flow rate, $[m/s]$
- T_∞ - Empirical inlet air temperature, $[K]$
- β - Coefficient of thermal expansion - calculated regarding the empirical average integral temperature for middle of the gap, $[1/K]$
- T_s - Empirical average integral temperature at the glass and heated surface, $[K]$
- l - Characteristic dimension is the height (H) of the cavity, $[m]$
- H/b - Aspect ratio of height over depth of the cavity, $[m/m]$

All physical properties of air are interpolated by piecewise cubic polynomial with respect to the empirically obtained temperature. The tabulated data used for the physical properties of air is presented in appendix G.1.

The average integral temperatures inside the cavity are calculated numerically for the previously mentioned five minute period of data by using Trapezoidal rule for the estimation of the integral area below the curve. The trapezoidal rule is second order accurate and is considered sufficient for the aim of this paper. The usage of hot and cold surface temperatures is done in order to be obtained the difference in the dimensionless parameters regarding both surface temperatures of the asymmetrically heated channel. This gives the possible range of variations of the dimensionless parameters inside the cavity.

The velocities used in the calculation of Reynolds number are based on the estimated flow rate at the inlet opening divided by the area of the cavity's cross-section.

7.1 Baseline experiment

The experiments are planned, so that the set points conform with the equipment characteristics. The boundary conditions for the baseline case are situated in between the possible range of variation. However, there is certain correlations among the parameters which restrict all possible combinations of boundary conditions.

The data presented below corresponds to Baseline experiment (Exp. 1) from table 6.1. The experimental case was repeated several times, in order to study better the flow

and temperature variations. The empirical boundary conditions for all four cases are summarized in table 7.1.

Table 7.1. Baseline experiment boundary conditions for 4 cases

Case №	Heating mats controller	$T_{heaters}$, [°C]	T_{glass} , [°C]	$T_{gapcenter}$, [°C]	T_{inlet} , [°C]	$T_{laboratory}$, [°C]	\dot{V} , [m ³ /h]
1.1	PID	27.91	26.02	26.48	15.77	23.72	5.68
1.2	PID	28,01	26.28	26.68	15.89	24.18	-
1.3	On/Off	28.21	25.71	26.42	15.89	21.93	-
1.4	On/Off	28.40	25.69	26.45	15.78	22.43	-

When referring further to the baseline experiment should be considered case 1.1 from table 7.1. This case is chosen as representative from all baseline experiments. Columns 3,4 and 5 from the table give the average integral temperature respectively for the heaters, glass and gap center. It can be seen that every case has a slightly different boundary conditions. The biggest variation is noticed in the laboratory temperature, which was unable to control. The \dot{V} column presents the average volumetric flow rate measured at the orifice plate. The value is close to the desired set point. Unfortunately, volumetric flow rate data is available only for Case 1.1, the rest of the cases have similar flow rate conditions monitored manually.

To obtain more precise overview of the temperature differences inside the cavity are plotted figures 7.8 and 7.9 . They visualize that even though the average integral temperatures from table 7.1 are very close in magnitude, the temperature field in height can vary significantly between the cases.

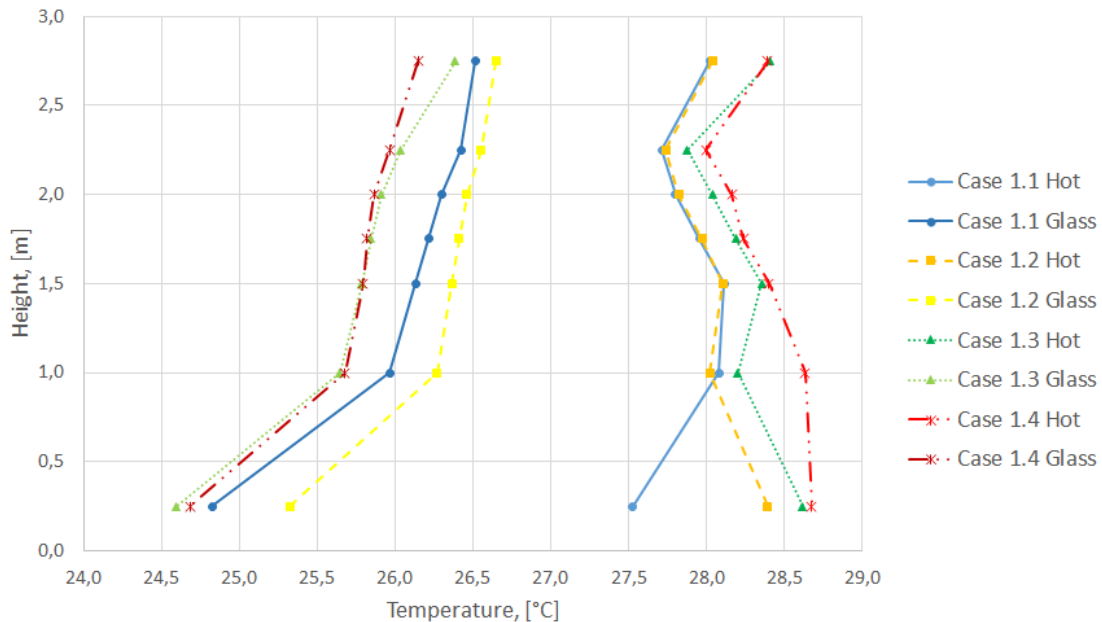


Figure 7.8. Vertical temperature distribution of heated and cold surfaces for Cases 1.1 to 1.4

At the right side of figure 7.8 are compared all vertical temperature distributions along the

heated surface. It could be noticed a similar pattern between the lines above 1.5m height, however the zone below that level is varying depending on the temperature set points of the heater's controller. Case 1.1 and 1.2 have identical temperatures excluding level 0.25m due to the PID controller, while the cases with On/Off controller have higher deviations in temperature. At the left side of the figure are presented the temperatures close to the glass surface. They have the same curve, however their values are strongly dependent on the laboratory temperature. Case 1.3 and 1.4 are made in similar conditions during March, when the laboratory temperature is lower, while Case 1.1 and 1.2 are performed in the end of April, when the heat gains are increased.

Regarding the core vertical distribution inside the cavity on figure 7.9 , cases 1.1, 1.3 and 1.4 have almost the same temperature, while case 1.2 is deviating with around a degree at the lower level and less in the upper ones. The most stable ambient conditions were for Case 1.1, therefore it is chosen for the baseline experiment.

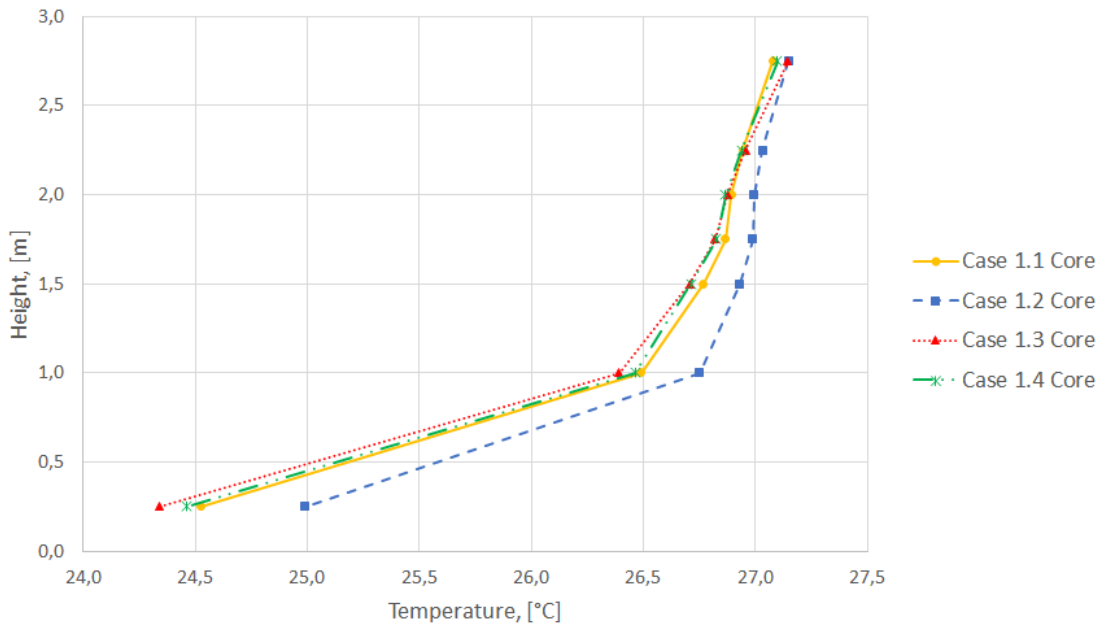


Figure 7.9. Vertical temperature distribution in the core of the cavity for Cases 1.1 to 1.4

7.1.1 Video flow visualization

In order to obtain basic knowledge about the flow pattern in the cavity a video is made with extreme smoke supply. It is accounted for the high-rate smoke generation not to disturb the regular steady state conditions and deviate the flow pattern. Videos of all filmed experiments can be found on the memory drive attached to this report. However, in this subsection snapshots from the video will be evaluated.

Since the height of the cavity is significant and the hot box left wall is restricting the cameras distance from the glass, two cameras record the flow development. They are positioned in a way that at the center of the cavity the two videos overlap. A principle scheme of the cameras location and capturing angle is shown on figure 7.10.

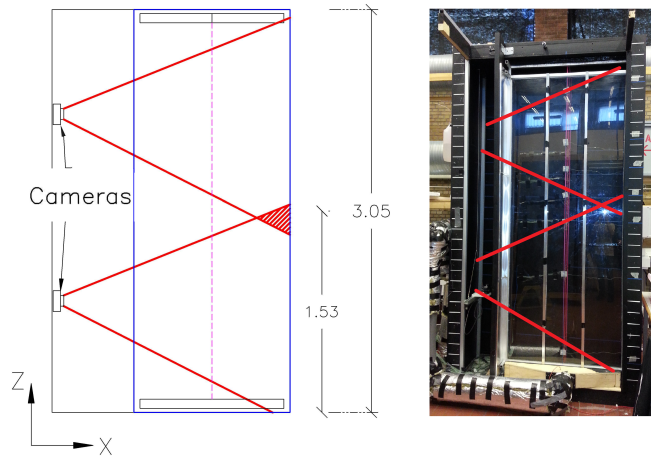


Figure 7.10. Cameras capturing zones

The video capturing is mainly considered as an auxiliary information and serves for deriving initial assumptions and guesses.

On the figure bellow are presented snapshots from the lower part of the cavity. On the left side is the heated surface and right side is the glass surface. The accounted time stamps start at the moment when smoke enters the cavity.

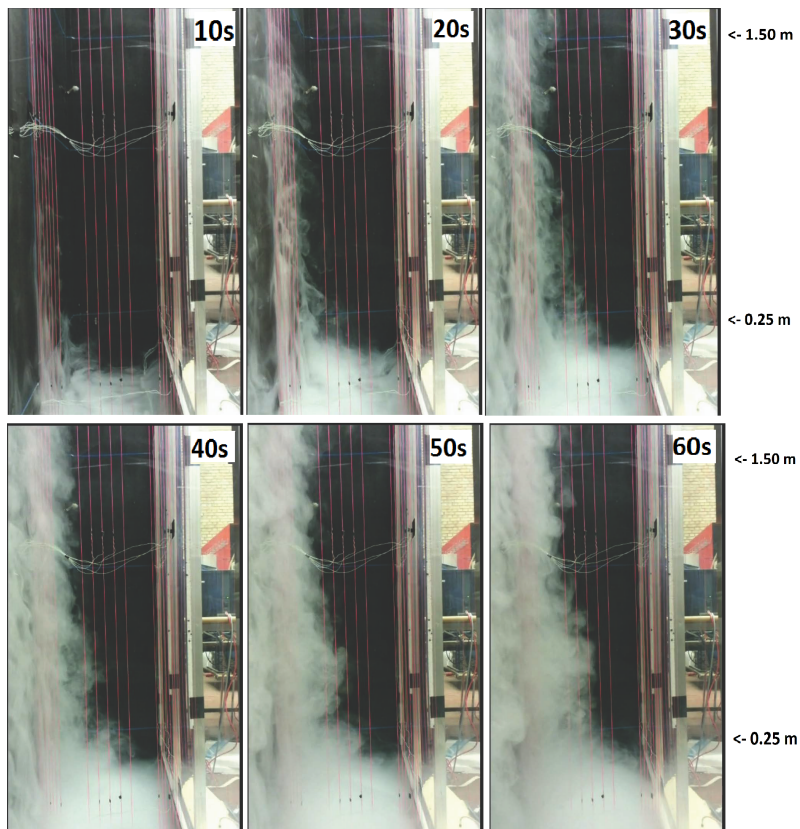


Figure 7.11. Flow visualization with smoke (0.25m to 1.50m) - from 10 to 60sec. with time step 10 sec. for Case 1.4

The video clearly presents that the flow rises along the heated surface, due to the buoyancy effect. It is noticed a formation of vortices (eddies) at the edge of the hot surface boundary layer with an unstable manner. They grow and collapse unpredictably. Based on that an assumption can be made that the flow is turbulent. This will be later validated or rejected by dimensionless numbers analysis.

The video presents also that at height above 0,50m some of the formed eddies increase their penetration in direction toward the core of the cavity. Those eddies are stretched due to the high velocity difference in the gap center and boundary layer.

The formation of the strong hot boundary layer for the lower part of the cavity is presented for period of 60 seconds on figure 7.11. The eddies are also visible, however their stagnation when penetrating towards the center can be observed only in the video.

In the upper part of the cavity the smoke is not so dense due to mixing with the surrounding air, which impedes the analysis of vortices.

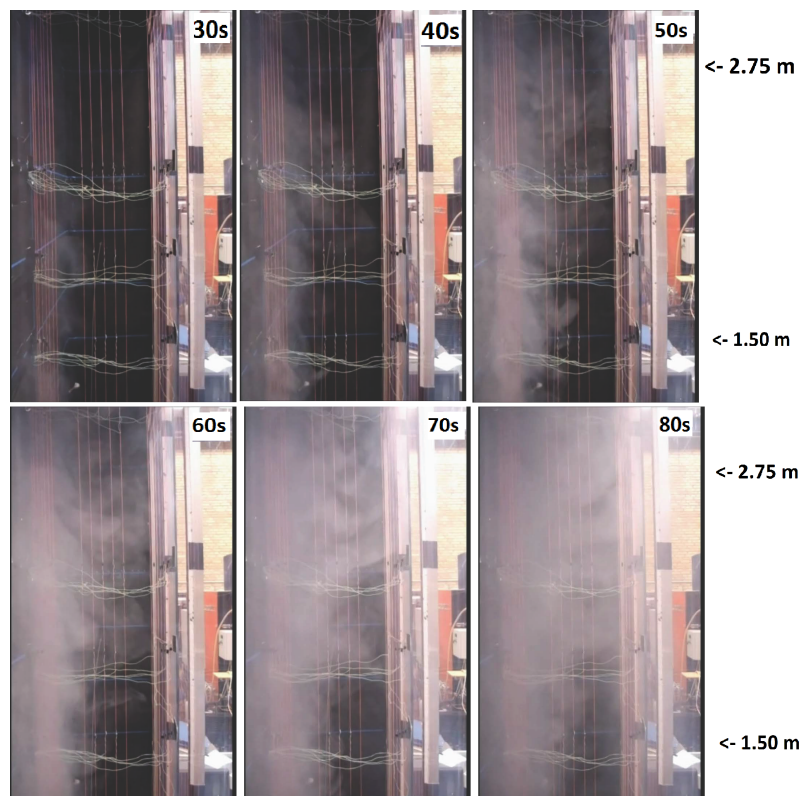


Figure 7.12. Flow visualization with smoke (1.50m to 2.75m) - from 30 to 80sec. with time step 10 sec. for Case 1.4

The first thing that can be observed is that the developed boundary layer at height around 2.0m ends its increase and instead decreases half its width. A reason for that can be influence of the ceiling of the facade. The flow is slowly entrained to the middle of the gap and consequently redirected towards the cold surface. Reaching the cold surface the smoke starts slowly dropping along it. The flow is assumed to supply the descending cold boundary layer development. An illustration of the observations is shown on figure 7.13 .

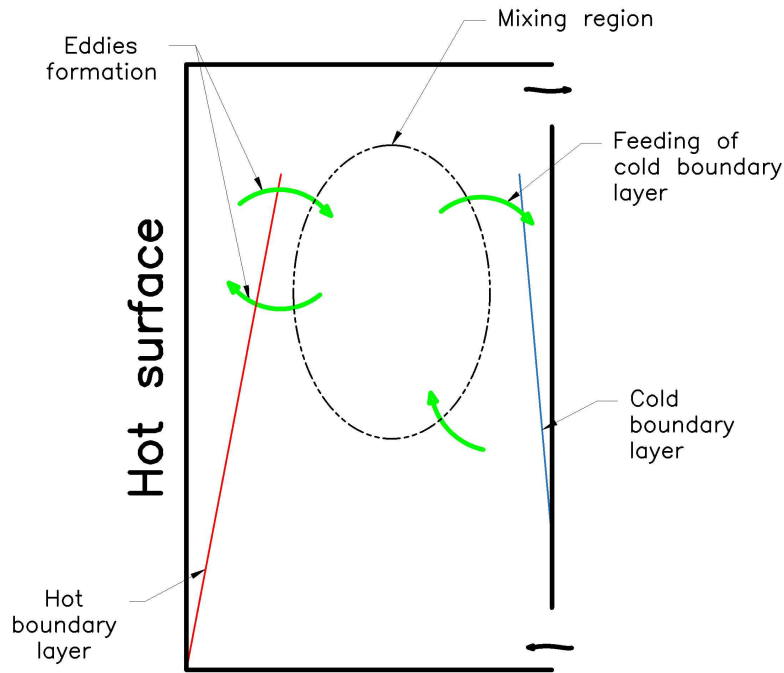


Figure 7.13. Flow movement inside the cavity

After the upper part of the cavity is well mixed the smoke slowly spreads first close to the cold surface and after that inside the lower half of the core. In the lower part of the cavity was observed as well the height at which the cold boundary layer terminates. In this experiment that happens at height of around 0.55 m.

7.1.2 Temperature distribution

In this subsection will be presented the five minute average temperature distributions and analysis obtained for Case 1.1. Also there will be provided the justification of using the 5min average values as representative for the thermal distribution in the cavity.

Horizontal temperature distribution

The horizontal temperature distribution is used to show the thermal differences between the hot and cold surfaces. The zones with similar temperatures can be easily distinguished from the rest and serve as a starting point for further observations.

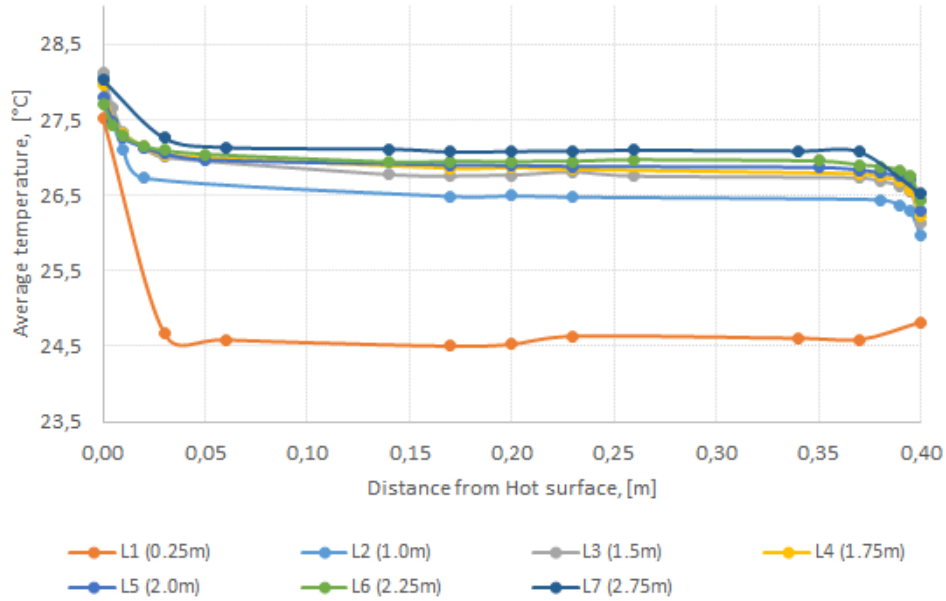


Figure 7.14. Horizontal temperature distribution (Case 1.1)

In this figure the heated surface is positioned on the left, while the cold one is on the right side of the graph. It makes an impression that the temperature of the first level (L1) is lower than the rest. It could be explained by an influence from the inlet air ($T_{in} = 16^{\circ}\text{C}$), since the inlet is positioned only a few centimeters below L1. The temperature increases slightly with level height until it reaches L2. At heights between L2 - one meter and L7 - 2.75 meters in the center of the gap can be seen less than 1°C difference. Furthermore, temperatures at each level are mostly linear in the vicinity of the gap's core.

From figure 7.14 can be estimated the thermal boundary layer. It is defined as the section of the flow in which a temperature gradient exists. However, the thermal gradient disappears in the interpolated region between the measuring points. In that way a specific numerical value for the maximal boundary layer thicknesses cannot be stated. Nevertheless, a wider hot boundary layer is expected due to buoyancy forces and assistance from the core flow, while for the cold surface the main flow is opposing.

Vertical temperature distribution

The vertical temperature profiles can be used to conclude about existence of no temperature gradient regions as shown on figure 4.12 on page 26. Therefore, the vertical temperature distribution of five different locations inside the cavity are presented.

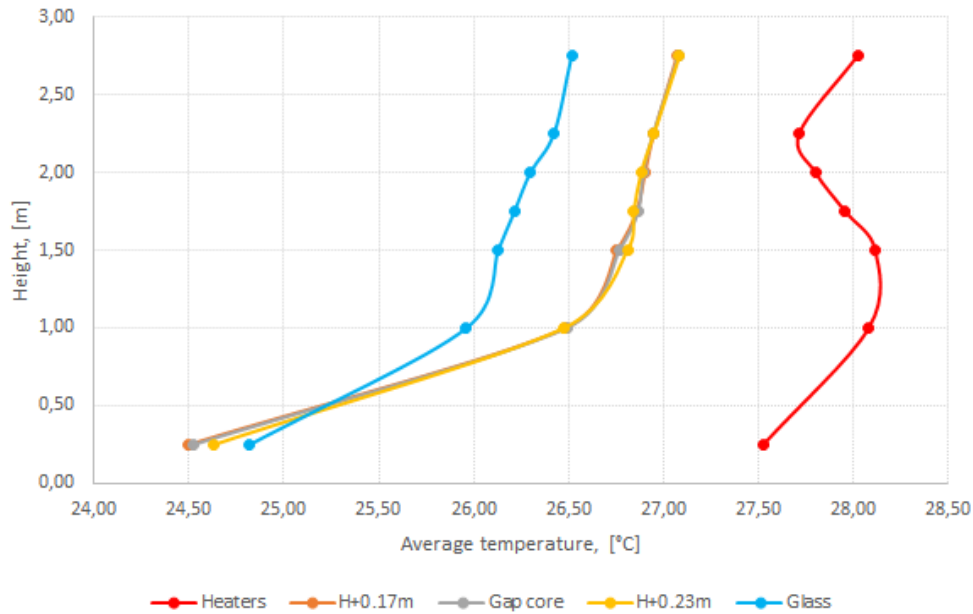


Figure 7.15. Vertical temperature distribution (Case 1.1)

The hot surface profile (on the right) shows the difference in the heaters temperatures with height. Here can be noticed the inability of precise control of the heaters temperatures, which is included as a set up limitation. However, the difference is not significantly high and is assumed acceptable.

In the core of the cavity and ± 3 cm away in y direction the temperature gradient is small and a linear profile is visible above 1.5 meters. This does not correspond precisely to the statement attached to figure 4.12, so a conclusion for lack of temperature gradient cannot be made.

At the bottom of the figure the temperatures at the core decrease and cross the glass (cold) surface temperature. This is due to the supplied cold inlet air. At the glass surface is visible the temperature gradient imposed by the laboratory conditions.

Temperature stability in time

A different method in this report for analysis of temperature is the temperature stability in time. The changes in temperature can be used as a guideline for estimation of focus zones. On the following figures is presented data for a period of 20 minutes, where the time interval is split to sets from 20 seconds to 20 minutes. The reader should be careful when comparing the graphs due to differences in y axes. The purpose of this method of analysis is to show that the employed period for temperature averaging is representative enough for the entire experiment. On figure 7.16 are presented the vertical temperature distributions close to the heated surface up to 2 cm distance in y direction.

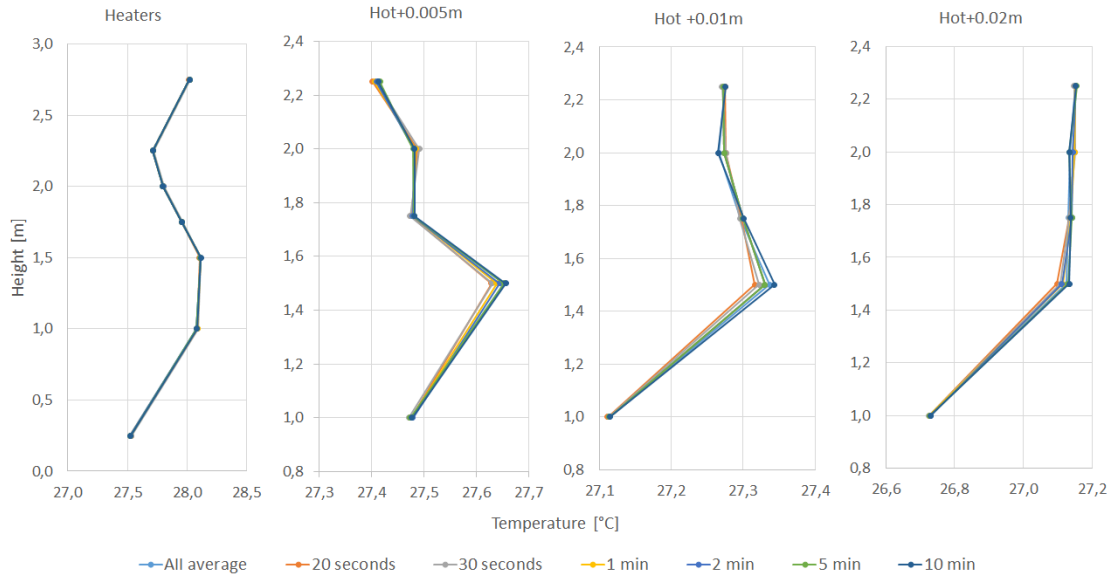


Figure 7.16. Temperature stability close to heated surface (Case 1.1)

It can be observed that the temperature at the heated surface is stable for the given period of 20 minutes. However, deeper in the cavity are noticed temperature fluctuations in time with a magnitude lower than the precision of the thermocouples. Therefore, no conclusion can be derived for the flow behavior and the temperature is assumed to be stable enough.

Different perspective can be found in the last graph on figure 7.16, where a straight vertical line is visible for the points above 1.5m. The fluctuations are so small that it can be defined as a zone without temperature gradient in vertical direction. Referring to figure 4.12 a similar pattern of the temperature can be observed, which is a sign for well mixed zone.

Figure 7.17 gives information for the temperature distribution close to the glass surface and up to 2cm inside the cavity. The same stable temperature conditions are visible for the glass, however a slight instability is present deeper in the cavity. The pattern is linear from above 1 meter height. In ideal cases the temperature gradient inside the laboratory should be as well linear, but the glass temperature profile is slightly changed in the lower region, below 1 meter. This is the zone influenced by the penetration of the inlet air. Additionally, the well mixed zone observed close to the heated surface is not present at the cold one.

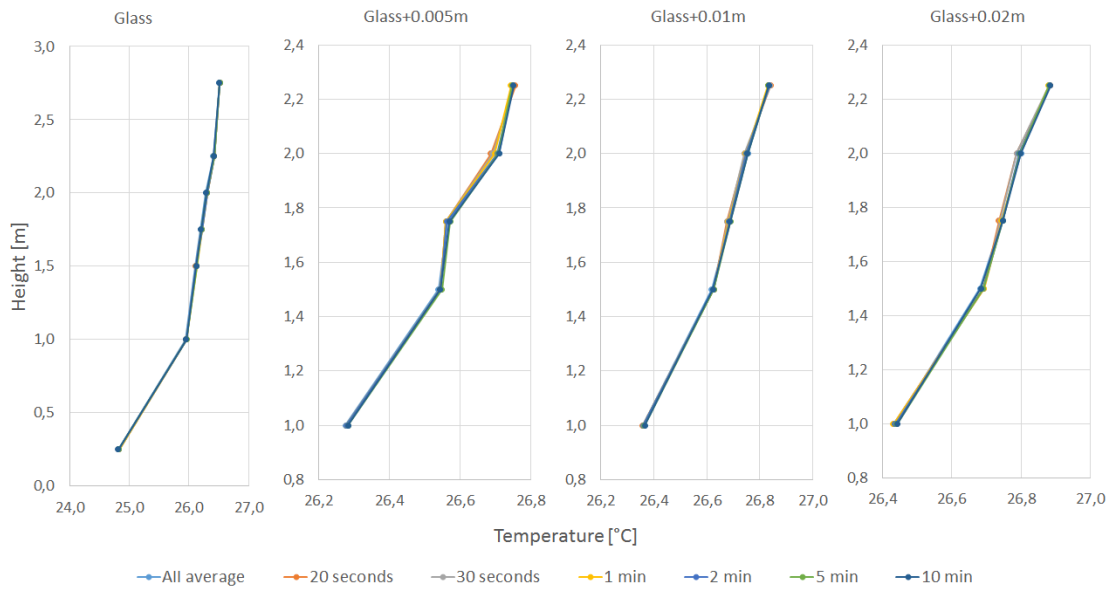


Figure 7.17. Temperature stability close to glass surface (Case 1.1)

Another observation is made based on the vertical temperatures at 3 cm away from both surfaces and deeper into the cavity. No temperature fluctuations were noticed in that case. The temperature is stable and increases slightly with height.

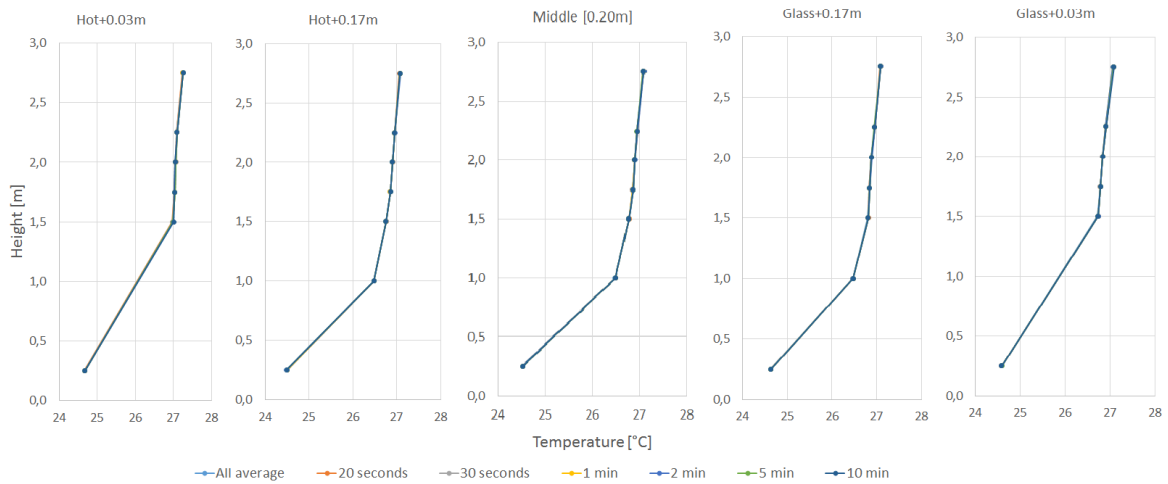


Figure 7.18. Temperature stability in the gap core (Case 1.1)

Concluding on the previous graphs it was visible that even though the plotted results include averaged values for different time period, the only visible result is a single line. This means that no fluctuations in temperatures are observed in that period. Based on the above graphs is proven that the average values from the chosen five minutes interval will represent accurately enough the temperatures inside the cavity.

Temperature contour plot

The next step is presenting the contour plot, which gives information about the entire temperature field inside the two dimensional measurement plane.

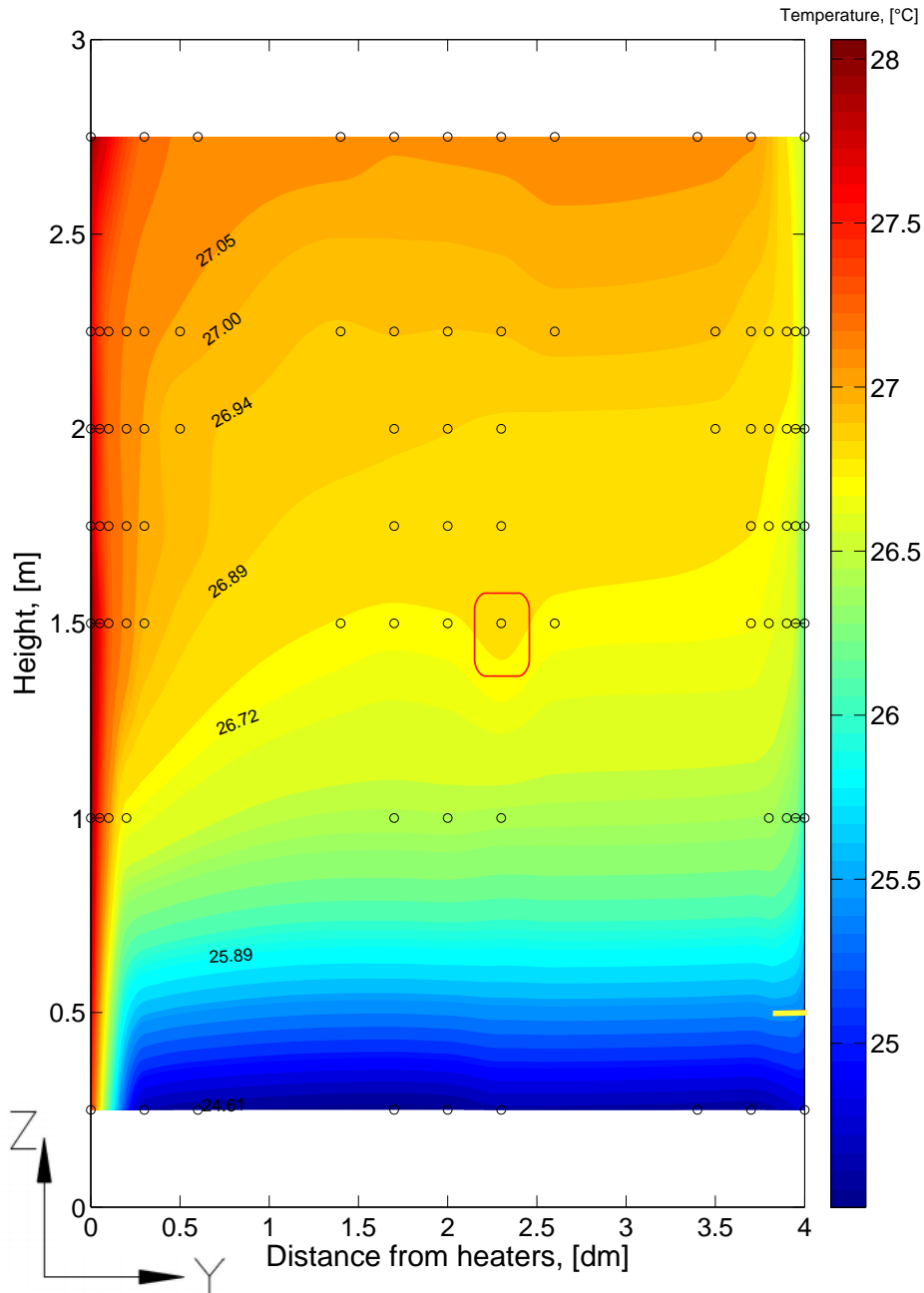


Figure 7.19. Contour plot of temperature (Case 1.1)

On that plot can be first noted the thermocouples positions marked with an empty circle. The interpolated data is between them in both vertical and horizontal direction. The color map on the right side is scaled according to the maximum and minimum temperatures. Above 1.5 meters the temperature differences in the core are very little as shown on figure

7.14.

Judging by the color scale difference in temperatures between the different color nuances is below the thermocouples precision. The reason behind that is that these small steps for each nuance are purely mathematical approximation, due to the interpolation procedure.

At height 1.5 meters and distance 23 cm from the hot surface, marked with red, can be seen an increase in the temperature in downward direction. This increase can be caused by an influence of the hot boundary layer or another phenomenon. Although, the formation of eddies at the edge of the boundary layer is considered highly unstable and dynamic, this might result in a slight increase in temperature inside the core.

On the other hand, the difference in the temperatures between this sensor and the neighboring sensors in horizontal direction is less than the precision of the thermocouples (0.087°C). This means that the increase can be attributed to sensor dislocation or calibration error. In support to this case is that only one sensor undergoes such an increase, which based on the nature of the flow would not be expected.

Regarding cases 1.1 to 1.4 the same occurrence was observed in each of them. Further experiments will be used to distinguish if this can be linked as experimental error or a physical process.

On figure 7.19 with yellow line is marked the level at which the temperature in the core of the cavity equalizes with the one at the cold surface. It is considered as important due to the fact that below it a formation of a thermal boundary layer in upward direction can be expected along the cold surface.

7.1.3 Velocity distribution

The velocity distribution inside the cavity is visualized on figure 7.20 using "quiver" command in MATLAB. It is chosen to show the data using two graphs - on the first is easier to distinguish the vector direction and general flow patterns and on the second one, using contour plot, are outlined the boundary layers and vectors magnitudes.

The results confirm the observed behavior at the videos. Along the hot and cold surfaces are formed two opposing velocity boundary layers. They are visualized better at the contour graph on the right. The limitation caused by the experimental setup is that measurements start at 6 cm away from the hot surface, which obstructs the proper estimation of the hot boundary layer. Still the velocities at the hot surface are twice higher than the ones at the cold one and way bigger than the ones at the first two levels, close to the inlet. This is a sign for a buoyancy dominant flow.

On the left plot is shown the calculated boundary layer according to equation 7.1. The curve shows agreement with the experimental data until approximately 2.25 meters. After that the boundary layer decreases its thickness in half. The maximal hot velocity boundary layer is assumed to be around 16 cm thick, while for the cold velocity boundary layer the maximal thickness is up to 6cm.

Additionally, when observing the velocity behavior in the levels above 2.25m in the core of the cavity, a strong variations in velocity direction and magnitude is noticed. The reason

for both processes can be from the disturbances when the powerful hot boundary layer hits the ceiling. This can result in increased turbulence in this region and mixing of the flow.

On the left part of figure 7.20 is drawn a red line in the lower half. This line represents the level at which is assumed that the cold boundary layer terminates and reverses its direction to become part of the core flow. It might be also said that at this level the core flow overpower the cold boundary layer. This observation is important when comparing between different experiments, because it gives information for the development of the recirculation in the cavity.

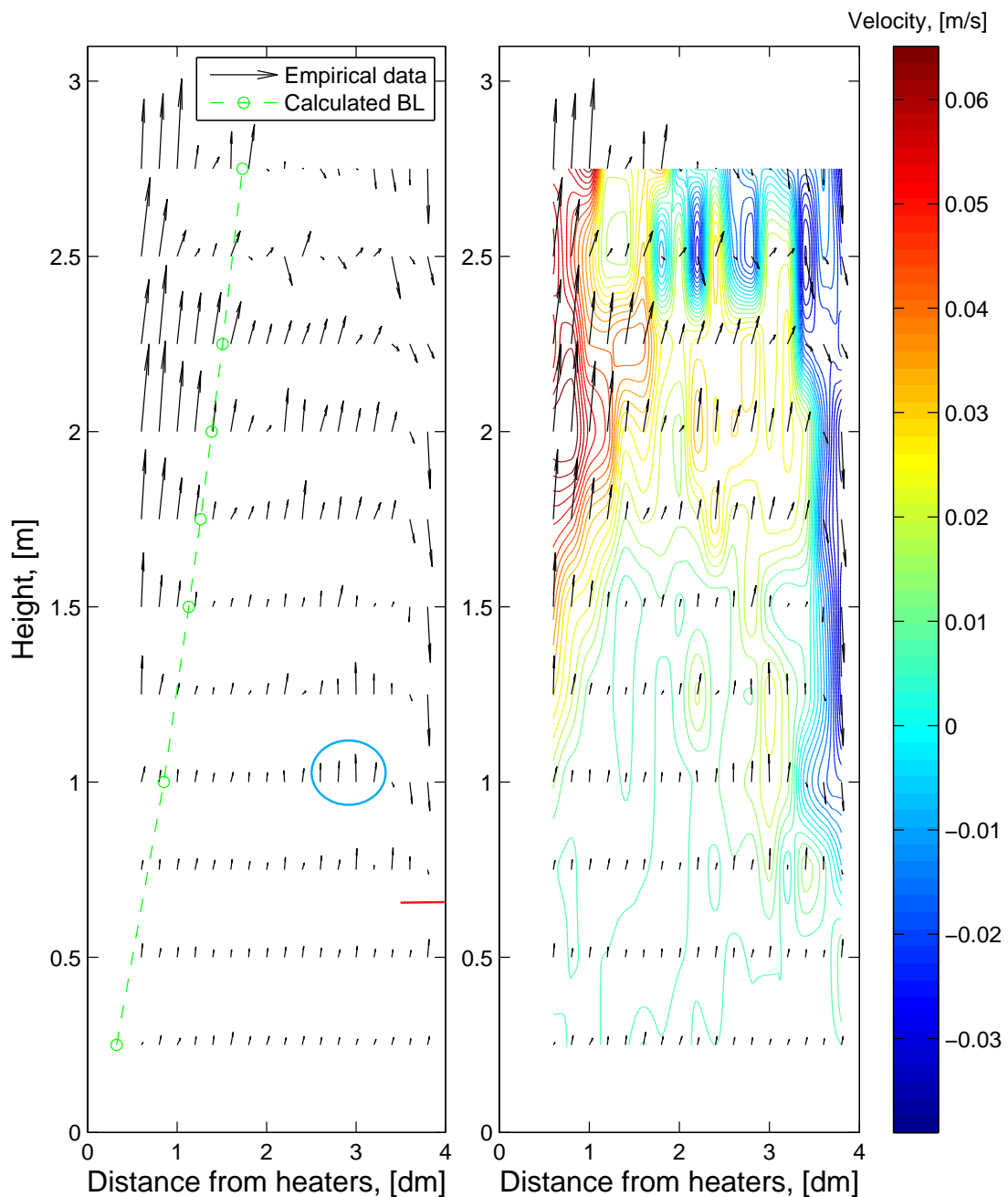


Figure 7.20. Comparison between analytical and empirical velocity boundary layers (Case 1.1)

When observing the development of the core flow on figure 7.20 is noticed a velocity increase above the cold boundary layer termination plane. It is marked with a blue oval on the figure. This pattern proceeds its rise on the following levels up to 1.75 meters height. From theoretical point of view, when two flows concatenate the resulting flow has an increased velocity. Therefore, this velocity rise should be a result of redirecting the cold boundary layer and its entrainment into the core flow.

Figure 7.20 does not give precise information about the velocity numerical values, therefore another way of data representation is necessary. On figure 7.21 is given the exact velocity magnitude of every combined velocity vector except the ones at level 0.25m. This level is avoided because of the similarities with level 0.50m.

The fluctuations at height of 2.50m vary from positive to negative with every consecutive measurement. The same pattern, but less intense is present on level 2.75m. This consolidates the existence of a physical phenomenon in this region

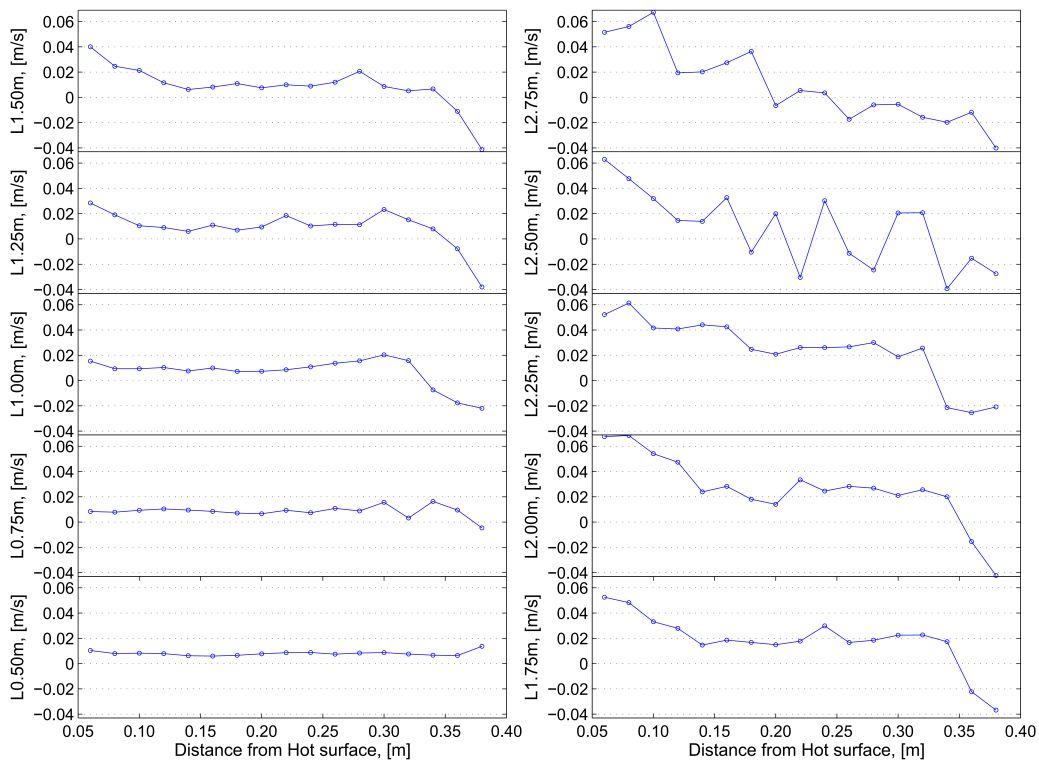


Figure 7.21. Velocity distribution on levels for Case 4

Since the conditions in the facade are considered as dynamic, it makes sense to compare the velocities for the different base experiments from Case 1.1 to 1.4. The purpose of this analysis is to observe the flow similarities inside the cavity when maintained as close as possible boundary conditions. Figure 7.22 presents the comparison between the cases. This data together with the baseline experiment boundary conditions (table 7.1) helps to evaluate properly the differences.

It should be highlighted that on figure 7.22 all experiments follow the same measurement

grid as presented before, except Case 1.3. In this case the focus is on the boundary layers and less in the middle of the cavity.

From the first look can be seen that even though the vector size is different between the cases, three regions with consistent direction can be distinguished. The first region is the one close to the inlet, which comprises heights 0.25m and 0.50m. The changes are so small that the vectors overlap and is difficult to see to which case they correspond.

The second region with similarities is along the hot surface boundary layer. The vectors have same direction up to level 2.25m although their magnitude is varying. The maximal thickness of the boundary layer in all cases reaches 1.6 dm inside the cavity. However, above 2.25m the velocities start to fluctuate and the boundary layer thickness is decreased in all cases. The average integral temperature of the heaters is the lowest in Case 1.1, which explains why at level 1.00m the boundary layer is still not visible in the measuring zone. Here should be stated that in cases 1.3 and 1.4 the On/Off controller causes fluctuations in heating mats temperature. This might be the reason why on level 2.25m only in PID cases the boundary layer is developed, while in On/Off case it contracts. The explained above region is marked with a black oval on figure 7.22.

The third region with partly consistent pattern between the cases is the cold boundary layer. In all cases there is a downwards flow close to the cold surface, although the magnitude and direction of the velocity vectors are varying. Furthermore, in all cases the plane at which the cold boundary layer terminates is between 0.75m and 0.50m. This gives a confirmation that the phenomenon of recirculation has a consistent manner of appearance. Even though the laboratory temperature for the different cases is varying with roughly 2°C the phenomenon still preserves the pattern.

On the other hand, there is a highly unstable zone in the core of the cavity at heights 2.50m and above (black rectangular on figure 7.22) and at the edges of the velocity boundary layers. In these zones the direction and magnitude of the velocity can rapidly change. This might be caused by a mixing flow with a turbulent manner.

As mentioned above there is an increase of velocity in the region close to the cold boundary layer termination plane (blue oval on figure 7.20). The same pattern is present in all cases, which confirms the assumption for concatenation of the cold boundary layer and uniform inlet flow.

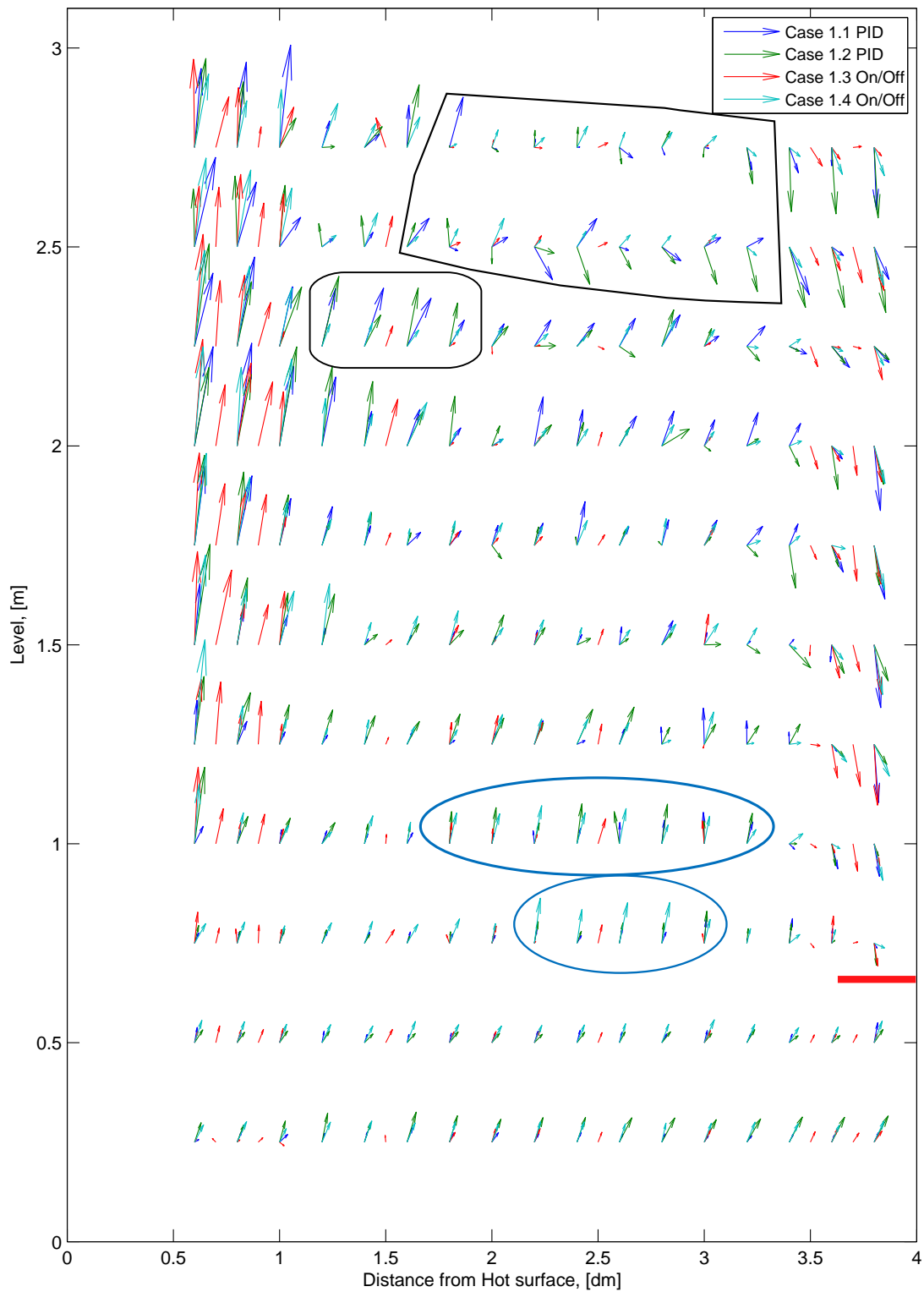


Figure 7.22. Baseline cases comparison

To sum up, the existence of repetitive vector direction in all cases is a sign for a reliable results and a proof that in these boundary conditions a recirculating flow appears.

Simultaneously, the presence of results with varying direction and magnitude, contribute to the theory that highly dynamic and uncertain flow is dominating inside the cavity core.

A different perspective to the analysis of the velocity dynamic is made by performing an experiment with the same boundary conditions as in Case 1.4, but with restricted number of collected samples. This is presented on figure 7.23 . In a full experiment 15 000 samples are acquired for every measuring point, however to show the dynamics of the flow is used a reduced number of samples (5000 samples). Normally LDA systems are used to measure in a stable velocity flows, but the current case has dynamic conditions. This makes the measuring time too large to account for the instantaneous change of velocities. By decreasing the number of samples, the acquisition time reduces with 1/3. The disadvantage of this analysis is that the measurement precision decreases with reduction of the acquired samples. Additionally, the measurements are performed every 1cm in the regions at the edge and inside of the boundary layers. Intermediate levels are added to focus on the zones. The target is the upper part of the hot boundary layer and the lower part of the cold one. As a result is expected to observe an instability due to eddies formation.

Observing the upper part of the hot boundary layer on figure 7.23 shows an agreement between the full case and 5000 samples. Both magnitude and direction are significantly similar. However, if we focus on the horizontal velocity distribution of the pink vectors can be observed a region in which the vectors tilt from vertical to horizontal direction. This shows that there exists a flow fluctuation with unpredictable manner. In general that can be assumed to explain the existence of eddies. On the other hand, since the experiments do not include simultaneous acquiring of velocity for all measuring points, there is no exact confirmation for eddy formation.

In the lower part of figure 7.23 the target was to observe closely the termination of the cold boundary layer. The vectors are consistent between the cases and the termination plane is estimated between levels 0.625m and 0.750m. Additionally, when we examine the overall picture of the red vectors a global process of rotation is noted. A proof for that is the inclination to the left of the vectors at levels 0.625m to 0.875m and to the right for the levels above. It looks like the cold boundary layer reverses its direction and is entrained into the core of the cavity.

A close look to the edge of the cold boundary layer shows an appearance of horizontal vectors at almost all levels in that region. A healthy development of the boundary layer includes entrainment of external air, which ensures that it will grow properly. Therefore, those vectors are sign for feeding of the cold boundary layer. However, it is exposed to an opposing flow, which restricts that development to some extent.

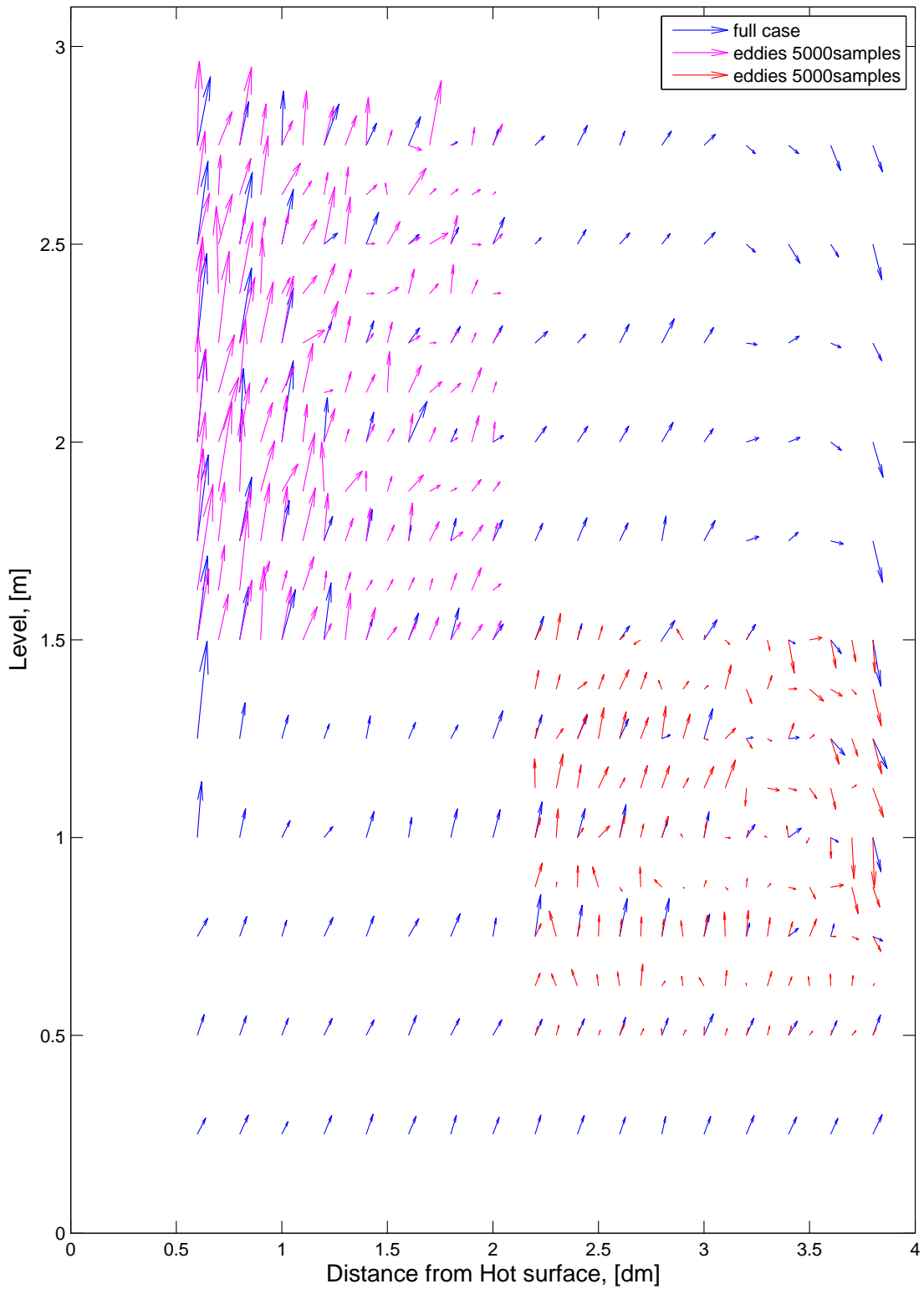


Figure 7.23. Close look at boundary layers for Case 1.4 with 15 000 samples and 5000 samples

During the process of acquisition it was noted that in some zones inside the cavity the

average velocity for a given point varies between positive and negative. On figure 7.24 are shown results based on Case 1.1 where the whole data set is split on sets representing 1000, 5000 and 10 000 samples and their average velocity is plotted.

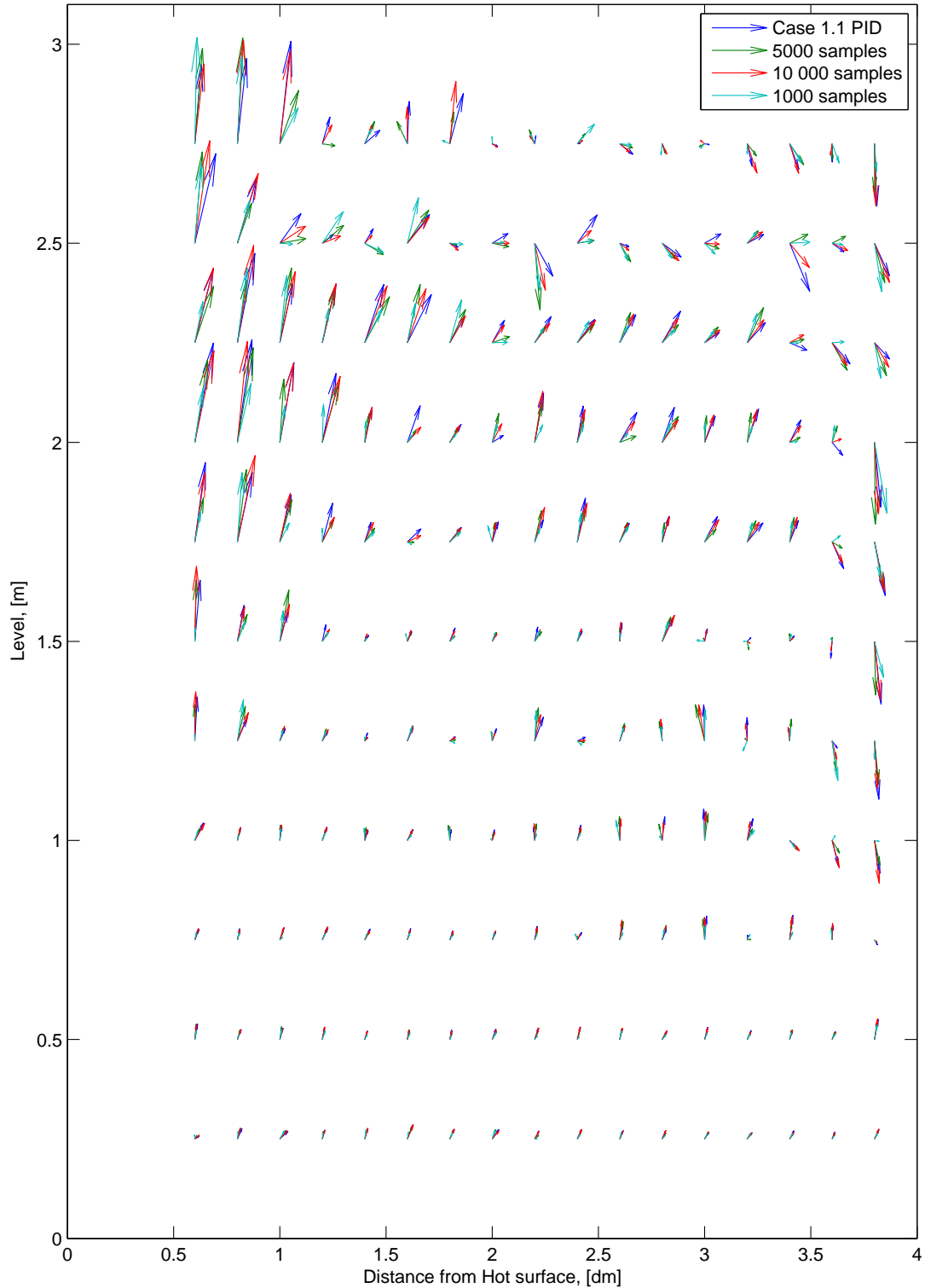


Figure 7.24. Stability of the acquired data for Case 1.1

By doing this analysis it is possible to understand how stable the acquired data is. The interesting zones are the one which have a deviation from the averaged values based on the full case with 15 000 samples. The first few levels show a complete agreement between the different sample groups. This leads to assumption for stable supply with negligibly small fluctuations. Focusing on the hot boundary layer the consistence is noticed up to 2.25m. Above this level, in the zone of decreasing boundary layer thickness, the fluctuation is significant. The velocity varies from positive to negative not only close to the heated surface, but on the entire length of levels 2.50m and 2.75m. This region presents unstable flow pattern in all cases observed above. Clearly the flow is consistently exposed to conditions, which lead to mixing and turbulence in that zone.

A fluctuation is noticed close to the upper part of the cold boundary layer. A reason for that can be an entrainment of the mixed flow into the cold boundary layer.

To sum up the flow supply inside the cavity is assumed as stable. Any fluctuation existence is caused by natural means and cannot be a consequence from the inlet air. Additionally, the instability is concentrated close to the outlet of the cavity, which might be a result from a flow collision with the cavity ceiling or influence from the exhaust opening. The results observed by analyzing the split data set can be used to justify fluctuations only in the measurement time interval for each point.

In order to present the fluctuating velocity regions in a better way a velocity contour graph is plotted on figure 7.25 . The figure presents fluctuating velocities at the same locations as in figure 7.24 . The fluctuations are given as a time dependent variable in this case, where the value is calculated based on figure 7.7. This contour plot cannot show the change in direction of the vectors, but it clearly highlights the zones with highest velocity magnitude variation.

Fluctuations are visible at the boundary layers along heated and cold surfaces. Even though the direction of the vectors in those zones is more or less the same, the velocity magnitude is quite different. In the lower part of the cavity the fluctuations in velocity are very close to zero. This kind of reaction is expected, due to the uniform flow supplied through the inlet. Another point of view is that the uniform flow is rising high in the core flow, where it is consequently entrained in the mixing region.

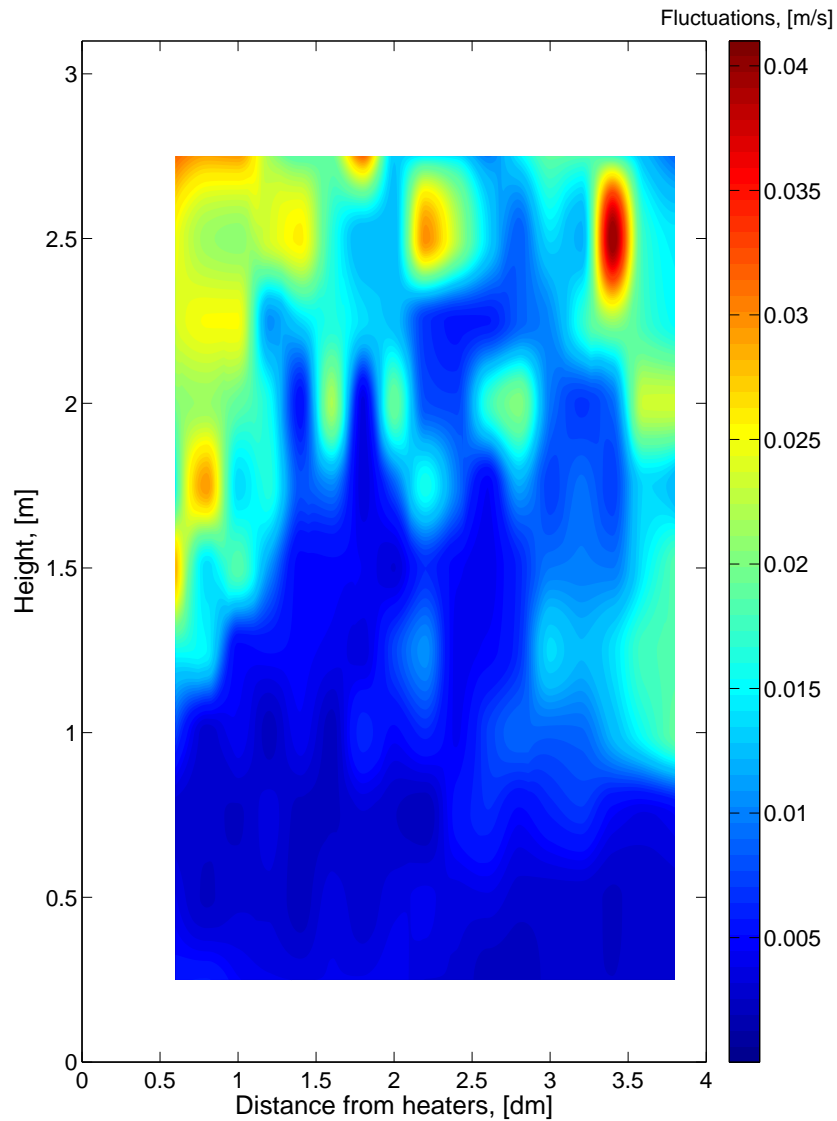


Figure 7.25. Velocity fluctuations for Case 1.1

The last velocity analysis is regarding the standard deviation for each point in horizontal and vertical direction, and is used to obtain knowledge about the turbulence level inside the cavity. The results calculated based on formula 7.3 are visualized on figure 7.26 as a square root of the kinetic energy.

The whole interval of turbulence fluctuations is between 0.0484 m/s and 0.0690 m/s. The first observation is regarding the inlet influence on the flow. At the first two levels is noticed the highest turbulence in the entire cavity. A reason for that might be the inlet construction and more specific - the inlet opening grill. However, even though this is the region with higher standard deviation the acquired average velocities are stable.

In the upper part of the cavity at levels 2.50m and 2.75m is visible a region with increased turbulence. At this place the velocity vectors also show inconsistency and conditions for turbulence.

As an overall result the range of deviation of the turbulence inside the cavity is very small. There are no regions where the turbulence is close to zero (non-turbulent), therefore should be concluded that the cavity flow is turbulent. However, this statement will be confirmed or denied by the dimensionless analysis.

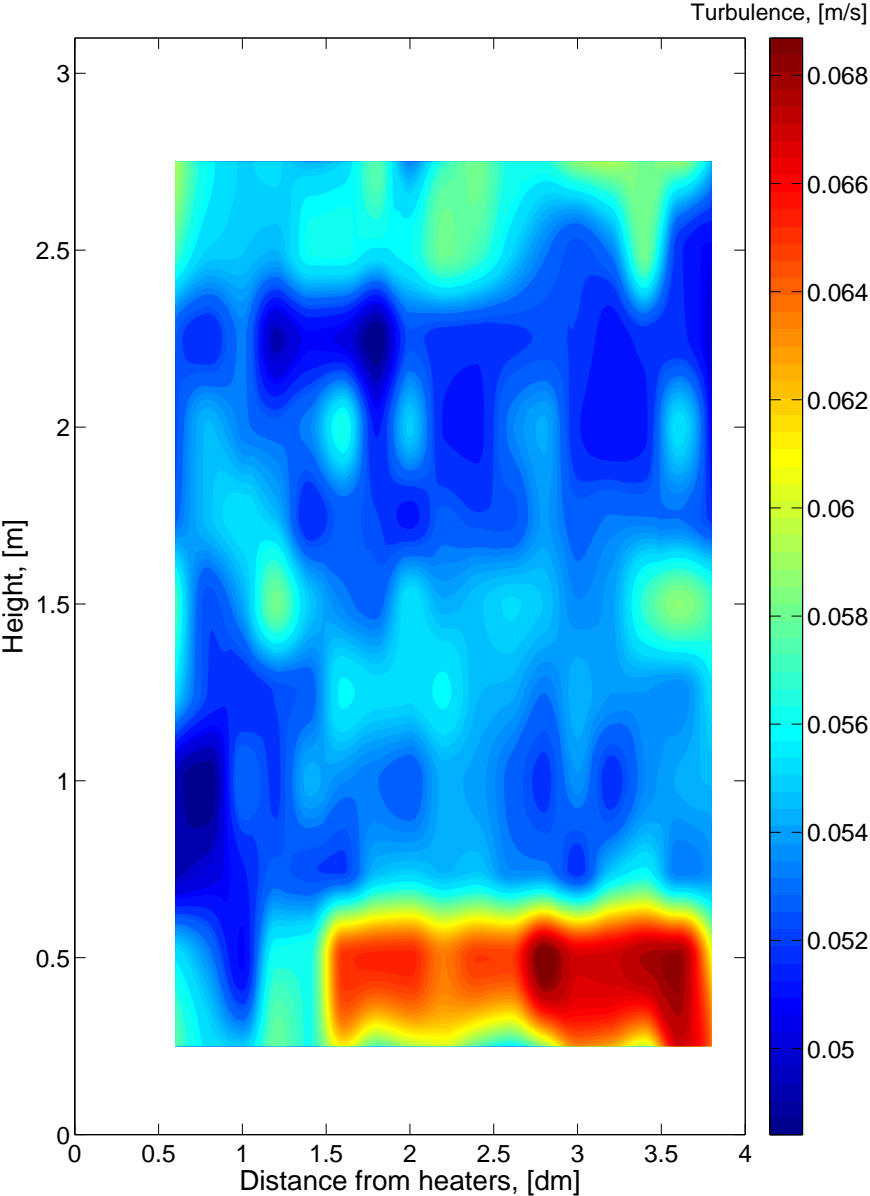


Figure 7.26. Turbulence in Case 1.1

7.1.4 Dimensionless analysis

This analysis will provide understanding for the processes inside the cavity and a possibility for comparison between other experiments with similar targets. All dimensionless

numbers, including characteristic dimension are calculated according to height of the cavity.

Table 7.2. Dimensionless number for Baseline experiment

	Case 1.1		Case 1.2		Case 1.3		Case 1.4	
	Hot	Cold	Hot	Cold	Hot	Cold	Hot	Cold
Gr_H	4.86E+10	4.11E+10	4.84E+10	4.15E+10	4.92E+10	3.92E+10	5.04E+10	3.96E+10
Pr	0.7026	0.7028	0.7026	0.7028	0.7026	0.7028	0.7026	0.7028
Gr_H/Re_H^2	1.07E+05	9.07E+04	1.05E+05	9.04E+04	1.07E+05	8.55E+04	1.10E+05	8.63E+04
Ra_H	3.41E+10	2.88E+10	3.40E+10	2.92E+10	3.46E+10	2.75E+10	3.54E+10	2.78E+10
Re_H	673		678		677		677	
Velocity cross section, [m/s]	0.0034							

In section 2.3 is explained the physical meaning of all dimensionless numbers, so based on that from observation of the Grashof number in table 7.2 can be clearly stated that the buoyancy forces are overcoming the viscous forces in all cases. Therefore, the flow inside the cavity is characterized as a buoyancy driven flow.

Regarding the Prandtl number the calculated value is less than 1, therefore can be concluded that the thermal diffusivity is dominating the momentum diffusivity. This means that the ability to conduct thermal energy is increased over the ability to store it. Since Prandtl number includes only thermal properties of the fluid, there are no changes between the cases.

The Rayleigh number is used to characterize the flow regime inside the cavity. In chapter 5 is given the critical Rayleigh number above which the flow regime is defined as turbulent. All performed calculations state a value above $Ra \approx 10^9$, therefore the flow is considered as turbulent.

Reynolds number combined with Grashof number forms a relation, which specifies the convection flow regime. The values for Gr_H/Re_H^2 in table 7.2 are much higher than 1. This is enough to define the convection regime as free.

To sum up the flow inside the cavity is turbulent free convection. This assumption agrees with the flow dynamic observed through experiments and complies with the desired initially conditions.

7.2 Comparison group one - air-change rate variation

The experiments conducted in this part aim to distinguish the physical phenomena and their variations with increase of the supply air-flow inside the cavity. The chosen steps start from the lowest achievable supply flow-rate and finish with four times bigger. The averaged empirical temperatures and volumetric flow rates are shown in table 7.3.

The same method as explained before was used for presenting the different cases. Looking into the experimental boundary conditions is visible that for exp. 2 (ACH 3), the temperature at the inlet opening is marginally higher than the rest of the cases. This is due to the combination of lower supply flow-rate and the overheating by the fog generator smoke production. These two effects restrict the proper maintenance of the

inlet temperature. In this case the cooling equipment was working at full power, and the result is appreciated despite the slight difference. As mentioned in the previous case the laboratory temperature cannot be controlled, but in these four experiments it is not varying significantly.

Table 7.3. Experimental boundary conditions for Group 1

Exp. №	ACH, [-]	$T_{heaters}$, [°C]	T_{glass} , [°C]	$T_{gapcenter}$, [°C]	T_{inlet} , [°C]	$T_{laboratory}$, [°C]	\dot{V} , [m^3/h]
1	4	27.91	26.02	26.48	15.77	23.72	5.68
2	3	27.96	26.12	26.60	16.41	23.56	4.28
3	8	27.94	25.89	26.08	16.06	23.60	11.35
4	12	27.87	25.83	25.59	15.89	23.87	16.99

7.2.1 Temperature distribution

Analysis of the temperatures is done over contour plots and line graphs for the chosen experimental cases. On figure 7.27 on the facing page are summarized all temperature contour plots for experiments from group one (Table 7.3).

Observing the temperature contour plots, on the right side of figure 7.27, can be seen that the scale for all experiments is the same. This gives the opportunity to compare the influence of the ACH variation on the temperatures inside the cavity. The first thing that draws attentions is that with an increase of airflow, the cold air penetration height rises. This is accompanied with slower development of the hot surface boundary layer and decrease of temperature in the core. At heights above 1.5m the temperature in the core for Exp. 4 (ACH 12) is around 0.5°C lower than in Exp. 2 (ACH 3). This decrease in temperature is insignificant compared to the difference between the cases at the inlet region (around 4.5°C).

With the lowest ACH of 3 the temperatures above 1.50 meters are nearly uniform, and very close to the hot surface temperature, which means that the area can be assumed as well mixed. Based on the isotherm at height of 2.25 meters can be observed how the higher temperature region close to the cold surface spreads a bit lower than at the core of the cavity (marked with black square at figure 7.27 Exp. 2). The same profile can be seen in all four cases, but with different proportions. The reason for this temperature profile might be related to the hot boundary layer flow transition toward the cold surface.

As before at height of 1.5 meters an increase of temperature is visible, at 23 cm away from the hot surface. This result is generally visible in all cases, which following the discussion from the baseline experiment addresses the issue as a sensor problem or dislocation, rather than a physical phenomenon. Based on that conclusion, this temperature variation between 1.5 meters and 1.00 meter will not be regarded anymore as relevant to the temperature field.

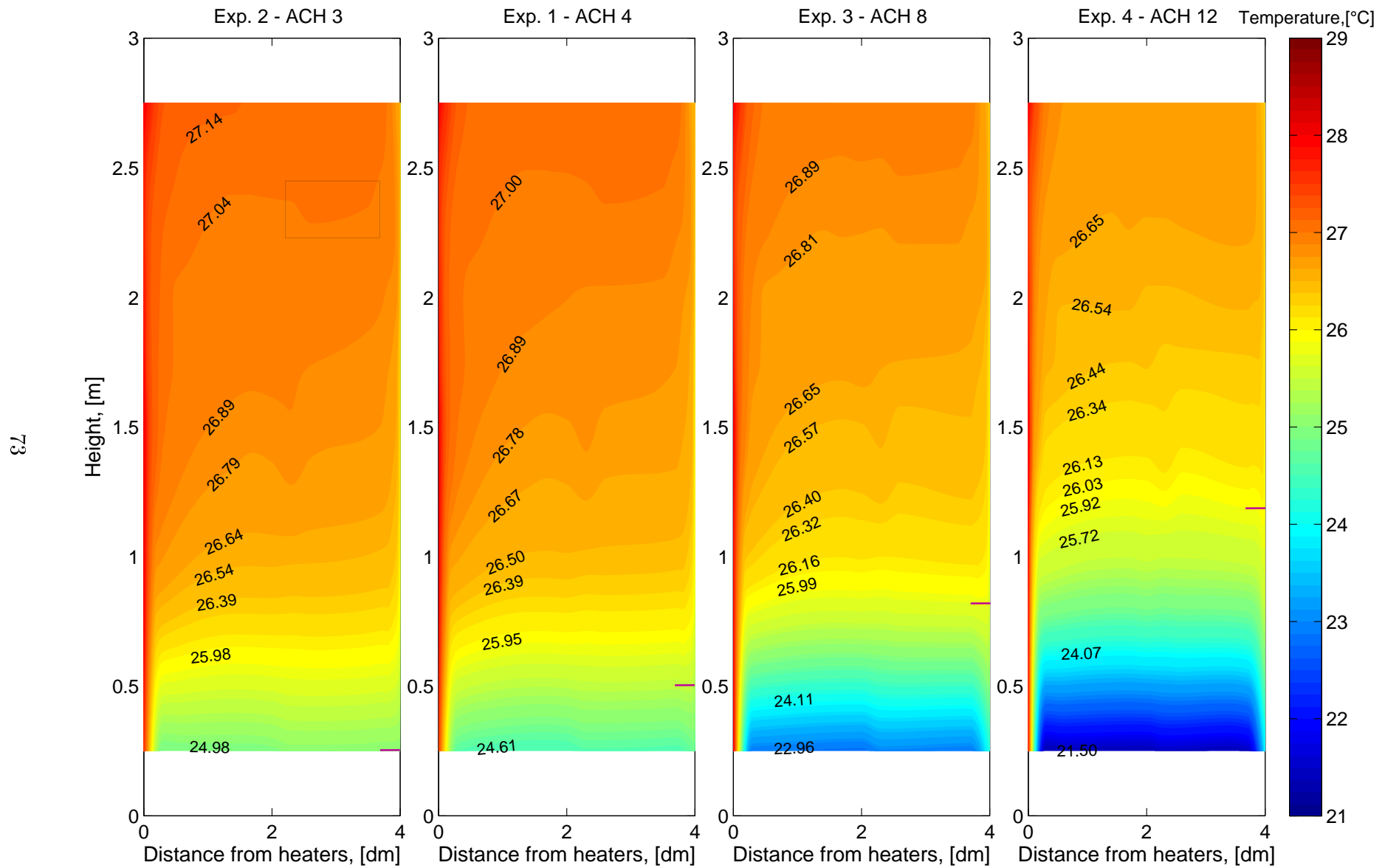


Figure 7.27. Temperature comparison with ACH variation (Group 1)

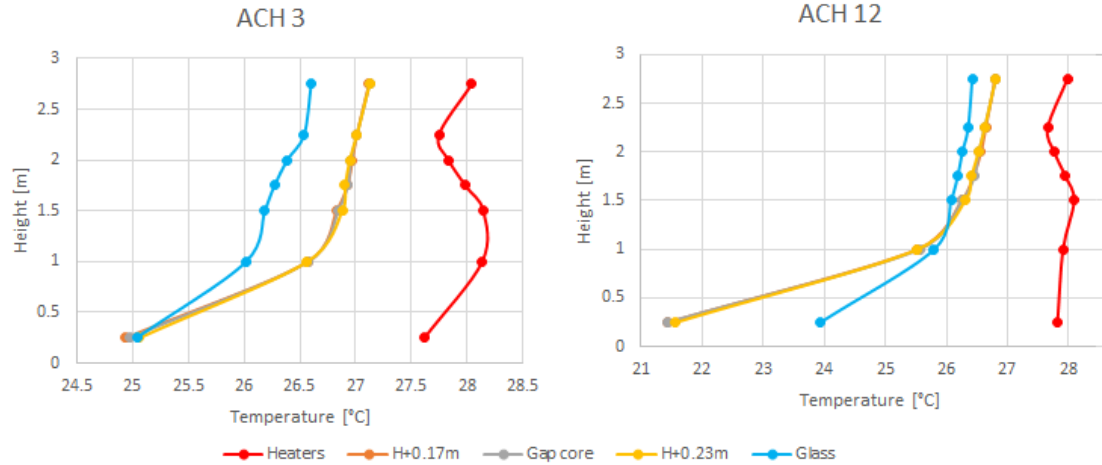


Figure 7.28. Vertical temperatures in case 2 and 4 (ACH3 and ACH12)

Figure 7.28 shows the difference between the core and surface temperatures for both extreme cases. For the lowest air-change rate the core temperature at 0.25 m height is close to the glass surface temperature, meaning that the supplied air is overheated from 16 to 25°C before reaching that height. For the other extreme case the core temperature and glass temperatures equalize at height of approximately 1.25 meters. This implies that for the second case both surfaces act as hot, compared to the fluid temperature at the core, until height of 1.25 meters. The vertical temperature distribution graph for Exp.3 can be seen in appendix D.1 on page 134.

The point at which temperatures at the core and the glass surface equalize are marked with purple line (right side of each graph) on figure 7.27 on the preceding page. The trend of raising of this plane with increase of ACH is clearly stated. Following that observation, can be assumed that until the respective cross plane (for each case), is possible development of thermal boundary layer in upward direction along the glass surface.

7.2.2 Velocity distribution

On figure 7.29, are presented the velocity vector plots for the same four cases. The resultant vectors are scaled with regards to the highest vector magnitudes of all four experiments. In this way easier comparison between the cases is possible.

It could be judged for boundary layers development based on the higher velocities at the vicinity of the hot and cold surfaces. Nevertheless, the results show stronger development of the hot boundary layer in the measurement zone for all four cases. Their thickness is decreasing with increase of the air-change rate. The analytical method for determining the velocity boundary layer thickness copes well with the first two cases, but over-predicts the thickness with increased ACH. This is due to the simplicity of the calculation method and the fact that it is based on surface and bulk temperatures, therefore not taking into account velocities.

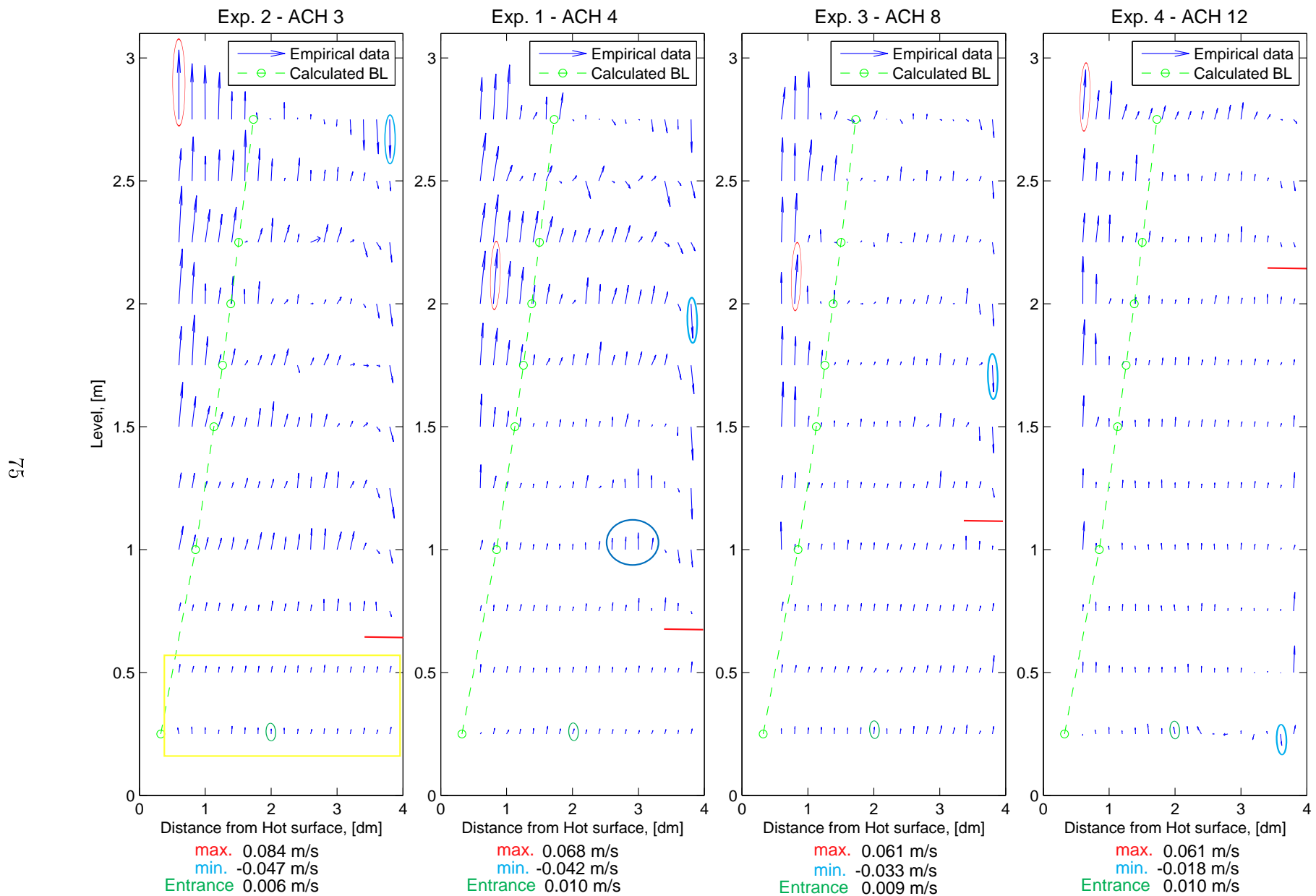


Figure 7.29. Velocity comparison with ACH variation (Group 1)

At the bottom of each plot are extracted some key values of the velocity vectors. The vectors are marked according to the color legend. At the entrance region is visible that the velocity vectors are similar in magnitude despite the change of the inlet velocity. In all cases the maximum velocity was measured inside the hot boundary layer. The position of the vectors having maximum values however varies. The highest of all velocities was encountered at the case with lowest air-change rate. The reason behind, is that with the ACH of 3 the least amount of air is driven by the fan inside the cavity, leaving the buoyancy forces much stronger than the forced airflow. In that way closer conditions to free convection are achieved. When increasing the ACH, buoyancy is suppressed, therefore boundary layers thickness is reduced. This however abates from the desired free convection flow conditions.

At the cold surface can be observed similar trend, where with lowest ACH the boundary layer shows healthy development, based on the horizontal vectors serving to feed it, while the increase of ACH almost destroys it. With red marker for each plot, is shown the plane at which the cold surface velocity boundary layer is terminated. Again with increasing ACH the termination plane raises along the glass surface.

The approximated as uniform flow zone is squared with yellow on figure 7.29 on the previous page for the first experiment (ACH 3). The assumption is that this zone is increasing with the ACH increase. It constitutes mainly of similar in magnitude and direction vectors, which proves the steadiness of the flow inside. After observing this zone in all four cases, can be seen a directly proportional relation between the termination plane (red mark) and the uniform flow (yellow square).

In the ACH 12 case the uniform region is significantly larger as seen in the velocity vector plot. It is better visualized on figure 7.32 on page 79. Even though the velocities in the cavity's core can be generally considered uniform at heights up to two meters (excluding the hot BL), at the cold surface a velocity boundary layer is formed in ascending direction. This is assumed as a reason for the termination of the descending cold surface boundary layer. In this region from 0.25 to 2.00 meters, the flow resembles standard channel flow, which deviates from the rest of the experimental cases, and the aim of the project.

The region marked with blue oval in the baseline experiment is shown on figure 7.29 as well. It is visible that velocities are higher in this part of the cavity. It is assumed that this is formed by the collision of the ascending and descending cold surface boundary layers. The region is varying in shape and dimensions, but in all cases can be seen its presence.

Figure 7.30 quantifies the velocity vectors for experiment 2 (ACH 3) at each level of measurements. The rest of the cases can be found in appendix D.6 and D.5 on page 136.

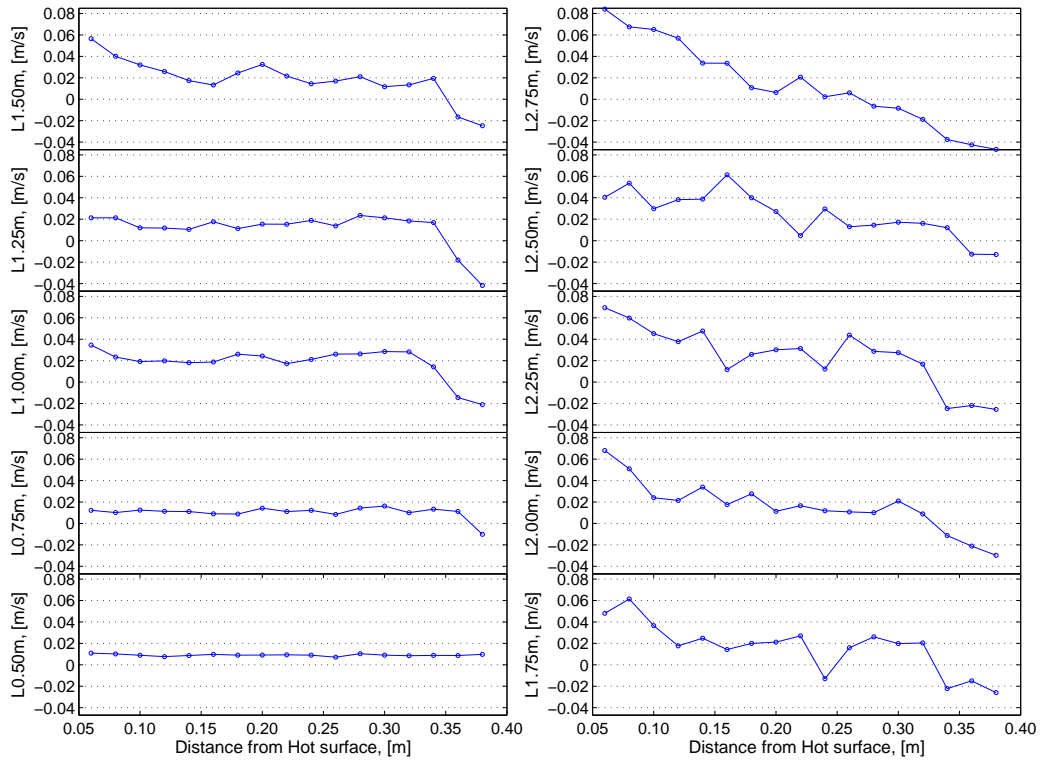


Figure 7.30. Magnitude of velocity vectors for Exp. 2 (ACH 3)

The trend of skewing of the velocity profiles with increase of height can be seen at figure 7.30. It is caused by the boundary layers development. At the first levels a deception that stronger cold surface boundary layer is developed is caused by the lack of measurements in the first 6 cm at the hot surface. This prevents further analysis of the cross section mass balance. The lowest level velocities at 0.25 meters for this case are not presented on the figure, because they coincide with the results at 0.5 meters height.

However, at the last experiment (ACH 12) on figure 7.31, is visible that at the bottom of the cavity are not observed uniform, but rather variable flow velocities. It is linked to the higher air-change rate and the inlet opening grill, which creates an entrance mixing region close to the inlet opening.

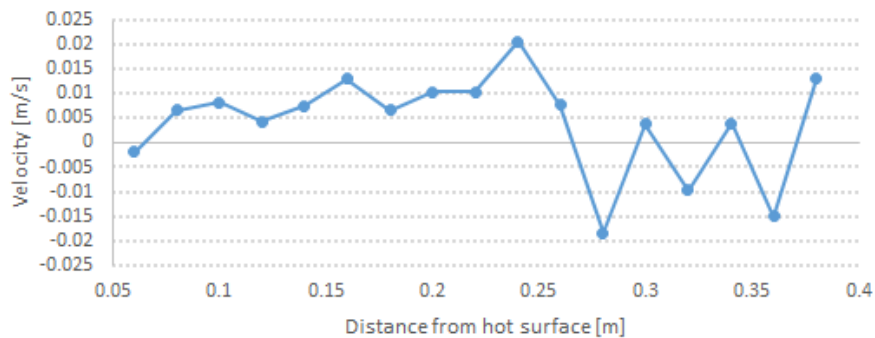


Figure 7.31. Velocity distribution exp. 4 (ACH12) level 0.25 m

Further on figure 7.32 on the facing page additional information can be found at the plotted velocity contours for the same experimental cases. This helps distinguish visually the boundary layers discussed above. The velocity contour scale is again consistent for the four plots.

The experimental results confirm the employed theory, for the existence of two separate developing boundary layers at each surface. The two opposing boundary layers can be seen for each of the experiments, but only in the baseline case can be noticed unusual behavior in the top part of the facade. This as mentioned earlier might be caused by mixing process due to the ceiling's influence or the exhaust opening. However, the full recirculation as the one shown on figure 5.2 on page 32 cannot be clearly observed in the experimental results, since there is no evident connection between the cold and hot surface boundary layers at the bottom of the cavity. The reason for this is assumed to be the fan supplied flow.

Visually the boundary layers thinner and move upwards with increase of air-change rate. The cold boundary layer termination plane is located at 0.55m height for Exp. 2 (ACH3), while by increasing the ACH four times this plane rises to approximately 2.15m (red mark on fig. 7.29). It is assumed that based on this termination plane can be judged about the limits at which recirculation occurs. By increasing the ACH above 12 the downward cold surface boundary layer will be destroyed and standard channel flow will be created. On the other hand, by decreasing the ACH bellow 3 the two boundary layers might be expected to connect as on figure 5.2. Another fact is that the boundary layers are not consistent in thickness and magnitude along the height. If we draw attention again to exp. 2 (ACH3) on figure 7.32 at height of 2.5 meters the increase of the hot surface boundary layer thickness can be related to the decrease of the opposing boundary layer thickness.

On figure 7.32 is shown the spreading of the uniform flow into the cavity core. The velocities in this flow are very close to zero based on the color map. Nevertheless they negate the cold boundary layer, while simultaneously decreasing the hot. Unfortunately the before mentioned blue oval region at the height of the cold boundary layer termination plane cannot be clearly seen on these plots.

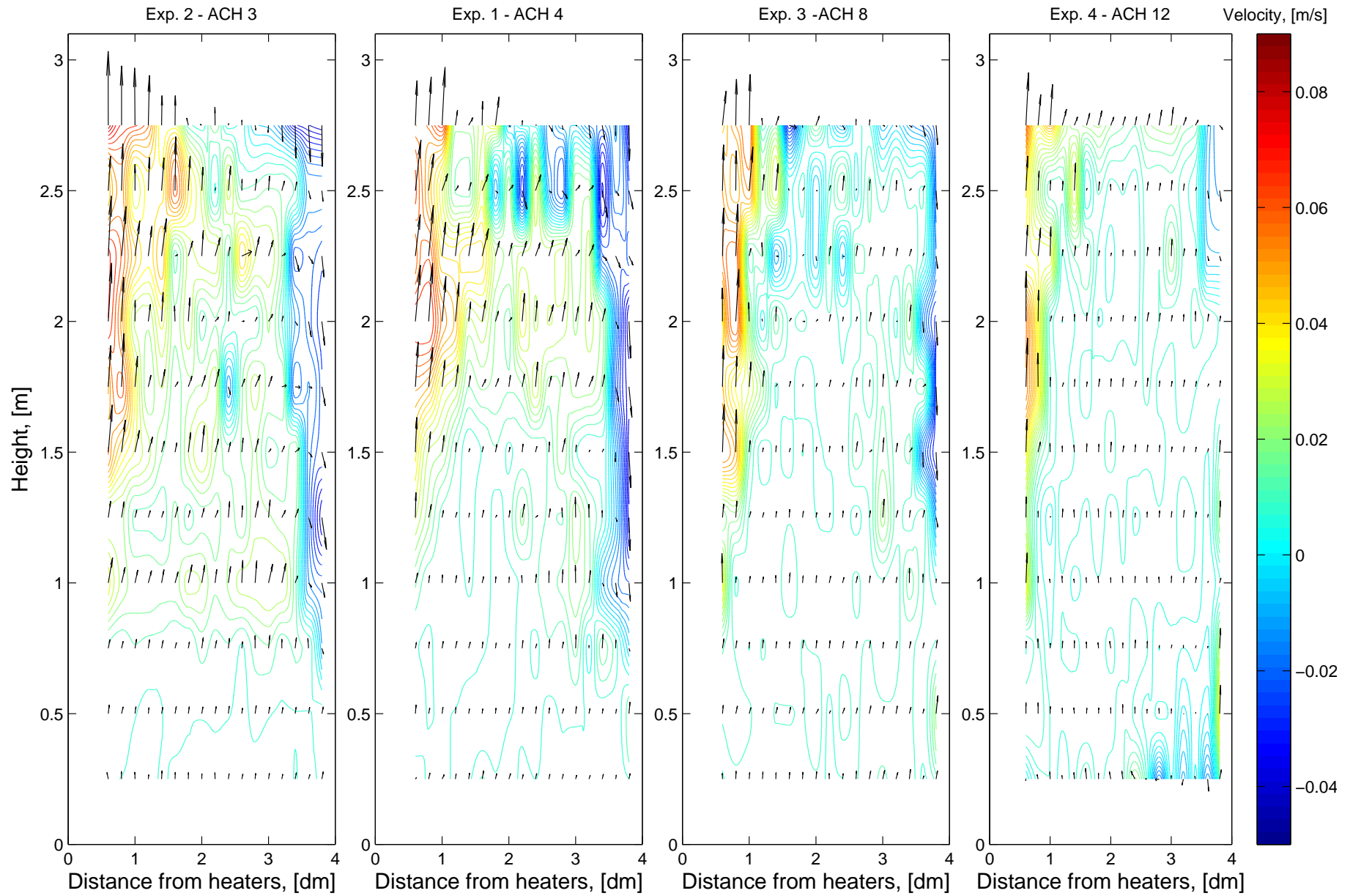


Figure 7.32. Velocity contour plots comparison with ACH variation, (Group 1)

Further on figure 7.35, can be made analysis of the flow stability with time. The different samples sets, correspond to different data acquisition time intervals. Therefore the flow dynamics can be estimated based on the already obtained results. The vectors denoted with "Full case" correspond to the average value from the total 15 000 samples collected for each point. An important note is that these plots are not scaled uniformly, meaning each of the experimental cases has its own scale. This is caused by the inability to show all of the necessary information for the vectors stability when scaling them uniformly. Therefore a comparison between the experiments is not possible.

The general observation is that consistent results in both magnitude and direction are visible at the bottom of the cavity and partly in the boundary layers. However at the edge of the boundary layers and in the unstable region at the upper part of the cavity a discrepancy between the averaged values is visible. Regarding ACH 3 experiment, inconsistent results can be noticed at several locations on figure 7.35. The majority of the unstable results are situated in the vicinity of the cold surface boundary layer. The difference can change from slight variation in the vector angle to complete switch of the flow direction. This implies that the flow in this region is unpredictably fluctuating throughout the measurement period of time.

An interesting observation is that in Exp. 1 (fig. 7.35) at height of 2.5 meters strong discrepancy in the results is visible. Comparing it to the next experiment can be seen that with the increased ACH similar results are shown at 2.75 meters, meaning that the mixing region is moved further upward. In these cases exist as well instabilities in the vectors magnitude and direction. Except in the before mentioned region in the upper part of the cavity these are available mostly at the edges and partly inside the boundary layers. With increase of the ACH the appearance of such vectors decreases due to the weaker boundary layers development.

Drawing the attention to specific locations, the circled vectors in Exp. 2 on figure 7.35, show two examples of a divergent and convergent velocity vectors. On figure 7.33 are presented the velocities in relation to the acquisition time for these two locations. The lines represent the averaged velocity measurements based on the full dataset. The moving average principle based on a subset of 500 samples, (explained in chapter 7) is used for the better visualization.

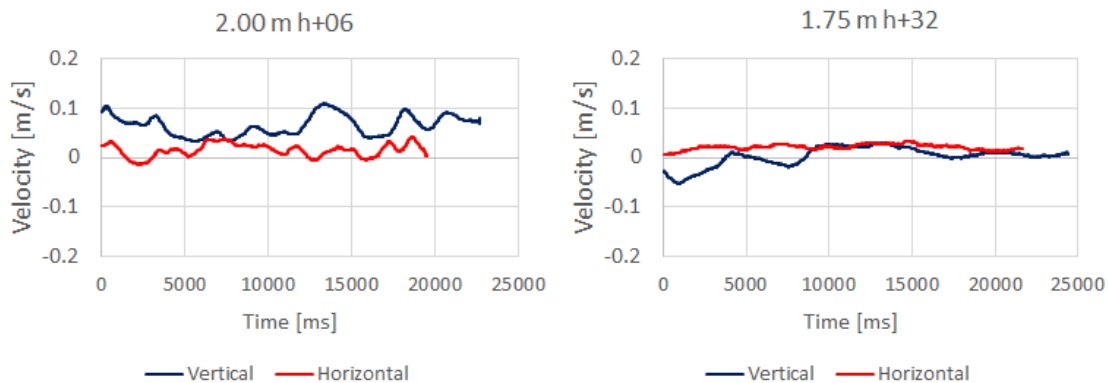


Figure 7.33. Moving average velocity for Exp. 2 (ACH 3)

It is visible that at two meters (left) in the hot boundary layer there is an instability of the vertical velocity. Nevertheless the result is always in the positive range. Simultaneously, due to the higher vertical velocity, the variation of the horizontal does not affect the resultant vector since it is too small.

On the other hand, at height 1.75 (fig.7.33) is visible that during the first 10 seconds approximately, the vertical velocity was negative. After this for the rest of the measurement time the horizontal and vertical velocities are almost the same.

The same analysis for two selected positions in Exp. 4 is done. The idea is to show that the velocity is not constant even at places where it looks stable. Figure 7.34 shows these results.

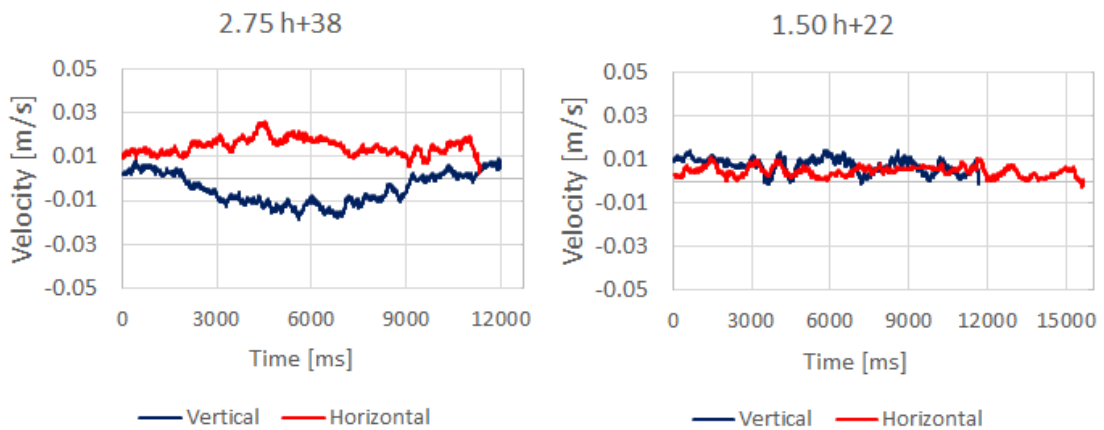


Figure 7.34. Moving average velocity Exp. 4 (ACH 12)

The first observation is that the general time for acquisition in this case is almost twice shorter than at fig. 7.33. In addition the velocities are much smaller, which could be the reason for the shorter measurement period. Another fact is that the smoothness of the curves is not the same even though the moving average analysis uses the same subset intervals (500 samples). This is due to the smaller velocity scale on figure 7.34.

At the height of 2.75 meters was observed that both horizontal and vertical velocities are deviating in different directions. Only the vertical velocity however goes from positive to negative at that point. At height of 1.50 meters smaller variation is visible, which is as well reflected on the vector plots. In this case the vertical velocity does not switch to negative, which is a confirmation of the stability of the flow direction in this region.

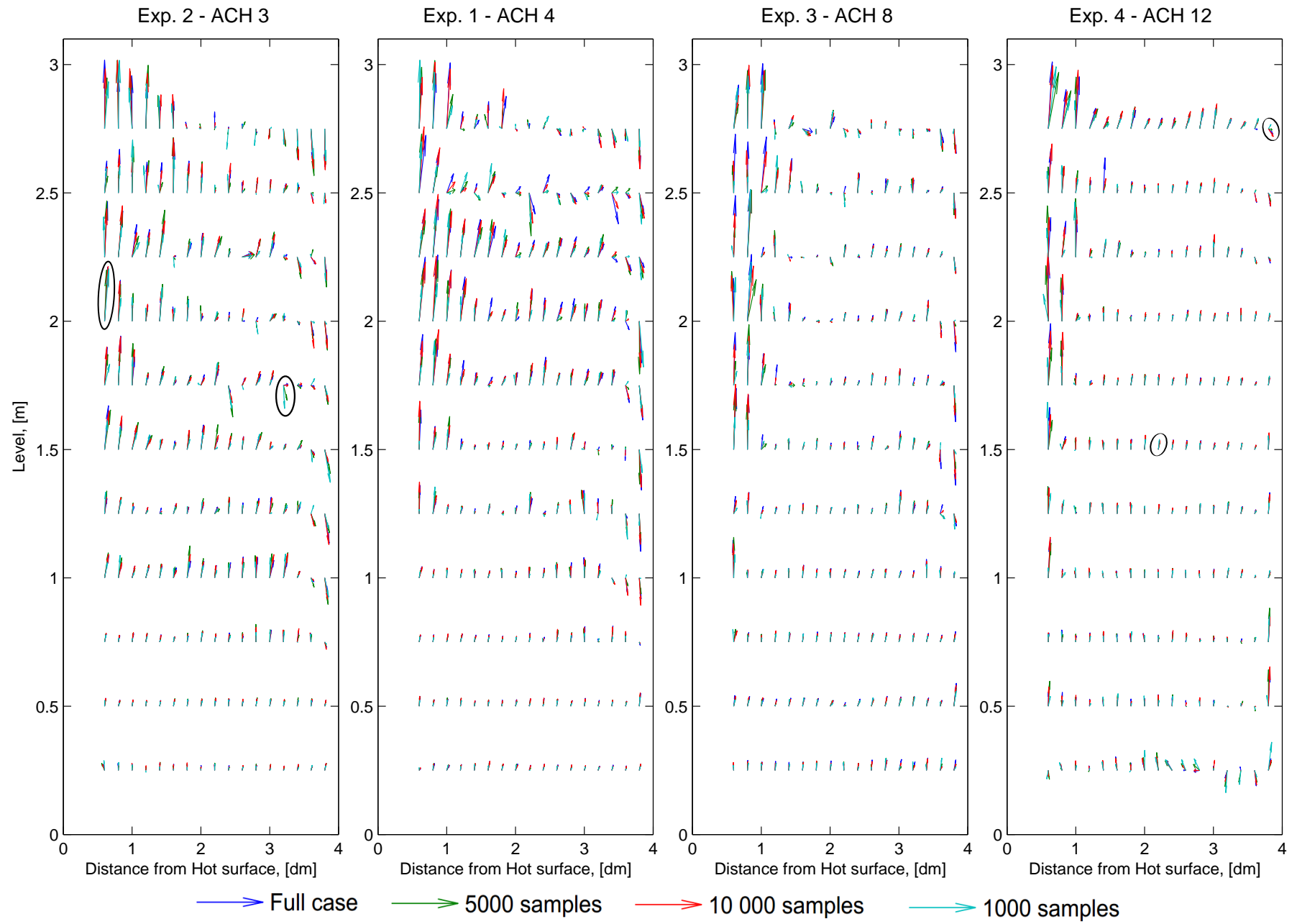


Figure 7.35. Stability of vector measurements (Group 1)

The following fluctuation analysis is more comprehensive in terms of velocity distribution in time and expands the understanding of the flow conditions inside the cavity. The analysis is presented on figure 7.36. The results give quantitative review of the standard deviation based on the averaged velocities from each 1000 samples from the dataset. The results are showing similar trend to figure 7.35, but give as well the numerical values of the flow fluctuations. In a certain aspect this analysis can be regarded as a flow stability with time, due to the method of post-processing the raw data. However it is addressed as Fluctuations analysis for simplicity. It should be noted the the Fluctuations and later the Turbulence analysis use the same interpolation procedure explained in chapter 7 to construct the contour plots. This would generate uncertainty in vertical direction, because of the distance between the measuring levels. Therefore the results should be analyzed with caution.

Starting with Exp 2 on figure 7.36 is visible that biggest fluctuations among the averaged values are measured in the top of the cavity at the hot surface. The overall picture however shows more regions with higher than 0.02 m/s fluctuations in the cavity compared to the last two cases. Similarly to the previous analysis the increase of air-change rate causes the decrease of fluctuations. Still the hot surface boundary layer is the region with highest values for each case.

On the other hand at the cold surface can be seen fluctuations too. Compared to the hot surface they are smaller in magnitude. However these fluctuations exist and as analyzed earlier they diverse in direction, which is in contrast to the hot surface, where diversity is visible mainly in the magnitude of the vectors.

The bottom of the cavity in the first three experiments has stable velocities with time based on figure 7.36 on the following page. At the last case (Exp. 4) the influence mentioned above from the higher ACH can be noticed, in the slightly increased fluctuations.

Even though it is obvious, in conclusion can be said that the increase of air-change rate leads to wash out of the buoyancy effects and creating of standard channel flow inside the cavity. The thermal processes are suppressed and stronger heat dissipation is seen in the core of the cavity. In this way no overheating of the internal air can be experienced with high ACH. Additionally, the lowest air-change rates show that with the dominance of buoyancy over the flow are generated higher velocities in the hot boundary layer. This increased momentum at the hot surface then reflects on the cold boundary layer by increasing its strength. The strong buoyancy forces generate as well uncertainties in the velocities in both boundary layers and in the upper part of the cavity. In terms of temperatures cannot be seen any difference at the surfaces, between the two extreme cases. However the thermal behavior of the bulk air in the cavity is affected.

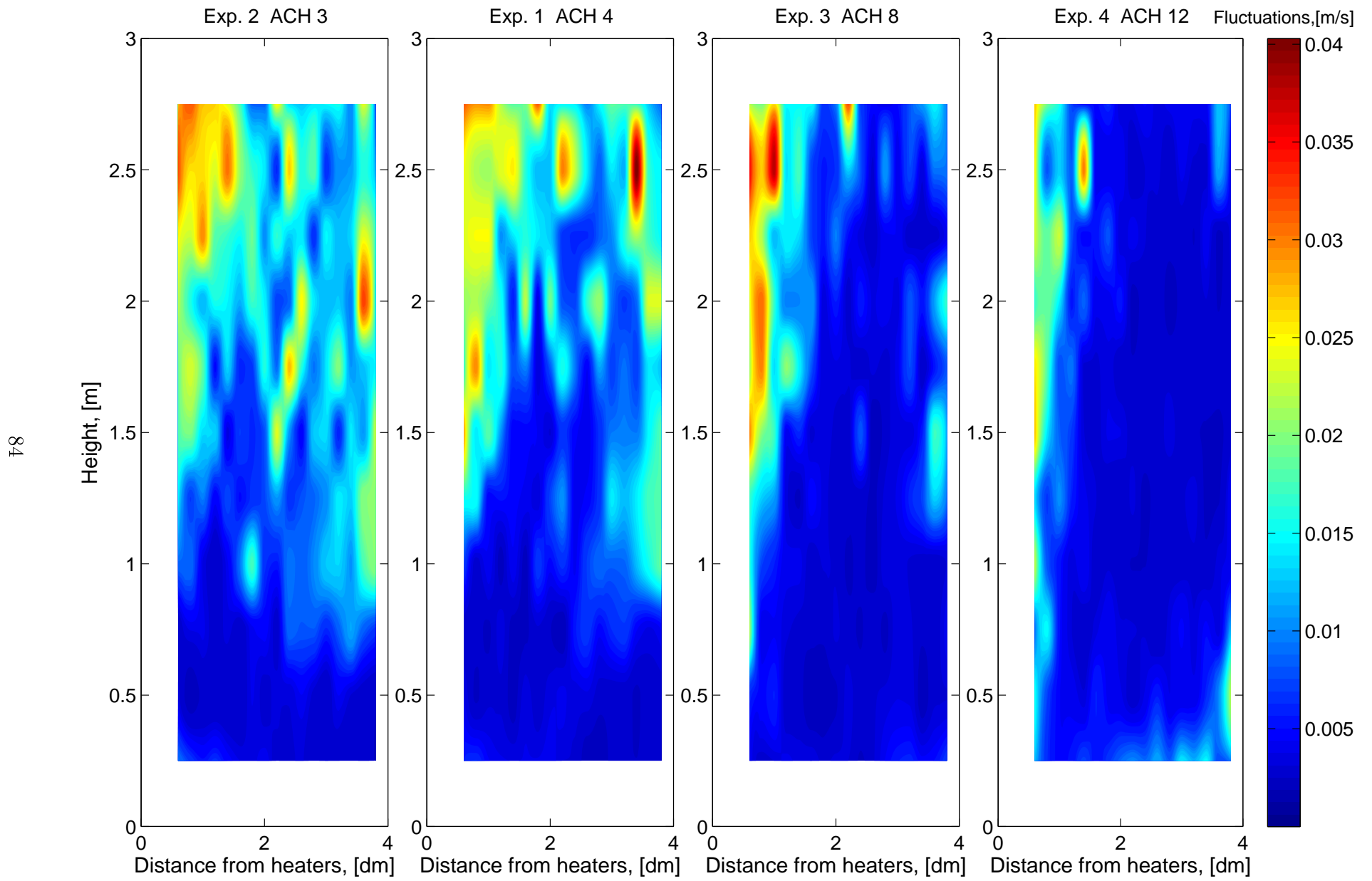


Figure 7.36. Fluctuations comparison (Group 1)

Following the baseline experiment, where was proven that the flow in the cavity is turbulent by the dimensionless numbers and the turbulence plot, turbulence in Group 1 cases is compared in the same manner. On figure 7.37 on the next page is presented the turbulence levels calculated according to equations 7.2 and 7.3 on page 48. The turbulence level quantifies the oscillating part of the velocity and helps to form an overview of the flow inside the cavity.

Observing the turbulence levels can be stated that the entrance region turbulences are caused by the supplied fan flow, and more precisely by the supply opening grill, which was mentioned earlier as a potential cause. A clear pattern of the increase of turbulence with ACH is also visible. The higher air-change rate generates stronger turbulence fluctuations in the entrance region, but also higher in the cavity. There is slight difference in the turbulence levels between the last two experiments, which deviate from the pattern. Experiment 3, shows much higher turbulences in the entire measurement volume. Still the highest values are situated in the entrance region, which is consistent with the rest of the experiments. Additionally, the first two cases show similar results in the entire cavity, where lower ACH arises less turbulence in the entrance region. Slightly higher levels can be seen at the top of the experimental volume in all cases. These turbulences might be generated by the end of the experimental channel. Again the range of turbulence variation is small and lack of values close to zero leads to assumption that the flow is turbulent in the entire cavity.

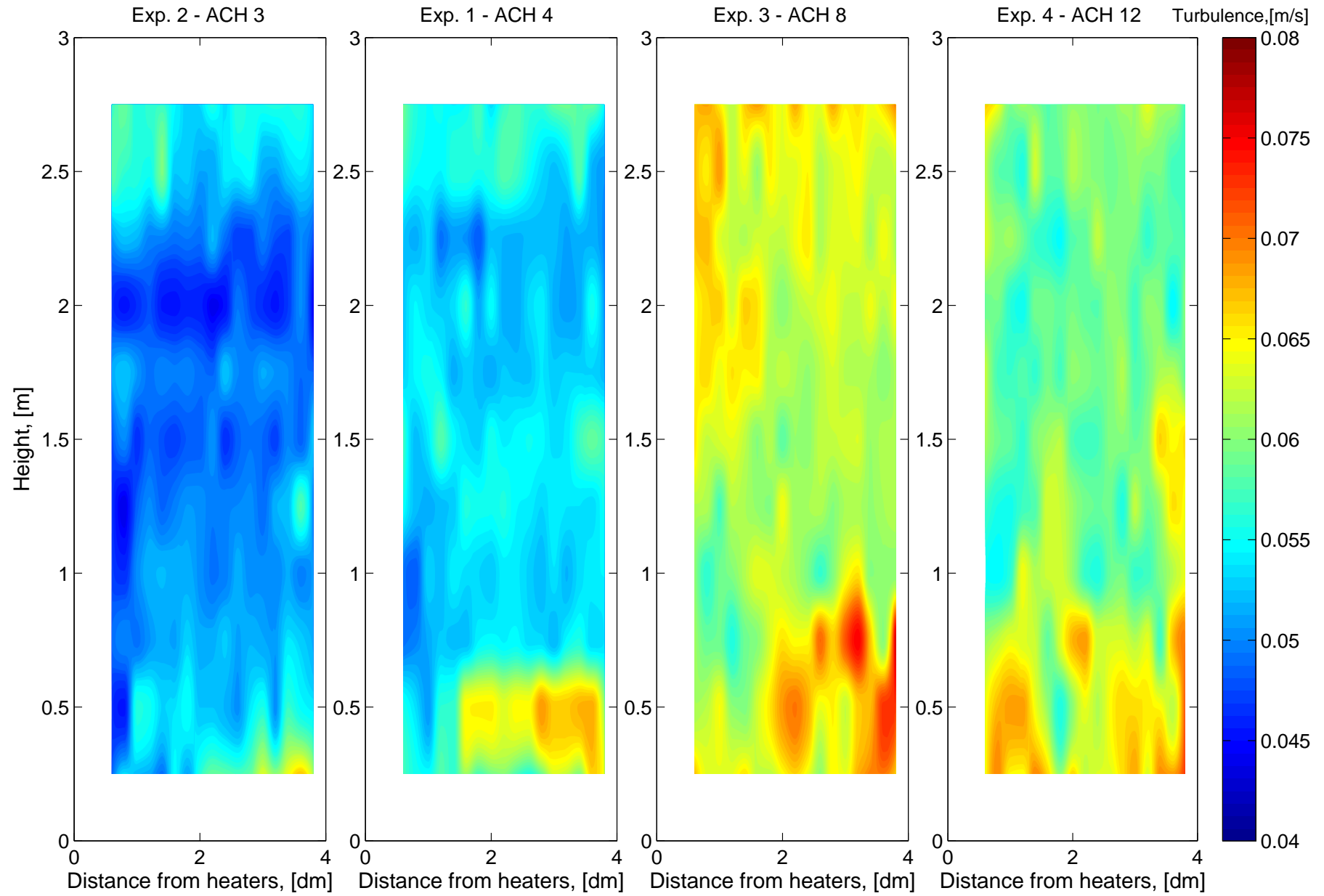


Figure 7.37. Turbulence with variation of ACH (Group 1)

7.2.3 Dimensionless analysis

Comparison of the dimensionless numbers is summarized in table 7.4. In the table can be seen that the increase of ACH changes the Reynolds criteria, which rises the inertial forces influence on the flow. The used velocities are calculated based on the supply fan flow-rate with regards to the cross section of the cavity. Therefore the influence of the buoyancy driven flow is not regarded for the calculation of Reynolds number. However the experimental velocities presented on figure 7.29 for the bottom of the cavity show results close to the calculated analytically in the biggest ACH cases. When comparing the Gr_H/Re_H^2 ratio the difference between Exp.2 and 4 is approximately one order of magnitude. Nevertheless, this still classifies the flow, with ACH 12 in the cavity as free convection, since the value is much higher than one. Rayleigh number in all cases results in values higher than 10^9 therefore the free convection regime is determined as turbulent.

Table 7.4. Dimensionless numbers comparison (Group 1)

	Exp. 2 (ACH3)		Exp. 1 Baseline		Exp. 3 (ACH8)		Exp. 4 (ACH12)	
	Hot	Cold	Hot	Cold	Hot	Cold	Hot	Cold
Gr_H	4.60E+10	3.87E+10	4.86E+10	4.11E+10	4.76E+10	3.93E+10	4.81E+10	3.99E+10
Pr	0.7026	0.7027	0.7026	0.7028	0.7026	0.7028	0.7026	0.7028
Gr_H/Re_H^2	1.80E+05	1.51E+05	1.07E+05	9.07E+04	2.64E+04	2.18E+04	1.19E+04	9.86E+03
Ra_H	3.23E+10	2.72E+10	3.41E+10	2.88E+10	3.34E+10	2.76E+10	3.38E+10	2.80E+10
Re_H	506		673		1343		2012	
Velocity cross section(m/s)	0.0025		0.0034		0.0067		0.0100	

Based on the hot and cold surface results there is no major difference between the cases. They are in the same magnitude, but give the idea about the range of variation that could be expected inside the asymmetrically heated channel.

7.3 Comparison group two - surface temperature variation

For the second experimental group is varied the heated surface temperature. This is done by maintaining the same ACH and inlet temperature. The reason for these experiments is the need to observe what is the influence of the hot surface temperature on the flow conditions. Table 7.5 summarizes the experimental boundary conditions. The achieved heaters temperatures show some difference from the desired set-points. The reasons for this are explained earlier in section 6.2. Temperatures at the glass surface and at the centerline of the gap are linked to the increased hot surface temperature proportionally. Inlet temperature is varying between the cases and it is visible that it is higher for the case with highest laboratory temperature (Exp. 6). The volumetric flow rate is rather stable between the different experiments.

Table 7.5. Group 2 empirical boundary conditions

Exp. №	ACH, [-]	$T_{heaters}$, [°C]	T_{glass} , [°C]	$T_{gapcenter}$, [°C]	T_{inlet} , [°C]	$T_{laboratory}$, [°C]	\dot{V} , [m^3/h]
1	4	27.91	26.02	26.48	15.77	23.72	5.68
5	4	26.06	25.50	25.45	16.04	24.17	5.60
6	4	34.54	29.16	30.86	16.39	24.37	5.63
7	4	37.88	30.18	32.63	16.01	23.80	5.71

7.3.1 Temperature distribution

On figure 7.41 on page 90 the averaged temperatures contour plots for the four cases are presented. The scale for each plot is individual due to the high difference in temperatures, therefore comparison between the plots cannot be made base on color similarities.

Starting with Exp. 5 on figure 7.41 the zone above 1.5 meters has nearly uniform temperatures. This includes not only the gap but the surfaces as well. The reason of conducting such an experiment was to observe the possible flow distortion in the channel with very small temperature difference between the surfaces. The entrance region in this case reminds of the previous experiments, where the core and glass surface vertical temperature distributions cross at certain height. This height is marked with a horizontal black line on figure 7.41.

The surface temperatures are better visualized on figure 7.38. Here can be seen a small temperature difference between them above 1.50 meters. The core and glass temperatures also completely overlap above 2.00 meters. Also, between 1.00 and 2.00 meters they are very close to each other. The difference is assumed to be caused by the heaters which are slightly warmer in this area. At height 1.00 meter exists the plane at which the temperature of the core reaches the one of the glass surface as mentioned before.

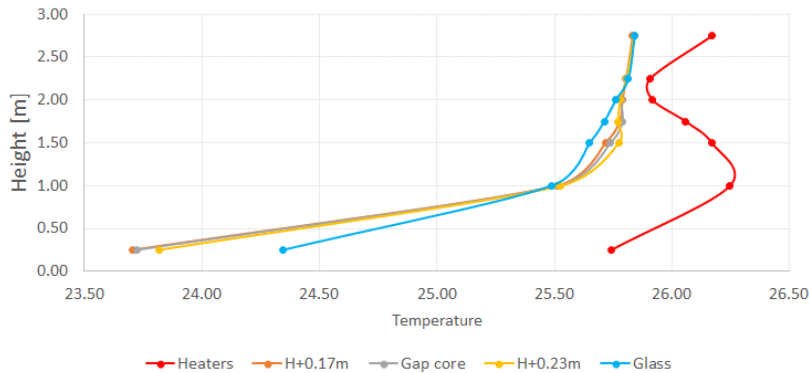


Figure 7.38. Vertical temperature distribution Exp. 5

Further on figure 7.41, with increase of the hot surface temperature to 35°C (Exp 6) becomes visible how the horizontal temperature profile at the inlet region changes. The temperatures at the glass surface in this case are lower than the ones at the core. This is determined by the stretching of the blue region at the bottom of the plot along the glass

surface. The labeled isotherm in this region is 28.25°C, which means that the inlet air was overheated with approximately 12°C in the first 25 cm of the cavity.

A better overview of the horizontal temperature distributions is seen on figures 7.39 and 7.40, for Exp. 5 and 7. Observing figure 7.39 is visible the difference in the temperatures at the glass surface and the air in the cavity. With increase of height can be seen that the glass surface and core temperatures are almost equal. It should be noticed that the temperatures above 1 meter are almost overlapping in the core of the cavity.

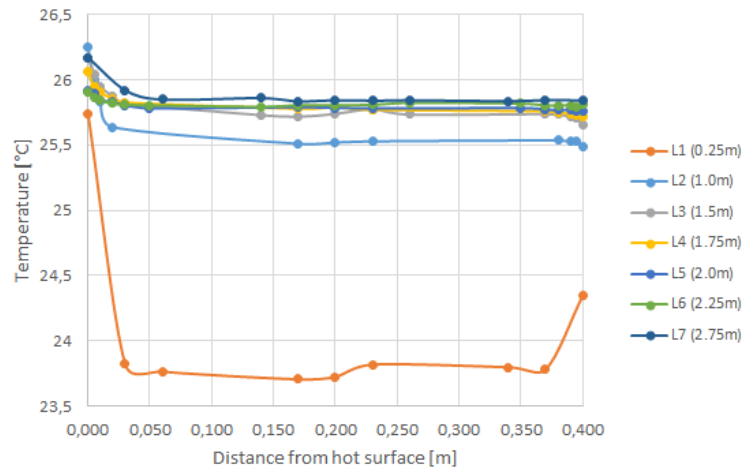


Figure 7.39. Horizontal temperature distribution Exp. 5

In the other extreme case, where the hot surface temperature was increased to 38°C, more spread out temperatures are visible in the upper part of the cavity. As well the temperature profile at the bottom level is not the same. The core temperature is higher than the glass surface temperature. These plots in combination with the contour plot clarify the overall temperatures distributions inside the cavity.

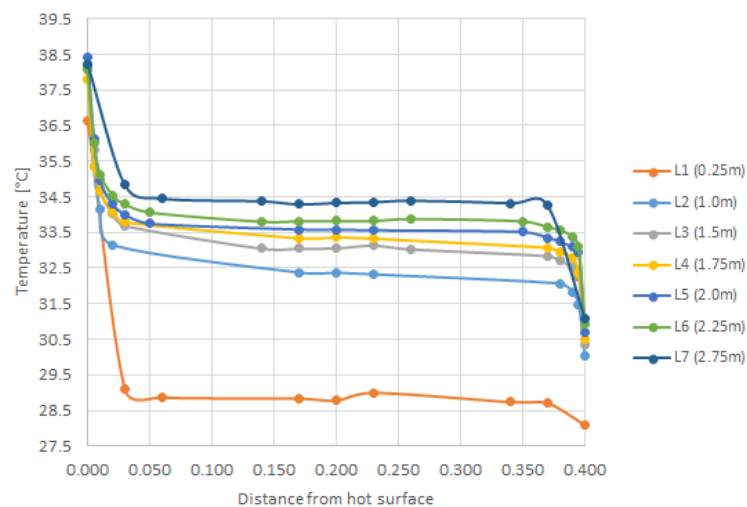


Figure 7.40. Horizontal temperature distribution Exp. 7

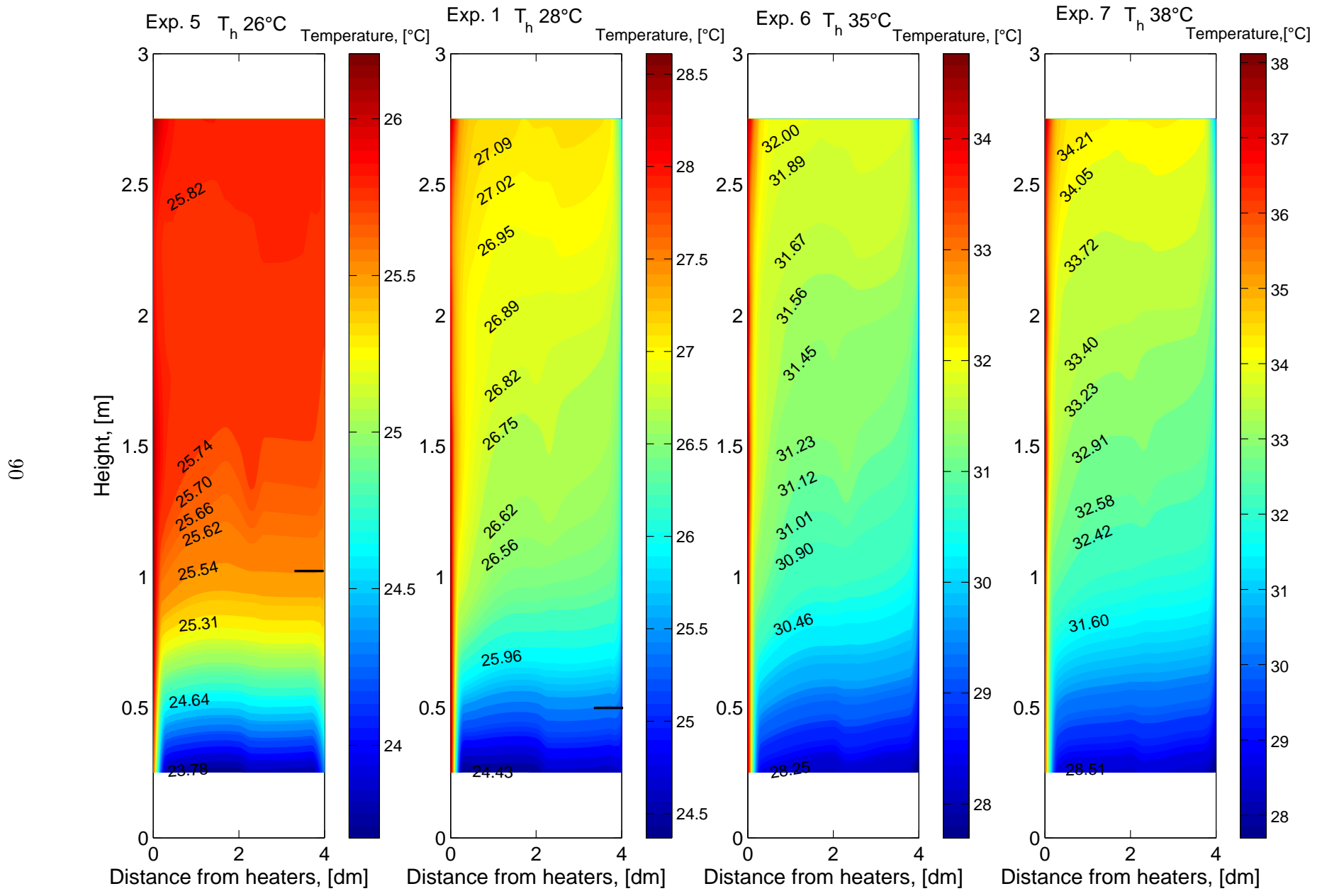


Figure 7.41. Temperatures comparison with variation of surface temperature (Group 2)

The surface temperatures for Exp. 6 are presented on figure 7.42, with the vertical temperature profiles. In this plot the difference between the surface temperatures is much higher than in the previous case. This affects the core vertical temperatures in such a way that they no longer intersect with the glass surface. In other words the inlet air is overheated faster in the entrance region.

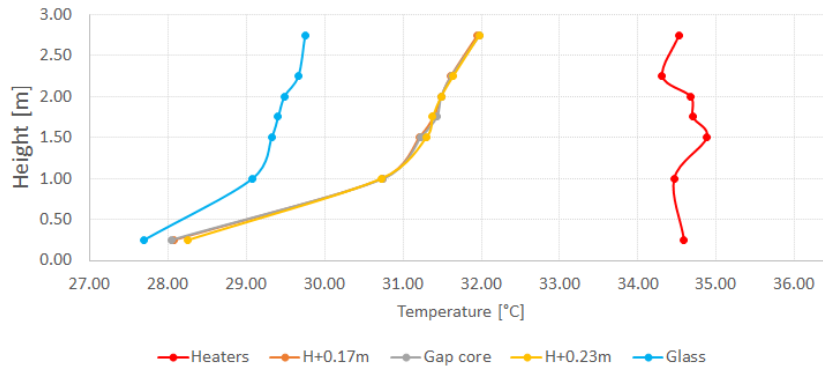


Figure 7.42. Vertical temperature distribution Exp. 6

The final experimental case variation has 38°C at the hot surface (Exp. 7), which means that a temperature difference between the inlet air (16°C) and the hot surface of 22°C is generated. The contour plot does not give specific information about the surface temperatures, but on figure 7.43 the vertical temperature distribution does. It can be seen that the bottom heater temperature deviates from the rest with approximately 1.5°C . This is caused by a lack of heating power at that location. However the limitation is accepted for the current case.

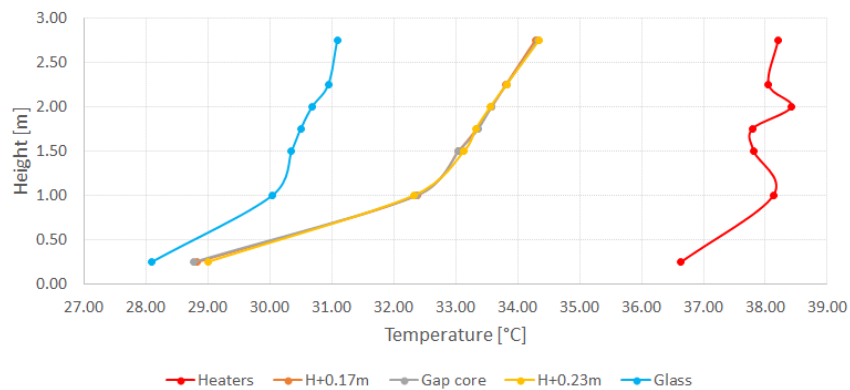


Figure 7.43. Vertical temperature distribution Exp. 7

Observing figures 7.38, 7.42, 7.43, can be seen the trend of increasing the slope of the core temperature with increase of the ΔT . In the last case (figure 7.43) the temperature difference between 1.00 and 2.75 meters is approximately 2°C . This contrasts with the baseline experiment where almost linear vertical temperature distributions were observed in the core.

7.3.2 Velocity distributions

The velocity plots presented on figure 7.44 are scaled according the highest values of all four experiments. The key vectors' information is extracted at the bottom of each plot and the vectors are circled according to the color legend.

Starting with the first case (Exp. 5) the velocities are uniform in magnitude and direction up to height of approximately 1.25 meters. The maximum value for the experiment is also noticed at height of 1 meter. Referring to the vertical temperatures on fig. 7.38, can be seen that up to height of 1 meter both surfaces are hotter than the fluid inside. When comparing back to the velocities the results lead to the assumption that standard channel flow develops up to that height. This is considered the reason for the uniform flow at the bottom of the gap.

Above the level of 1.5 meters can be seen weak development of a hot surface boundary layer. Since the driving force due to buoyancy is decreased, the velocities there are lower than the ones in the bottom of the cavity. However they are still higher than the core section at that height. At heights between 1.50 and 2.75 meters in the core region can be seen velocities in all directions with extremely small magnitude. A prove of this is at height of 2.25 meters, where the entire velocity level points upwards, while bellow and above it the vectors directions are opposite. These results can be assumed as pure mixing.

The red mark on figure 7.44 states the approximate termination plane of the cold surface boundary layer. Comparing between all cases cannot be seen specific trend of the red mark position. Additionally the position itself is determined purely visual, so it is not a certain statement of the plane height.

The one trend that can be seen is that with increase of the surface temperatures boundary layers and velocities in the cavity substantially increase. The maximal velocity can be seen in the last experiment's boundary layer, with a value of 0.130 m/s, which is almost 0.1 m/s bigger than the maximum in Exp. 5.

Experiment 6 can be compared to the baseline case (Exp. 1) in terms of velocity pattern. However, the substantial difference between the cases is the general velocity level. With the higher surface temperature almost twice bigger velocities are generated in the boundary layer, compared by maximum value. At heights of 2.25 m and 2.50 m a similarity can be seen between the two cases. In both the boundary layer thickness increases and then suddenly decreases. These instabilities at the edge of the boundary layer can be interpreted as eddies or vortexes.

Additionally with the increased temperature difference in Exp. 6 can be seen thicker cold surface boundary layer. This thickening is accompanied with horizontal vectors at the edge of the boundary layer, which represent a healthy development. Both of the above statements justify the higher momentum forces created by the increased surface temperature. Due to this stronger boundary layer the termination plane (red mark) drops compared to the previous case (Exp. 1).

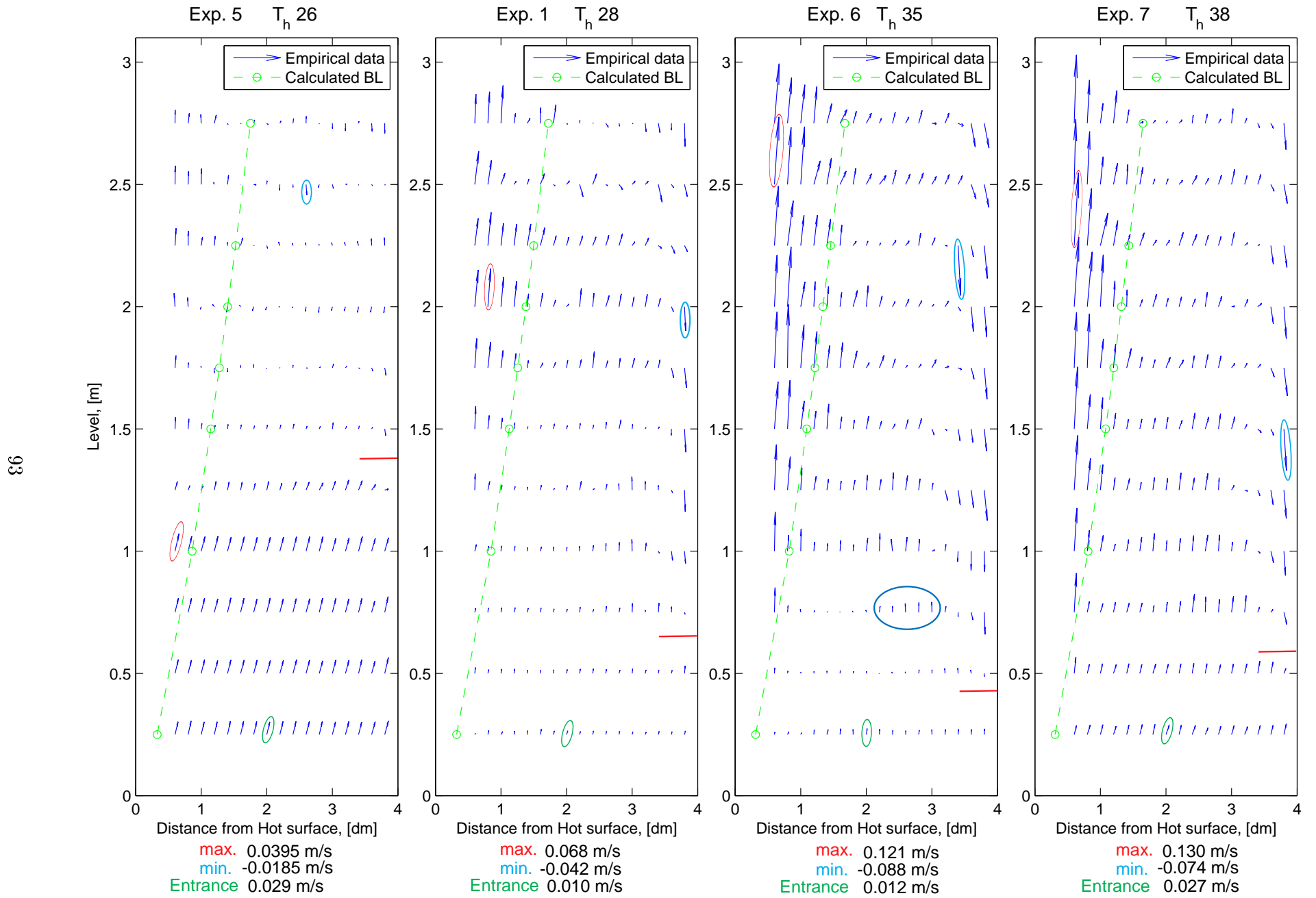


Figure 7.44. Velocity comparison for different hot surface temperatures (Group 2)

Comparing exp. 6 and 7, no marginal difference can be seen in terms of velocities in the boundary layers. Still at the bottom of the cavity in the last case, the measured velocities are twice bigger than the ones in Exp. 6. This is assumed to be the reason of the termination plane (red mark) raise in this case. These increased velocities can be connected to the higher buoyancy forces enforced by the rise in temperature. One may argue that judging by the fan supplied flow-rate, where only $0.1m^3/h$ higher average value was calculated for Exp. 7 might be an influence over the supplied velocity. However, it is assumed by the authors that this should not impose such an influence on the velocity at the bottom of the cavity.

Additionally the region circled with blue on Exp. 6, figure 7.44 is similar to the one observed in the previous experiments. It is well outlined, by the higher velocities in the circle, that in this region concatenation of flows is present. The same assumption applies that the cold boundary layer is reversing and uniting with the uniform flow from bellow. Experiments 1 and 7 show also this region, but it is harder to notice due to the smaller difference in the velocity vectors, caused by the scaling.

Further colorful contours show the velocities inside the cavity. Starting with Exp. 5 is seen that above 1.5 meters the velocities are very close to 0 in the core and slightly higher in the hot boundary layer. Observing the general picture for the rest of the cases is clear the increase of boundary layers strength with temperature. It can be observed also the trend of restraining the boundary layers and allowing further penetration of the core flow.

The boundary layers, however are not consistent in their development, meaning that they thicken and thin out in a seemingly random manner. This could be connected to vortexes and instabilities. Paying attention to the hot surface boundary layers in cases 1 and 6 shows precisely these fluctuations. Another observation is made regarding the hot surface boundary layers, that with increase of the surface temperature the development of the boundary layer starts lower in the cavity. On figure 7.45 can be seen that for Exp. 7 the boundary layer entered the measurement area at height of approximately 0.5 meters, while in the baseline this happens at height of 1.00 meter.

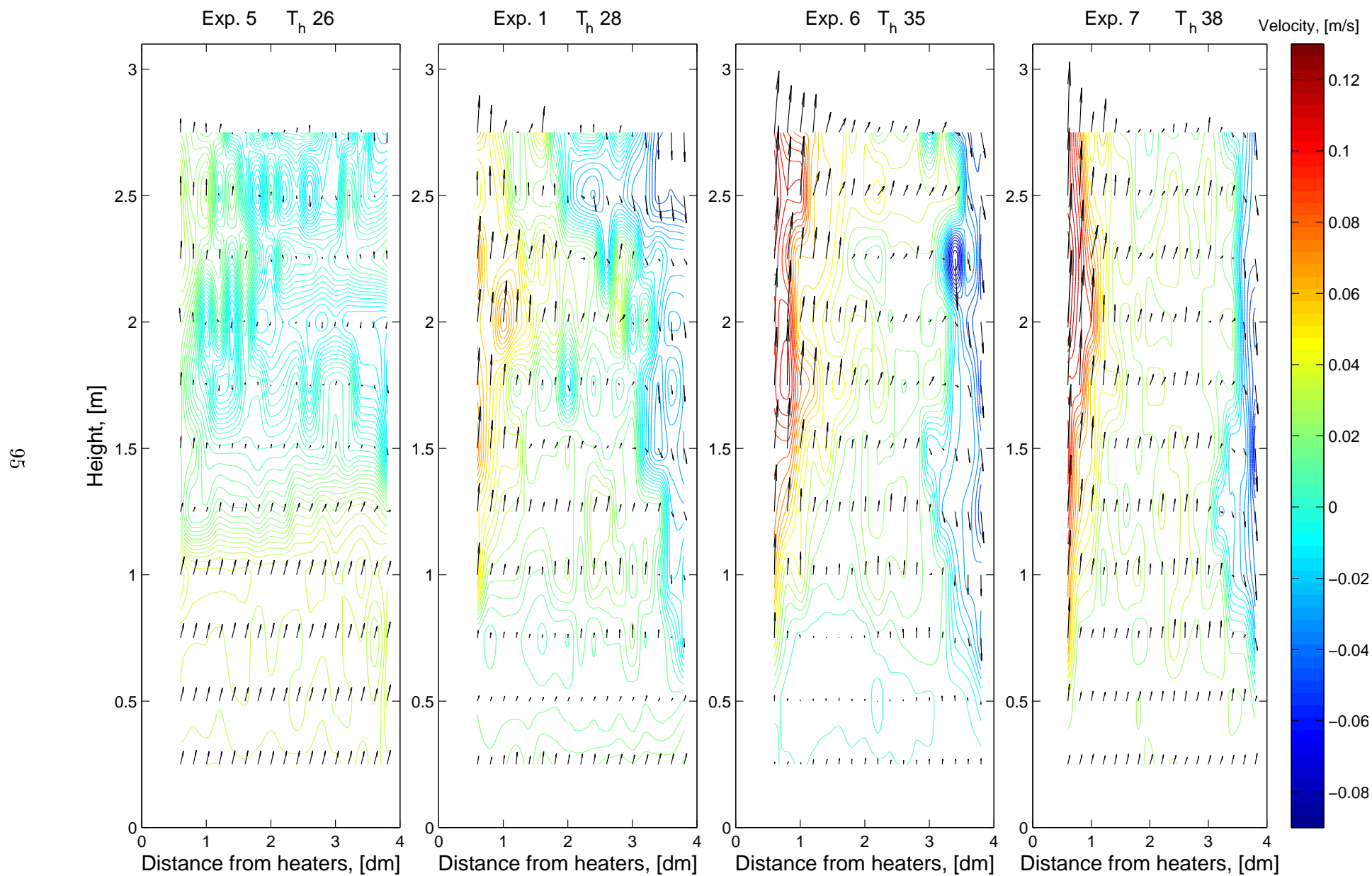


Figure 7.45. Velocity comparison contour for different hot surface temperatures (Group 2)

Figure 7.46 presents the flow stability with time, based on the averaged values from the samples datasets. The same manner and color legend is used as in the previous experiments. The difference in these experimental plots is that they are not scaled together, meaning they cannot be compared between each other. A scaling of the cases will result in decreased visibility of the interesting regions. The analysis gives not only the difference in the average velocity, but as well the variation in the flow direction with time.

Starting from left to right on figure 7.46 can be seen that for the upper part of Exp. 5 unstable in magnitude and direction velocities are obtained. This is related to the mixing flow in the region, which was already assumed based on the previous figures. At some locations can be seen changes in direction throughout the sampling period. Some of the locations are outlined with a rectangular shape. It is visible that these locations are spread all over the upper part of the cavity in this experiment. There is no certain pattern that could be assumed based on these results.

Taking a closer look to Exp. 6 is visible that with the increased temperature, the variations in the vectors directions decreases. Clearly there are still vectors with discrepancy in magnitude in all positions, but the ones with different directions are restricted to the edges of the boundary layers. The same observation can be made for Exp. 7.

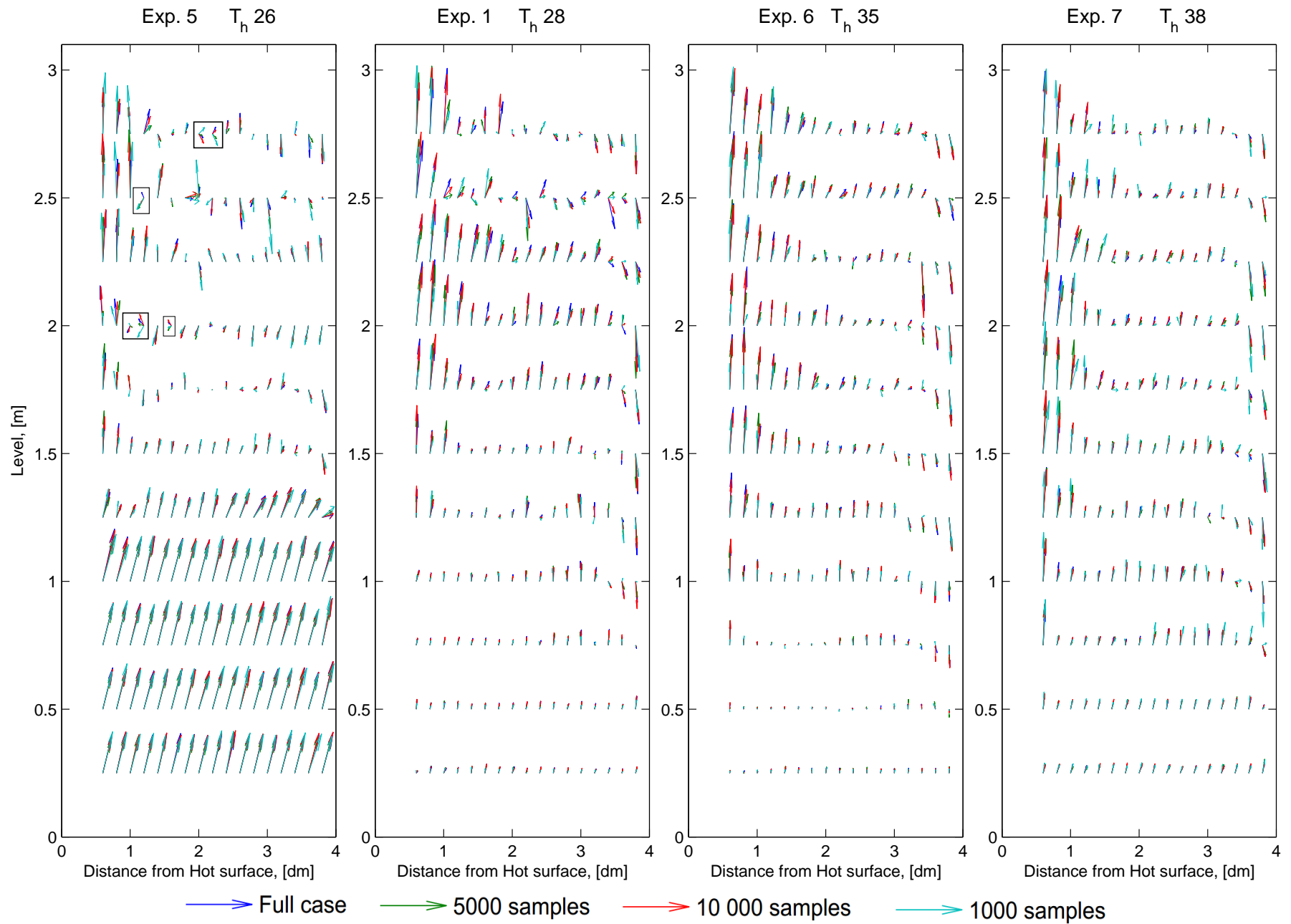


Figure 7.46. Stability of flow velocities (Group 2)

The next type of analysis shows a different data treatment method of the velocities inside the cavity. The fluctuations levels on figure 7.47 are compared using the before mentioned in section 7 data treatment techniques. The plots show the flow deviation with time during the measurement interval.

The fluctuations on figure 7.47 are based on the standard deviation of the averaged values of every 1000 samples from acquired horizontal and vertical velocities. In this way the velocities are strongly time dependent. One may argue that this type of analysis will under estimate the velocities and would be right for case where the flow conditions are stable. However, the current case has an unpredictable flow patterns, which occur and disappear in a short time interval. To account for that is used the presented analysis.

In Exp. 5 can be seen that the graph is almost uniform color and no fluctuations are visible. This is caused by the extremely small velocities in the upper part of the cavity, where even if instability occurs due to the small scale it cannot be visualized. Additionally, at the bottom of the cavity in the previous graphs for Exp. 5 were seen only uniform velocities, which does not generate any instability.

Proceeding further on figure 7.47, with increase of the driving force, instabilities become more visible. The fluctuations in Exp. 6 and 7 get the form of the hot surface boundary layer and spread towards the cavity core. Based on this can be said that precisely the boundary layers have the most uncertain flows conditions in terms of velocity magnitude.

Comparing the most intense fluctuation on figure 7.47 at 2.25 m height and $h+34$ cm for Exp. 6 with figure 7.45 for the same point, it is visible that there was measured extremely big velocity. This could be a result of a local vortex that occurred at specific moment. In addition, on figure 7.46 for the same location is visible that at first the velocity was small, but with time it increased rapidly.

The overall picture shows local peaks in the velocities fluctuations mainly in the boundary layers. These peaks increase with the increased buoyancy force from the heated surface. This analysis visualize accurate enough the zone with uncertain conditions.

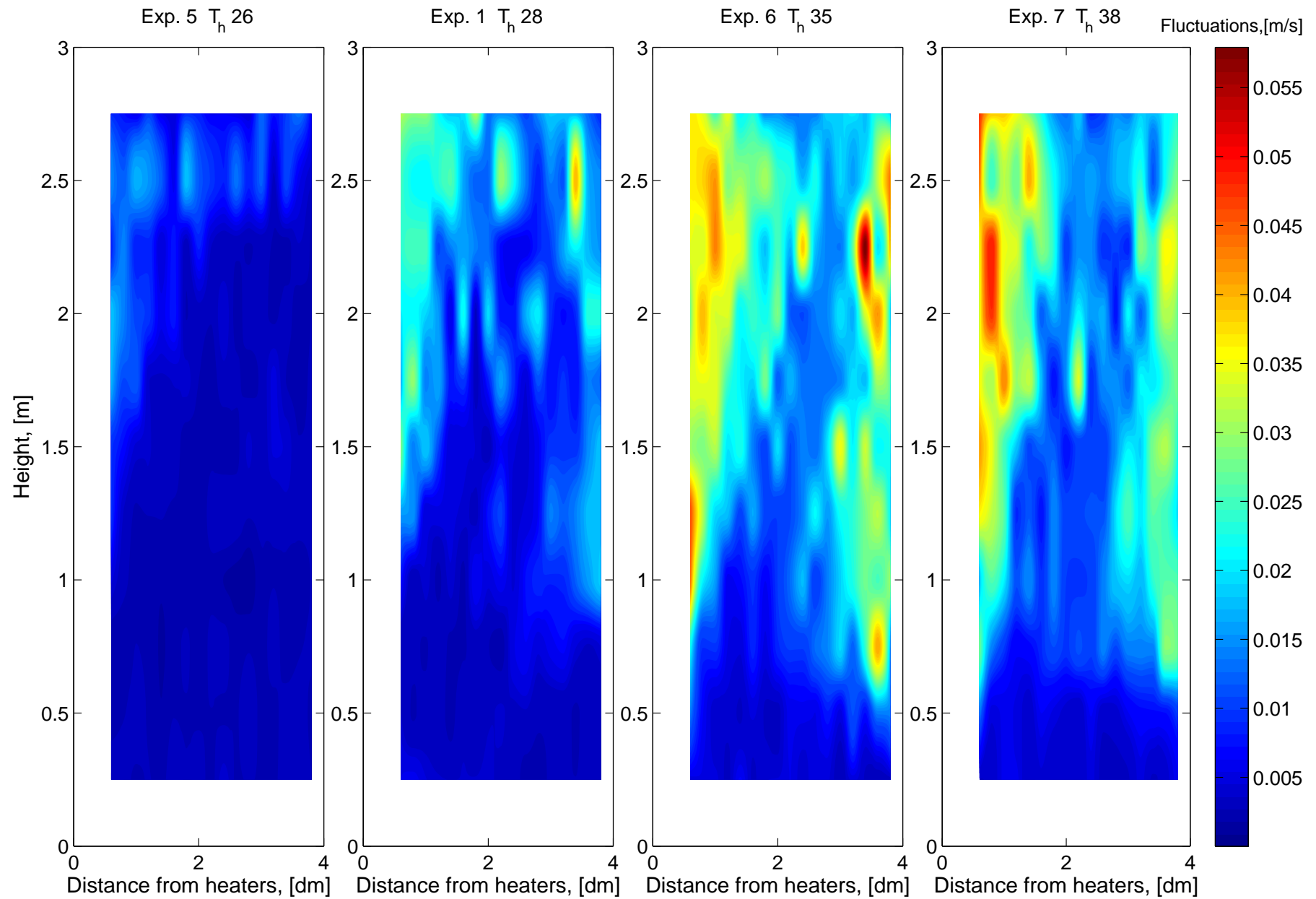


Figure 7.47. Velocity fluctuations with change of hot surface temperature(Group 2)

Turbulences in the cavity were calculated as the fluctuating part of each velocity component, based on the entire measurement data-set. The turbulences are presented on figure 7.48, where the scale for the four plots is uniform. A difference can be seen between Exp. 1 on figure 7.48 and on figure 7.37 on page 86. This is caused by the different scales for each group of experiments.

The results on figure 7.48 show strongly the influence of the inlet opening in the first two cases. The same was also concluded for the previous section (ACH variation). The inlet turbulent region in Exp. 5 is bigger compared to Exp. 1, which forms the argument, that the domination of the supplied fan flow over the buoyancy is the cause of this increase. For Exp. 5 is visible that not only at the inlet opening, but as well at heights between 1.75 and 2.25 meters are generated turbulences. On figure 7.46 was seen that for the height of 2.00 meters the entire measurement level has downward velocities except for the closest to the hot surface. This in addition to the turbulences plot, might be argued as an evidence for the uncertainty of the velocities in this region.

The last two experiments show significantly less, or almost none turbulences close to the inlet region. In Exp. 6 only scattered increases on the turbulence levels are visible at certain places, mostly in the upper part of the cavity, and close to the surfaces. In the last case, the majority of the turbulences are situated only in the hot surface boundary layer.

In another perspective, a connection can be made comparing the turbulences regions with the vertical temperatures distributions for each case. It is observed that there is dependency of the height of crossing the core and glass surface vertical temperatures with the velocity turbulence regions. Here can be seen that in the last two experiments the core temperature is not at any point lower than the glass temperature (fig.7.42 and 7.43), and almost no turbulences occur in the entrance region. The same assumption fits Exp. 5 and 1. Going back to experiments from group 1 (ACH variation) the same observation is valid. The turbulences in the entrance region are higher when the temperature difference between the core flow and the glass surface is small. When referring to figure 4.12 can be stated that conditions for mixing are present due to a small temperature gradient.

Both causes for the turbulences at the inlet region (inlet grill influence and small temperature gradient) are possible, however further investigation is necessary in order to support one of them.

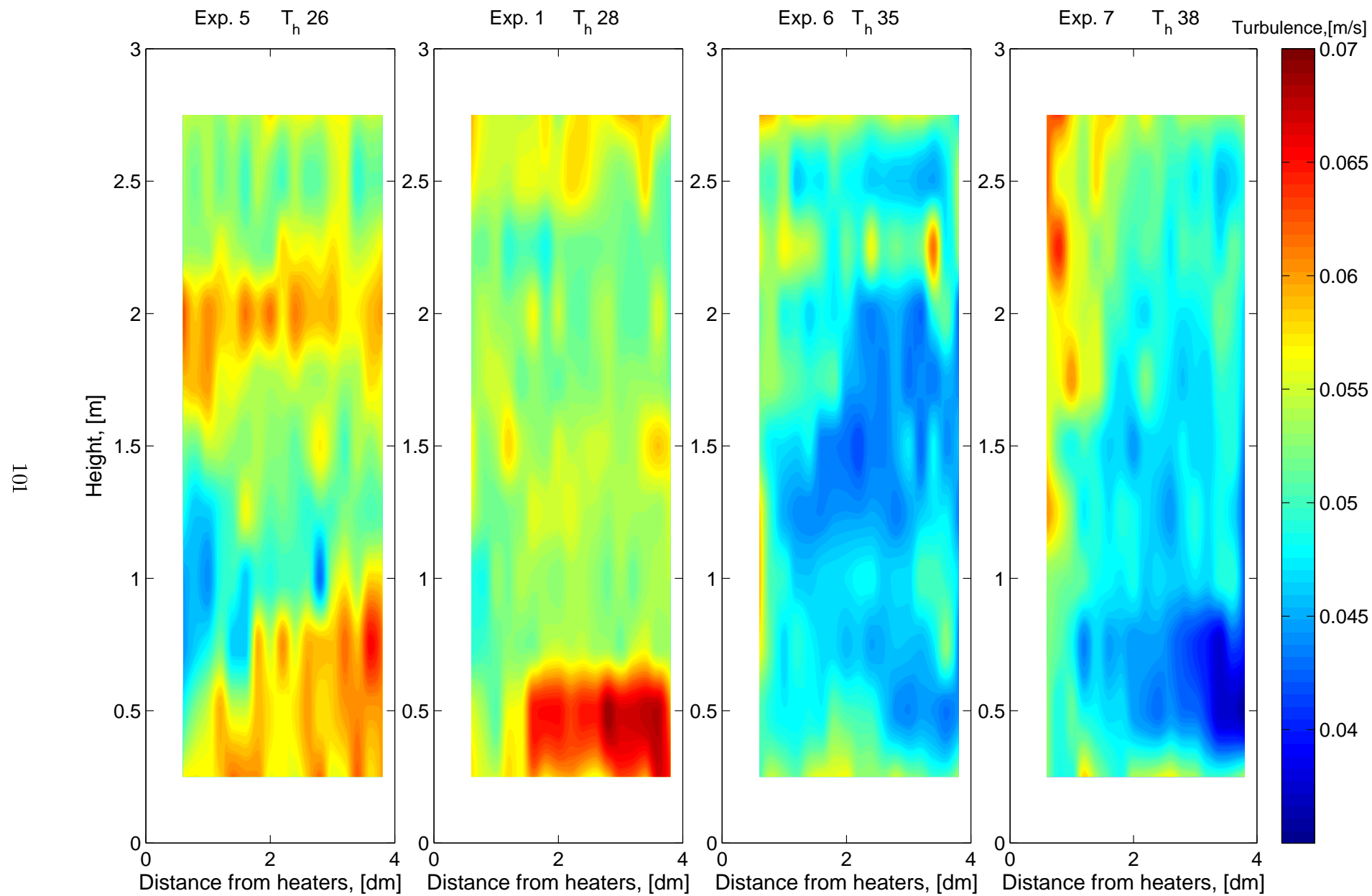


Figure 7.48. Turbulence with variation of heaters temperature (Group 2)

7.3.3 Dimensionless criteria

Calculation of the dimensionless criteria are based on the summarized in table 7.5 temperatures and volumetric flow rate. The characteristic dimension as before is the height of the cavity. On table 7.6 are shown the calculated values.

Table 7.6. Dimensionless numbers (Group 2)

	Exp. 5 ($T_h 26^\circ\text{C}$)		Exp. 1 ($T_h 28^\circ\text{C}$)		Exp. 6 ($T_h 35^\circ\text{C}$)		Exp. 7 ($T_h 38^\circ\text{C}$)	
	Hot	Cold	Hot	Cold	Hot	Cold	Hot	Cold
Gr_H	4.07E+10	3.84E+10	4.86E+10	4.11E+10	6.85E+10	4.82E+10	8.06E+10	5.22E+10
Pr	0.7028	0.7028	0.7026	0.7028	0.7019	0.7024	0.7016	0.7024
Gr_H/Re_H^2	9.15E+04	8.64E+04	1.07E+05	9.07E+04	1.61E+05	1.13E+05	1.88E+05	1.22E+05
Ra_H	2.86E+10	2.70E+10	3.41E+10	2.88E+10	4.81E+10	3.39E+10	5.65E+10	3.67E+10
Re_H	667		673		652		656	
Velocity cross section [m/s]	0.0033		0.0034		0.0033		0.0034	

Starting with the hot surface Grashoff criteria can be seen an increasing trend with the increase of temperature. Nevertheless this increase is in the range of $4.07 \cdot 10^{10}$ to $8.06 \cdot 10^{10}$, which is insignificant variation, because it does not change the assumption for buoyancy dominating force. Comparing Gr_H for both surfaces can be seen that there exists higher difference than in previous experiments, which is clearly caused by the surface temperature. The same is valid for the Ra_H , and for Gr_H/Re_H^2 ratio.

The Reynolds number is visibly slightly changing for the different experiments. This is caused by the small difference in the average volumetric supply rate, and the use of the air density ρ in the calculation, which is interpolated for the specific temperature from the tabulated data in appendix G.1 on page 146.

In conclusion the dimensionless numbers characterize the flow inside the cavity in all of the experiments as turbulent free convection.

7.4 Comparison group three inlet temperature variation

In this section are compared experiments with a change in the inlet temperature. This will show the influence of this variable parameter on the flow pattern. In table 7.7 are presented the empirical boundary conditions for two experiments compared to the baseline. Observing the average integral temperatures at the heater, glass and in the gap core small differences can be found. The laboratory temperature is also consistent. The volumetric flow rate is stabilized to very limited variation.

Table 7.7. Group 3 - Inlet temperature variation

Exp. N ^o	ACH, [-]	$T_{heaters}$, [°C]	T_{glass} , [°C]	$T_{gapcenter}$, [°C]	T_{inlet} , [°C]	$T_{laboratory}$, [°C]	\dot{V} , [m^3/h]
1	4	27.91	26.02	26.48	15.77	23.72	5.68
8	4	28.04	26.34	26.77	17.80	24.15	5.57
9	4	27.97	26.60	27.02	25.41	24.52	5.53

7.4.1 Temperature distribution

The three experiments with an inlet temperature variation are presented through contour plots on figure 7.49. All experiments correspond to the same temperature color bar. The lowest empirically achieved inlet temperature is 16°C. Due to set up limitations a maintaining of stable lower temperature was impossible.

It can be noted that with increase of the inlet temperature is increased as well the temperature of the core inside the cavity. The change as a value is not so significant, however the space between two neighboring isothermal lines expands in the upper part of the cavity. This forms regions where the variation in temperature is slightly over the thermocouples precision. The existence of zone with small temperature variations is normally accepted as well mixed.

The phenomenon of recirculation, explained by Incropera et al. [2011], includes a flow reversal in the upper part of the cavity, where the flow completely changes direction from positive to negative when approaching the cold surface. This movement of fluid would normally be assisted by temperature field redirection. Observing the contour plots this pattern can be found in the black squares. The size of the squares increases proportionally to the inlet temperature. It could be said that the heated air penetrates further downwards in the cavity, forced by the momentum of the flow. The thermal influence on the core flow is one of the main reason for existence of unstable velocity behavior in this area.

Observing the temperature distribution along the hot and cold surfaces in the cavity a difference can be noted between the experiments. The temperature boundary layer increase consistently. However, from the contour plots is difficult to estimate the thickness of the boundary layers. Therefore, the horizontal velocity distributions are presented on figure 7.50 .

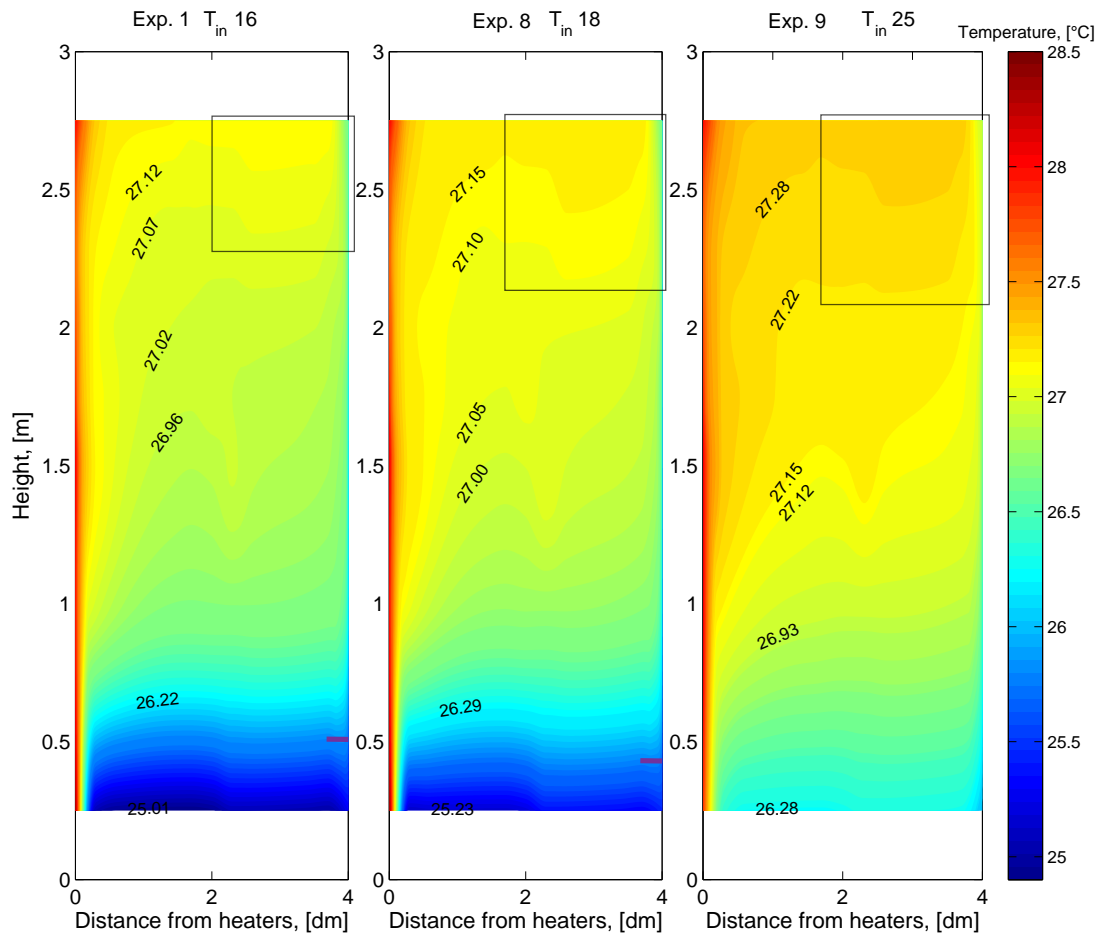


Figure 7.49. Temperatures comparison with variation of inlet air temperature (Group 3)

It should be easy to identify the thickness of the thermal boundary layers on figure 7.50, however the values that give this information are located between the measuring points. It might be misleading to conclude based on interpolated data, therefore an assumption based on theory is made. The thermal boundary layer is assumed to increase, but since there is a lack of thermocouples in the targeted areas, an exact value cannot be stated.

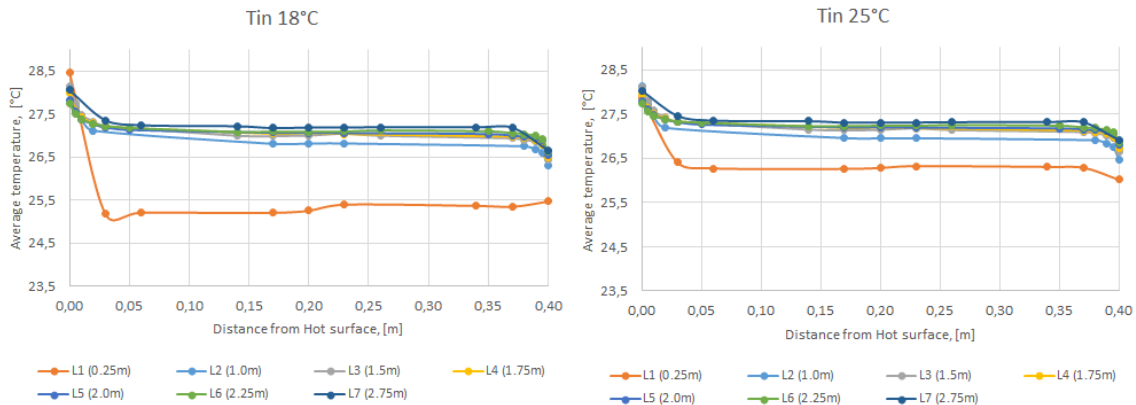


Figure 7.50. Horizontal velocity distributions for Exp. 8 and Exp. 9

In the lower part of the cavity on figure 7.49 the temperature distribution is influenced by the inlet air. It enters the cavity with the chosen temperature and is overheated by the internal flow and the heaters. By the time it reaches the measurement area the inlet air has temperature of at least 24.8°C for Exp. 1 and 26.28°C for Exp. 9. In other words, for an increase of inlet temperature with 7°C, the temperature at level 0.25m rises only with around 1°C.

Additionally, the line at which the temperatures of the core and glass equalize is marked with purple on figure 7.49 . What is different for those cases is that with the increase of inlet temperature that level drops down, where for Exp. 9 it does not exist. This is clearly shown on figure 7.51 , where the core temperature does not cross the glass temperature line. This purple lines are assumed as the limit at which there are conditions for existence of a boundary layer in upward direction at the cold surface. Clearly in this cases this possibility decreases with the inlet temperature increase.

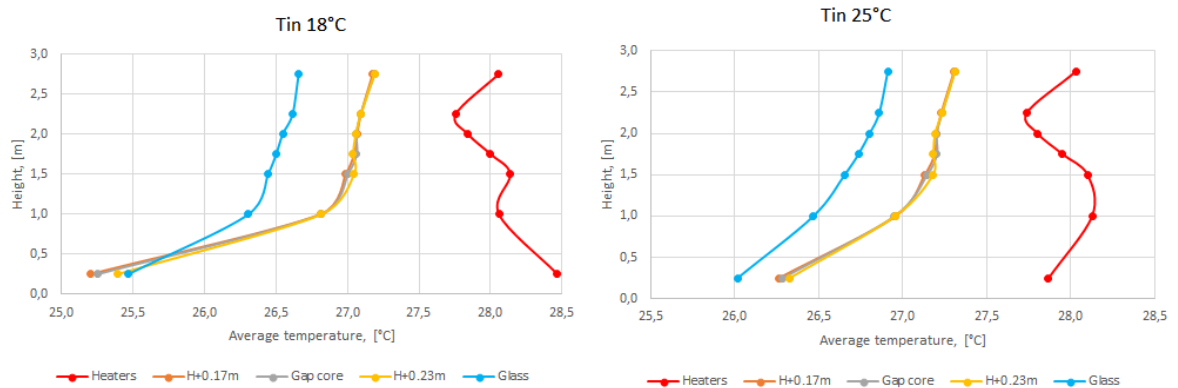


Figure 7.51. Vertical temperature distributions for Exp. 8 and Exp. 9

7.4.2 Velocity distribution

The same pattern of description is used in these experiments regarding the velocity. On figure 7.52 are presented the velocity vectors to visualize the flow movement in the cavity. All experiments are scaled to the largest velocity of all cases.

Focusing at the entrance can be seen that all cases have similar magnitude and direction of the velocity vectors. Regarding the cold boundary layer termination plane, it is expected that with increase of inlet air temperature the plane will drop. However Exp. 8 shows a slight deviation from the pattern. The reason for that is the dynamic manner of the flow inside the cavity, which might result in fluctuation of the termination plane. Another possible explanation is the increased strength of the cold surface boundary layer which pushes down the termination plane. The thickness of the cold boundary layer is bigger in the last experiment, which suggests that more air is entrained in downward direction. No conclusion can be derived from the maximum and minimum velocity in the cavity, since Exp.8 deviates in this factor as well.

Another point of view is the comparison between the calculated and the visible boundary layers. Exp. 8 and Exp. 9 show similar boundary layer collapses as in Exp. 1. The

statement for a disturbed boundary layer development in the upper part of the cavity is confirmed in all cases. However, the calculated boundary layer gives a good agreement with the empirical data until the collapsing zone is reached. Comparing the calculated boundary layers is shown that the thickness increases proportionally to the inlet temperature. The measured values also confirm the calculations. This can be better visualized on figure 7.53

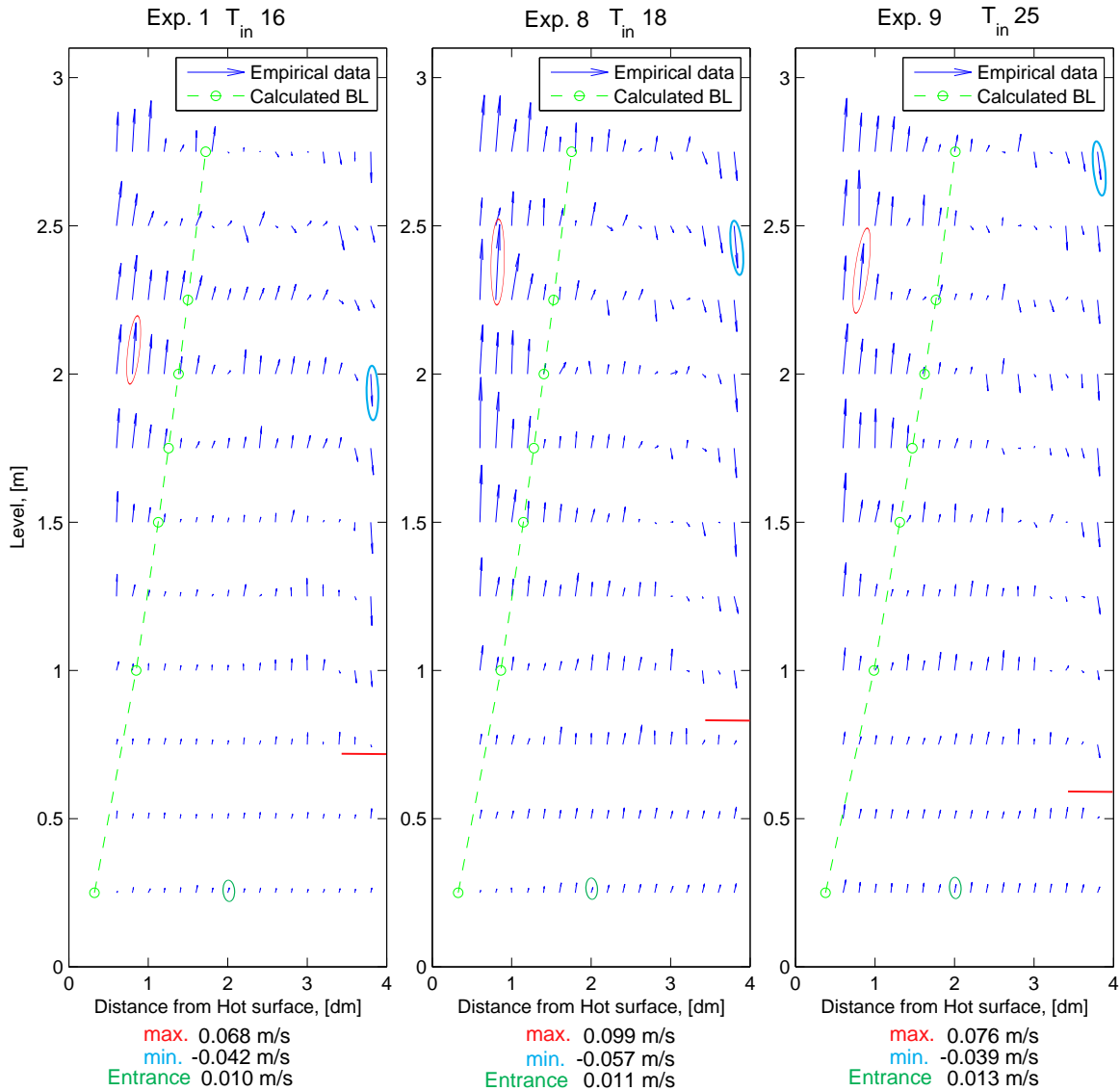


Figure 7.52. Velocity vectors inlet temperature variation (Group 3)

What the color scheme helps to differentiate is that with increase of inlet air temperature the heated boundary layer thickness is slightly increased. However, more collapses are present at its edge. The increase of temperature allows also early development of the hot boundary layer and as a result the momentum forces assist stronger cold boundary layer. The last spreads toward the cavity by increasing its thickness. This results in appearance of negative velocities at the lower levels and decrease of the upward core flow thickness. The penetration of the cold boundary layer downwards is also increased. A sign for that

is the lower cold boundary layer termination plane in Exp. 9 on figure 7.52.

An interesting hot boundary layer development is visible at the upper levels for Exp. 9. Its thickness increases steadily up to level 2.0m and after that a slight decrease is present. However, above 2.0m the boundary layer starts increasing again. Referring to the video for this case the same flow pattern is present. Which means that the mixing zone in the upper core drops down with 0.25m. Therefore, an assumption for increased mixing region can be made.

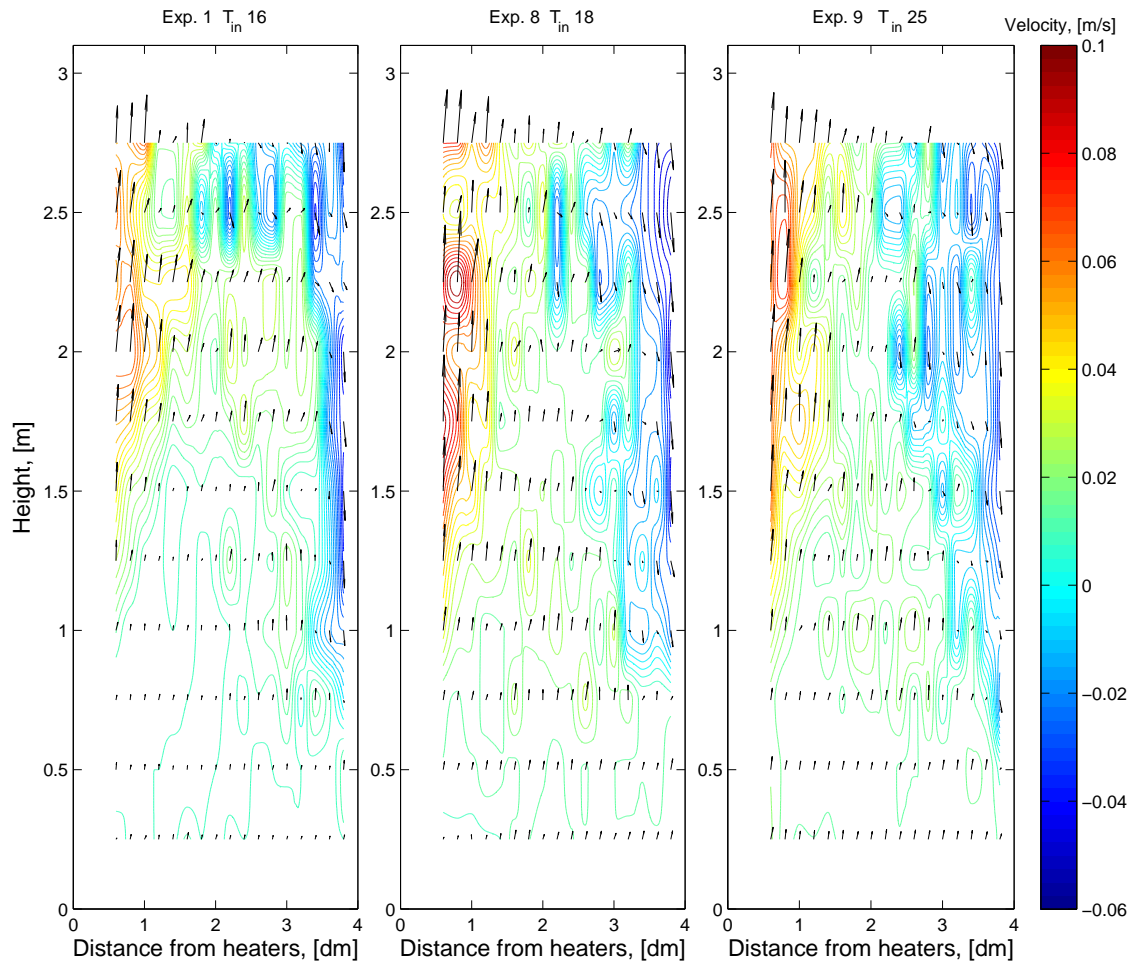


Figure 7.53. Velocity contour inlet temperature variation (Group 3)

The stability of the velocity vectors is plotted on figure 7.54 for the number of samples given in the legend. By "Full case" should be understood 15 000 samples. All plotted vectors are an average value of the given number of samples starting from the first.

It can be observed that with time the acquired velocities are changing in direction and magnitude. The explanation regarding this kind of figures in section 7.1 is relevant for these cases. The differences are again noticed only at the edges of both boundary layers and in the upper core of the cavity. As explained earlier, there is a mixing zone with lower velocities at that location, so the results are expectable. Comparing the three cases, can

be noticed that the unstable vectors zone spreads down with increase of inlet temperature. The explanation comes from the decreased temperature difference in the cavity flow and as a result are formed conditions for mixing in the lower levels.

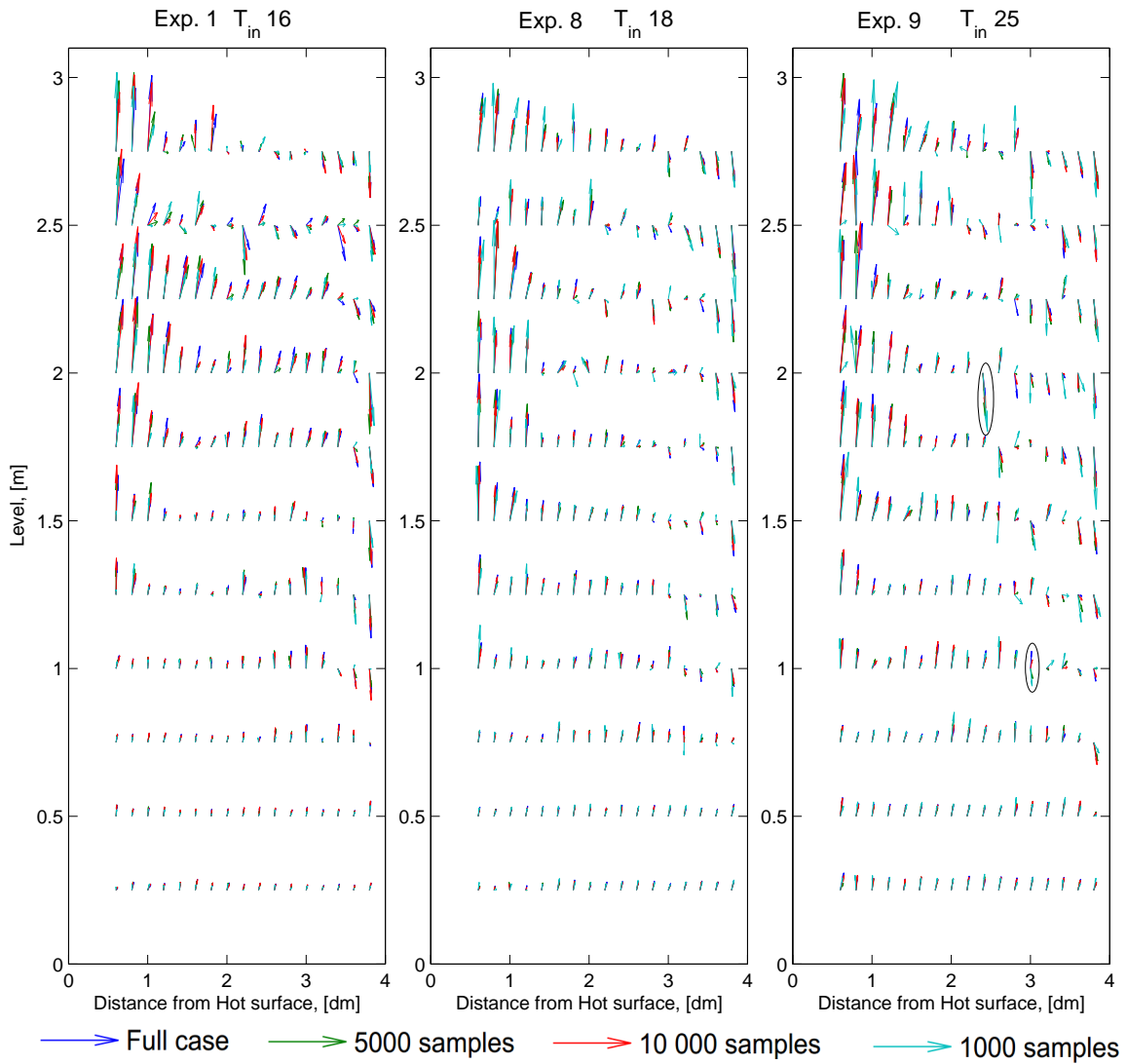


Figure 7.54. Velocity stability (Group 3)

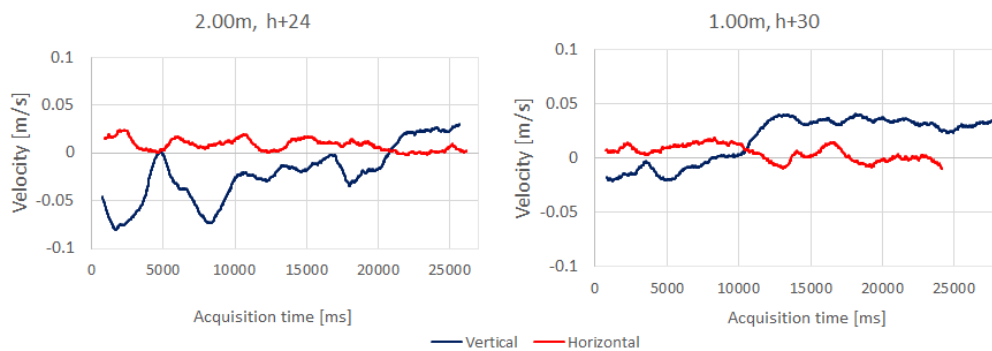


Figure 7.55. Moving average velocity with time for Exp. 9

The circled vectors on figure 7.54 are further examined on figure 7.55, where the moving average velocities are presented in relation to the arrival time. Starting with 2.00 meters height, is visible that the vertical velocity switches from positive to negative throughout the measurement time. Additionally even in the first 15 000 ms, the velocity was very unstable. Not the same can be observed in the other case, at height of 1.00 meter, where after the increase of the vertical velocity in the second half of the measurement period mostly stable results are obtained. These results prove in another sense the dynamics of the velocity at specific locations.

In order to present the zones at which the velocity experiences fluctuations in time in global aspect, contour plots are made on figure 7.56. The difference with figure 7.54 is that the evaluation of the results is done for every 1000 samples from the data set of 15 000 samples. This results in 15 average velocities, used to determine the standard deviation. In this way the velocity differences (fluctuations) in terms of time are better emphasized.

From figure 7.56 can be stated that the fluctuations are mostly concentrated at the boundary layers. In Exp. 1 (Baseline experiment) in the core of the cavity fluctuations are noticed only in the upper part. For the lower part the time dependent differences are close to zero, which is a good sign for uniform flow at the inlet. Comparing with the two other cases can be observed an increase of the fluctuations in the core of the cavity in direction towards the inlet. The same conclusion was made for figure 7.54 . Additionally it should be stated that the fluctuations are given as an absolute value.

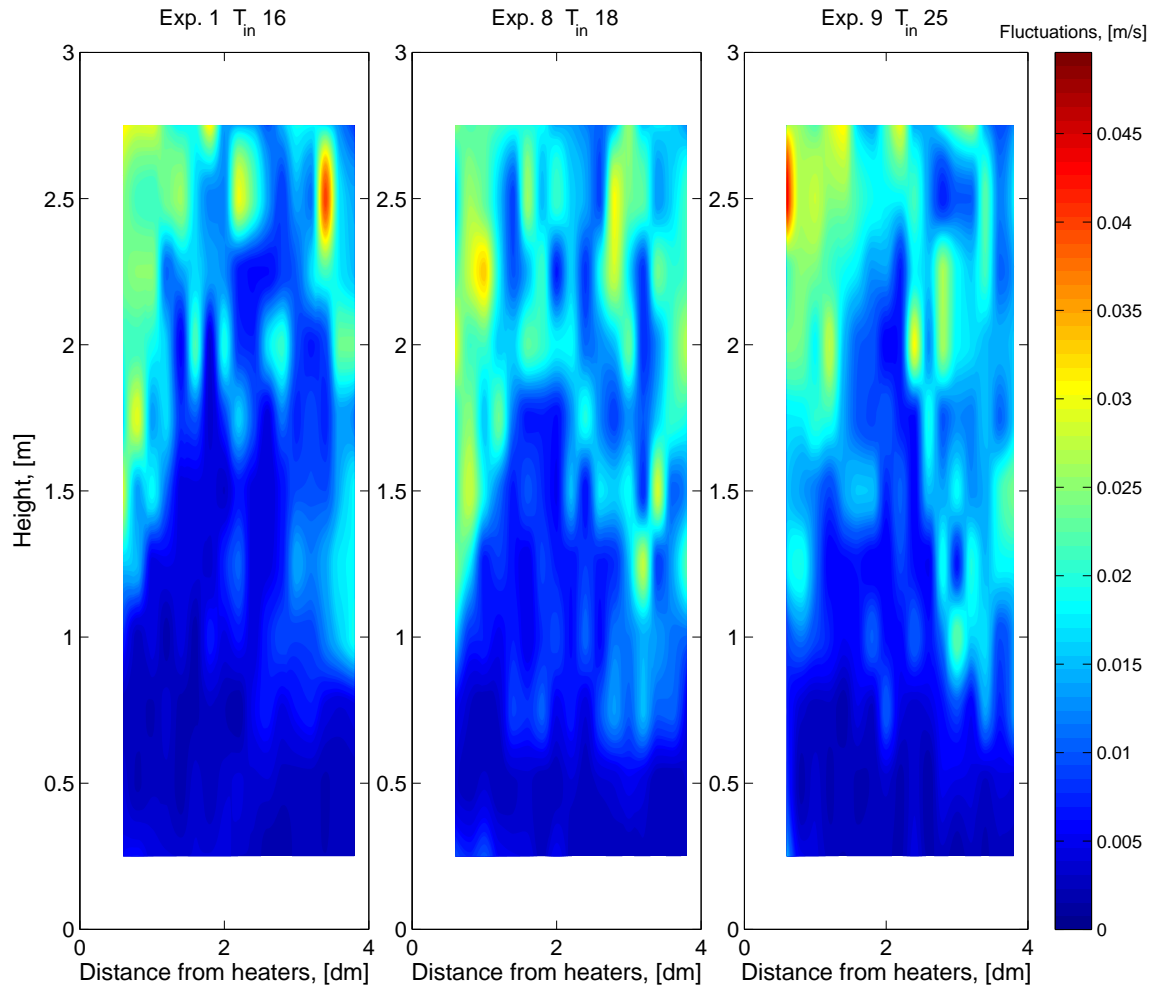


Figure 7.56. Velocity fluctuations in time for (Group 3)

Since the fluctuating zones are estimated, it is relevant to focus on the turbulence levels inside the cavity. The contour plots showing the turbulence are presented on figure 7.57. First of all, all experiments are scaled with the same color bar, so the comparison is easier. Secondly, the limits of the color bar are regarding the minimal and maximal value from all cases, so zero values are not present. Normally regions with turbulence level close to zero are assumed as laminar or partly transient, however in this case all values are much higher. All cases show intensive turbulence at the inlet region (first two levels). Additionally, with increase of the inlet temperature the turbulence above first two levels increases until it fills the whole cavity in Exp. 9. An interesting observation is that the most of the turbulence results are situated in a smaller range between approximately 0.055 to 0.07 m/s for the last two cases. By all means it looks that the flow is turbulent inside the cavity. For the final statement will be concluded based on the dimensionless analysis in the next subsection.

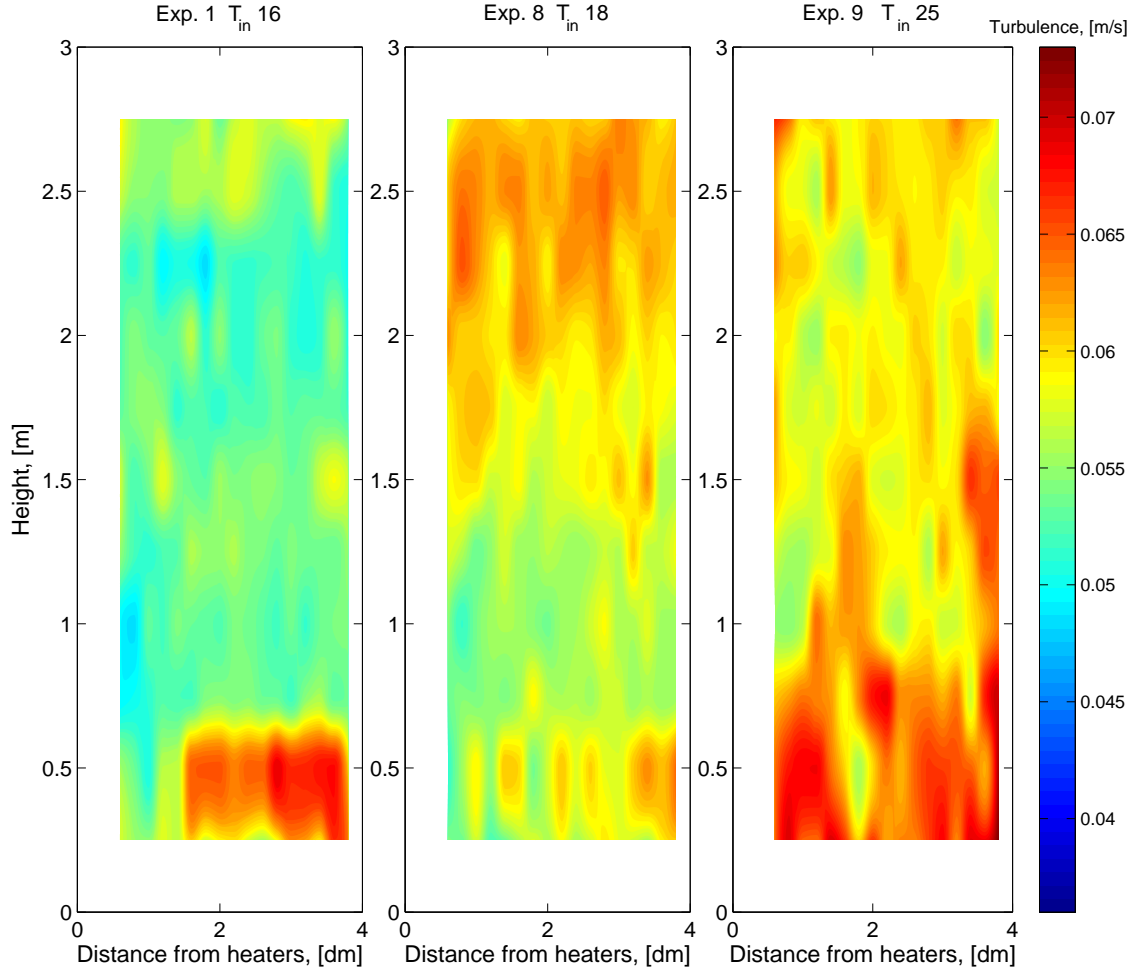


Figure 7.57. Turbulence levels (Group 3)

7.4.3 Dimensionless analysis

All calculated dimensionless numbers are presented in table 7.8.

Table 7.8. Dimensionless numbers for group three

	Exp. 1 (Baseline)		Exp. 8 ($T_{in}18^{\circ}\text{C}$)		Exp. 9 ($T_{in}25^{\circ}\text{C}$)	
	Hot	Cold	Hot	Cold	Hot	Cold
Gr_H	4.86E+10	4.11E+10	4.04E+10	3.37E+10	9.56E+09	4.48E+09
Pr	0.7026	0.7028	0.7024	0.7026	0.7017	0.7018
Gr_H/Re_H^2	1.07E+05	9.07E+04	9.41E+04	7.85E+04	2.39E+04	1.11E+04
Ra_H	3.41E+10	2.88E+10	2.84E+10	2.37E+10	6.77E+09	3.14E+09
Re_H	673		655		636	
Velocity cross section, [m/s]	0.0034		0.0033		0.0033	

Since the Grashof number is a function of the surface and bulk temperatures it is expected that it decreases with increase of the inlet temperature, due to decreased temperature

difference. The Prandtl number is almost constant because of the slight changes in the thermal properties of the fluid in this temperature range.

The parameter evaluating the convection regime is Gr_H/Re_H^2 and by default values way above one describe free convection flow regime. Additionally, the Rayleigh number should be above 10^9 in order to assume a turbulent flow. In all cases the requirement for minimal Rayleigh number is satisfied, so the flow is turbulent. To summarize, the flow in the three cases is free convection turbulent flow.

7.5 Summary of experimental results

The employed theory about separate boundary layers at each surface, based on Incropera et al. [2011], is seen in different magnitude throughout the experimental work. In all experiments is observed a boundary layer development at the surfaces, but based on the different conditions the strength and thickness of the boundary layers are varying. Global recirculation phenomenon is present in almost all cases. However, the theory shown on figure 5.2 on page 32 is not observed in full power during the experiments. The results show lack of flow connection between the boundary layers at the lower part of the cavity. It is assumed that the supply air disturbs the formation of this connection, due to the velocities magnitude in this zone.

The baseline experiment serves as a reference point for all cases. Several runs of the baseline case are done, in order to study the stability of the flow in the cavity. Even though the boundary conditions for the four cases are very similar, regions with flow variations are outlined. The edges of the boundary layers, and the upper part of the cavity show diverse velocity directions and magnitudes. Moreover, inconsistent results for the vectors magnitude are observed also in the boundary layers, which is a sign for turbulence. In terms of temperatures no major differences or instabilities with time are observed for the baseline cases after the upgrade to PID control of the heaters. In general comparing all cases with baseline boundary conditions, can be observed a consistent height of cold boundary layer termination planes and uniform thermal fields. Since the flow inside the cavity is assumed turbulent free convection the diversity of magnitudes and directions in the given zones serve as a prove for this statement.

The first controllable variable is the ACH, which shows the influence of the velocities on the recirculation phenomenon. It is seen that the increase of volumetric flow negates the effects of buoyancy, therefore decreases the boundary layers thicknesses and strength. Less uncertainties are present at the edges of the boundary layers and at the upper part of the facade with the increased air-change rate. These results give the idea of the boundary layers dependency by the strength of the forced airflow. Furthermore, the cold boundary layer termination plane rises up with the increase of ACH. Based on that a conclusion can be derived for the limits of recirculation existence inside the cavity. The lower the ACH is the stronger the cold boundary layer develops and penetrates further towards the inlet opening. It could be assumed that ACH lower than 3 will cover the whole cold glass surface with downwards boundary layer. On the other hand the upper limit of recirculation existence inside the cavity is slightly higher than ACH 12. Further increase of ACH will prevent conditions for downwards flow and promote development of stronger

upwards boundary layer along the glass surface.

The second controllable variable is the hot surface temperature, which brings information about the strength of the boundary layers. The variation of this parameter results in temperature differences between the hot surface and the inlet air of 10°C (Exp. 5), 19°C (Exp. 6) and 22°C (Exp. 7). The case with low surface temperature proved that the air movement is generated mainly by the buoyancy forces and when the air in the cavity reaches the hot surface temperature stagnation is caused. This results in inappropriate ventilation and causes overheating of the facade. However, even a small temperature difference between the surfaces increases the boundary layer strength and promotes the natural convection as in the baseline experiment (Exp. 1). The increase in the hot surface temperature shows higher velocities accompanied with earlier development of the hot boundary layers. The inertial forces due to the higher velocities assist a stronger formation of the cold boundary layer, allowing it to increase its length along the cold surface. In conclusion can be stated that the increase of hot surface temperature favors the development of both boundary layers enforced by the rise in velocity magnitudes. On the other hand, a decrease of the parameter results in no driving forces and consequently in flow stagnation and ensured overheating of the gap.

The last controllable entity in the experimental setup is the inlet air temperature. The general velocity limits are not so different with the increase of inlet temperature. However, the hot boundary layer thickness increases slightly and the flow patterns show formation of different structures compared to the previous experiments. The supply of higher inlet air temperature seems to force an early hot boundary layer development, due to the close temperatures with the hot surface. Additionally it is noticed an increase of the mixing region due to the different flow patterns in the hot boundary layer. These processes have favorable influence on the cold surface boundary layer thickness. As a result a stronger and thicker cold boundary layer is generated, together with more fluctuations at its edge. This implies that the conditions assisting recirculation are not necessary a bigger difference between the inlet air and the surface temperatures. However a cold temperature supply will decrease the flow inertia and consequently the recirculation ability, while the opposite might result in stronger recirculating phenomena.

The calculation of dimensionless numbers in all cases confirms the turbulent free convection flow. The characteristic dimension for all of the calculations is assumed the height of the cavity, based on the general flow direction. In none of the cases is derived a value for Rayleigh number lower than $1 \cdot 10^9$, which is the threshold for turbulent flow regime. The values obtained for Rayleigh number at the cold and hot surfaces are presented on figure 7.58. Since Rayleigh number is a multiplication of Grashof and Prandtl, the temperature is the leading variable in the calculation process.

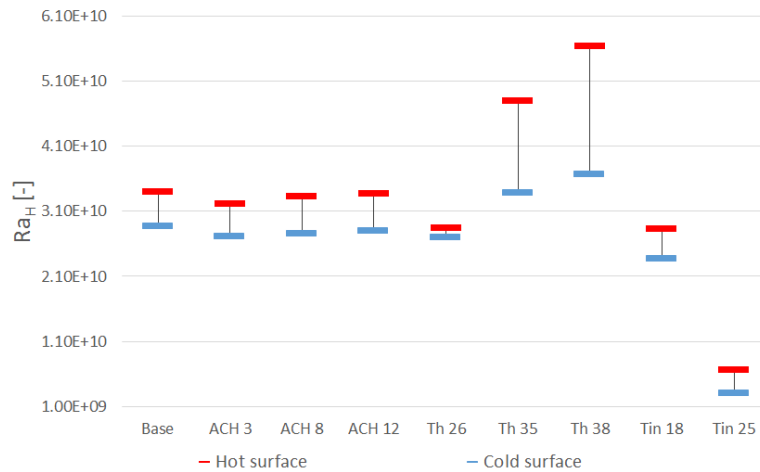


Figure 7.58. Rayleigh number ranges for all experiments

The ratio Gr/Re^2 , which is used to determine the convection regime is much higher than 1 in all cases. Therefore, to give an overview of the range of its variations is presented figure 7.59. As expected, the experiments with higher buoyancy forces are located in the upper part of the figure, while the one with high ACH are positioned in the lower part. The figure clearly states that in order to assist the buoyancy forces is necessary lower ACH and increased hot surface temperature.

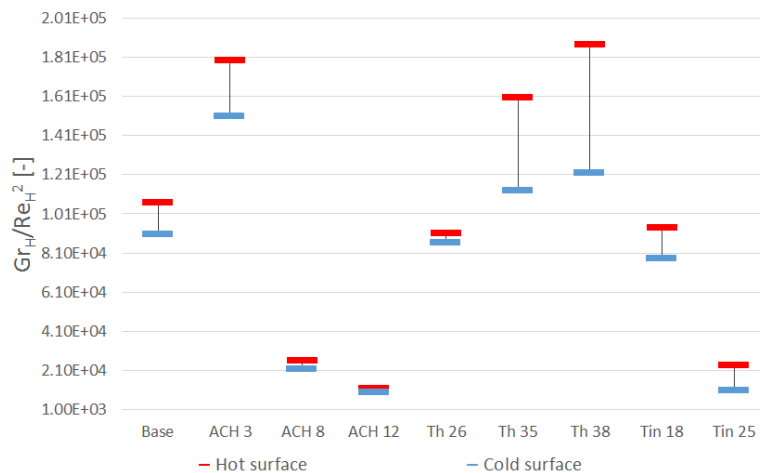


Figure 7.59. Gr_H/Re_H^2 ranges for all experiments

To summarize all concluded above statements, a stronger presence of global flow recirculation inside an asymmetrically heated, non-convergent, vertical channel occurs when the setup is exposed on low inlet velocities (low ACH), high temperature difference between the surfaces and warmer inlet air supply.

In order to present an overview of the assumed flow pattern inside the cavity is derived general flow movement sketch on figure 7.60. The key processes are located inside the boundary layers and in the core of the cavity. What brings attention to the hot boundary

layer is the formation of eddies at its edge with unpredictable manner. The vortexes have various magnitude and appears along the whole boundary layer. Since the direction of the eddies is towards the core of the cavity, they are entrained and their structure is stretched due to high velocity difference caused by the vortex momentum and core flow.

In the middle of the cavity the velocity vectors are rather constant in direction and small in magnitude, compared to the boundary layer velocities. This core zone is necessary for the proper transition from upwards to downwards flow direction. Its main purpose is to supply the boundary layers with fresh air and in this way assures their proper development.

Moving toward the cold surface the flow experiences transition in downwards direction by being entrained into the cold boundary layer. Depending on the exposed conditions the thickness of the cold boundary layer can vary significantly and the vectors which feature its feeding can experience major decrease and become invisible in some experimental cases. Additionally, the uniform flow direction shift when reaching the cold boundary layer is not properly caught during the measurement process. However, various studies of flow collision with similar conditions to the current case state that the most probable way of reaction between the opposing flows is as presented on figure 7.60.

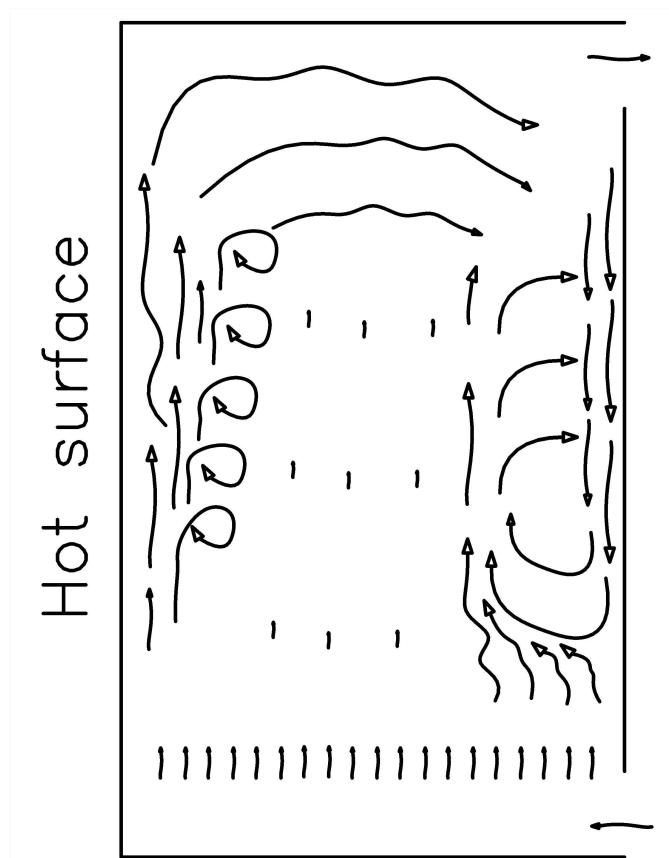


Figure 7.60. Flow recirculation and eddies formation

Part III

Conclusion and discussion

In this part are presented the conclusions derived from the experimental analyses, together with the limitations of the current setup. Suggestions for future work over the topic of flow behavior in DSF is also included.

Limitations 8

The project work is performed over an experimental setup, where as with every experiment, uncertainties and limitations are established. The following section summarizes them, in order to appreciate their influence over the experimental results.

Starting with the controlling equipment, the heaters controller, which is mentioned several times during the analysis, is upgraded from On/Off to PID (Proportional-Integral-Derivative). However, despite the obvious improvement consisting of stable maintenance of temperature, the controller step is still too coarse (1°C) for the purpose of the project. A more acceptable controlling strategy is the utilization of the floating gain controller for the cooling machine, where the control step is 0.1°C . An improvement of the control equipment can be considered a decrease of the set step for the heaters controller to (0.1°C).

Other generated uncertainties are due to the fan supplied inlet volumetric flow. The cooling equipment and the fog generator need higher flow rates for the proper heat extraction, while the desire for free convection dominant flow contradicts with that. This creates the necessity to exhaust a significant part of the conditioned air away from the experimental setup and outside of the laboratory, where the wind forces might oppose the extraction and influence the overall pressure distribution in the ductwork. Based on the results from the pressure difference at the orifice plate, is calculated that the variation in the volumetric flow reaches up to 19% for Exp.2 (ACH 3). These uncertainties can be avoided, if the construction of the experimental setup is refurbished. In the work of Sanchez et al. [2007], which is based on open joint ventilated facades, is used an attached construction to the inlet opening, which contains the preconditioned air. In that way with the additional enclosure, the inlet air is treated to the proper temperature and seeding particle density, while simultaneously maintaining stable pressure. With this construction only the buoyancy forces will be responsible for the air movement inside the cavity and will be avoided uncertainty caused by forced airflow.

Taking into account the velocity measurement system, a good precision is achieved in terms of averaged local velocities. The Laser-Doppler Anemometer (LDA), produced a Gaussian distribution, with validation of above 99%, for each measurement point in horizontal and vertical direction. However, the LDA system measures only 1D particles displacement. Therefore for the horizontal and vertical measurement is necessary a rotation of the probe. The lack of traverse system requires a manual rotation of the probe for each point. Despite the effort for alignment in all measurements the process can not be regarded as absolutely

precise. The manual rotation and alignment for each point generates an inestimable error and uncertainties due to the human factor. Additionally, for the top levels in the cavity the manual rotation requires a person standing close to the exhaust opening. The presence of a breathing and moving person in this region can be a cause of exhaust flow distortion. Local draught and currents in the laboratory are as well a prerequisite for flow instabilities at the exhaust.

Another accepted limitation is that the time acquisition for a single point took approximately 1 to 2 minutes. This prevents the capturing of flow variations (eddies), which require simultaneous measurement in more than one location. Therefore, it is not possible to create a velocity map of the cavity based on the instantaneous velocities, so the analysis is done based on averaged values. An improvement could be an implementation of a two-dimensional (2D) LDA system, with traverse mechanism, which will exclude the alignment problem and will provide coherent and simultaneous results acquisition in a 2D plane for a given point. Even better precision can be achieved by utilization of a Photo-Image Velocimetry (PIV) system. With a PIV system simultaneous acquisition of 2D velocities for a certain array of the cavity can be easily obtained. This will increase the precision of the measurements by allowing acquirement of data for the dynamic flow patterns in the cavity.

The listed above limitations are admitted, and an effort to overcome them by creating well planned and systematic experimental procedure and consecutive analysis is done. The procedure is resembling a One Factor At a Time analysis, where possible variations of the temperature and flow rate are tested.

Proposals for further work 9

The topic regarding flow nature in asymmetrically heated, vertical channel can not be depleted in the limits of this report. Further improvement can always be made and more precise experiments can be performed. However, authors' experience and proposals can be used as a base for further studies.

As mentioned earlier, the setup can be significantly improved in terms of geometry and equipment. Special attention should be paid to inlet structural improvements, so the conditions are as close as possible to free convection turbulent flow. In addition, the ability to control the temperature at both surfaces of the cavity will definitely expand the range of possible experiments and help to confirm the limits of recirculation flow more precisely. Furthermore, the equipment potential to reach broader inlet temperature range than the one already used should be increased. A preheating of the supply air will be an advantage for the future experimental setup. More experiment are proposed with high inlet air temperature, which is assumed to assist the conditions for global recirculation.

Another experiment that is not performed due to setup limitations is to observe the flow, when the cavity ACH is decreased under 3. This case might have the key for explaining why in the experiments presented above the recirculation is not the same as on figure 5.2 on page 32. Additionally, can be performed as well an experiment with increase of heaters surface temperature higher than 38°C. This might enforce the buoyancy forces and increase the flow momentum. Moreover, the experimental cases can be enriched by a variation of the facade thickness. Since the task is to develop an overall performance characteristics, it is expected that the various cavity thicknesses will contribute to the understanding of the flow pattern.

An improvement which will allow generation of various analyses is the increase of the velocity measurement area to cover the first 6cm close to the heated surface. This area is not investigated in the report due to setup limitations, but an alternation of the cavity structure can solve the problem. An acquisition of the velocities close to the heated surface will fill the missing data in the current report and allow a performance of mass flow analysis. Also, it can be beneficial to confirm the claim for 2D flow by a PIV measurement of velocities at the cavity cross section.

Additionally, it is worth measuring the inlet and outlet flow velocities together with the internal flow at the same level. They can present valuable information about the flow

patterns. The acquired data can be used for mass flow analysis through the openings.

The current project contains only experimental results and analyses. These can be used for validation of CFD simulation for prediction of the flow patterns between the asymmetrically heated vertical plates. Therefore, a development of a CFD model will be an useful improvement for a creation of an overall assessment of the physical processes in the gap.

Conclusion 10

The topic of flow nature inside asymmetrically heated, non-convergent, vertical channel was investigated in the current project. The simulated flow regime was turbulent free convection, driven by the temperature differences in the cavity. The project was focused on experimental measurements of velocities magnitude and direction, and temperatures in a two dimensional vertical plane between the asymmetrically heated plates. Velocities were measured with LDA system and temperatures with type K thermocouples. The experimental setup consisted of a glass surface exposed to laboratory conditions and a heated surface. The channel had two openings at the top and bottom of the glass surface, which served the role of inlet and exhaust. The inlet air was treated to the desired temperature, mixed with smoke particles and supplied with controlled velocity inside the cavity.

The outcome of the obtained data is an understanding of the flow dependency between the plates on the temperatures and inlet volumetric flow rate. The results are summarized in graphs showing the averaged temperature and velocity distribution for the entire vertical 2D cross plane of the cavity. The analysis of the velocity data include turbulence, stability of the flow and fluctuations throughout the measurement period. The analysis of the temperature data contains horizontal, vertical temperature distribution and contour plots.

Based on the results are derived the approximate boundaries of the recirculation pattern existence. It was concluded that even with fan forced inlet flow recirculation is present up to the threshold of 12 ACH, where the pattern was displaced upwards and an development of standard channel flow was observed. On the other hand, experiments with lower ACH present suitable conditions for establishment of stronger recirculation phenomenon. The temperature variations showed that higher temperatures of the hot surface facilitate the buoyancy and due to the generated stronger momentum forces influence the downwards cold boundary layer by increasing its strength. Moreover, the raise of inlet air temperature revealed that even with small temperature difference between the hot surface and the inlet temperature a recirculation phenomena is present. The increase resulted in slightly stronger hot boundary layer with unstable velocities at its edge and as a consequence has developed a thicker cold boundary layer.

In conclusion can be said that the experimental work can be regarded as successful in establishing dependencies of the varied parameters and the existence of the recirculation phenomena. However, further development of the topic in combination with computer simulations is necessary for the improved description of the problem.

Bibliography

- Artmann, N., Vonbank, R. and Jensen, R. [2008], Temperature measurements using type k thermocouples and the fluke helios plus 2287a data logger, Technical report.
- Ayinde, T. F., Said, S. and Habib, M. [2007], ‘Turbulent natural convection flow in a vertical channel with anti-symmetric heating’.
- Badr, H., Habib, M., Anwar, S., Ben-Bansour, R. and Said, S. [2006], ‘Turbulent natural convection in vertical parallel-plate channels’.
- Crespo, A. [1999], ‘History of double skin facades’.
- Dantec-Dynamics [2002], *BSA Flow Software - Installation and User’s guide*.
- Dantec-Dynamics [2016], ‘Principle of lda’.
URL: <http://www.dantecdynamics.com/measurement-principles-of-lda>
- Desrayaud, G. and Lauriat, G. [2009], ‘Flow reversal of laminar mixed convection in the entry region of symmetrically heated vertical plate channels’.
- Eckert, E. and Jackson, T. [1951], Analysis of turbulent free-convection boundary layer on flat plate, Technical report.
- Fedorov, A. and Viskanta, R. [1997], ‘Turbulent natural convection heat transfer in an asymmetrically heated, vertical parallel-plate channel’.
- Habib, M., Said, S., Ahmed, S. and Asghar, A. [2002], ‘Velocity characteristics of turbulent natural convection in symmetrically and asymmetrically heated vertical channels’.
- Incropera, Bergman, DeWitt and Lavine [2011], *Fundamentals of Heat and Mass Transfer*, number ISBN 13 978-0470-50197-9 in ‘7th edition’, John Wiley and Sons.
- Larsen, O. K. [2008], ‘Double-skin facade: Modelling and experimental investigations of thermal performance’.
- Mikkelsen, M. B. [2015], ‘Flow field characteristics in vertical channel with one heated surface’.
- Miyamoto, M., Katoh, Y., Kurima, J. and Saki, H. [1986], *Turbulent free convection heat transfer from vertical parallel plates*.
- Oesterle, Lieb, L. H. [2001], *Double-Skin Facades - Integrated planning*.

Plexiglas - general information and physical properties [2016].

URL: <http://www.plexiglas.com>

Poirazis, H. [2004], Double skin facades for office buildings - literature review, Technical report, Lund University.

Rusev, D., Chakarova, D., Gospodinova, M. and Pavlova, I. [2002], *Heat transfer*.

Saelens, D. [2002], Energy performance Assessments of Single Storey Multiple-Skin Facades., PhD thesis, Catholic University of Leuven, Belgium.

Sanchez, M., Sanjuan, C., Suarez, M. and Heras, M. [2007], 'Experimental assessment of the performance of open joint ventilated facades with buoyancy-driven airflow'.

Skistad, H., Mundt, E., Nielsen, P., Hagstrom, K. and Railio, J. [2004], *Displacement ventilation in non-industrial premises*, number ISBN 82-594-2369-3, REHVA - Federation of European Heating and Air-conditioning Associations.

Yilmaz, T. and Fraser, S. [2007], 'Turbulent natural convection in a vertical parallel-plate channel with asymmetric heating'.

Yilmaz, T. and Gilchrist, A. [2007], 'Temperature and velocity field characteristics of turbulent natural convection in a vertical parallel-plate channel with asymmetric heating'.

Zollner, A., Winter, E. and Viskanta, R. [2002], 'Experimental studies of combined heat transfer in turbulent mixed convection fluid flows in double-skin-facades'.

Part IV

Appendix

Here are summarized explanations and data which are not included in the main body of the project, but are referred in it.

Temperature Measurements A

A.1 Thermocouples and PT100 Sensors Calibration

A proper measurements with thermocouples and PT100 sensors require a calibration, which improves the accuracy of the data to 0.086K for type K thin thermocouples and 0.05K for PT100 sensors. The thin thermocouples are used for air temperature measurements inside the cavity, while PT100 sensors are used to follow the temperature variation of the compensation box.

The following list of equipment is used:

- Fluke Helios Plus 2287 A Data logger
- Ice point reference KAYE K170-6
- ISOCAL-6 VENUS 2140B Plus
- F200 Precision Thermometer
- Computer with Lab View

The first step of the calibration process is to calibrate the three PT 100 sensors, which will give the temperature of the Compensation box. The set up is schematically visualized on figure A.1.

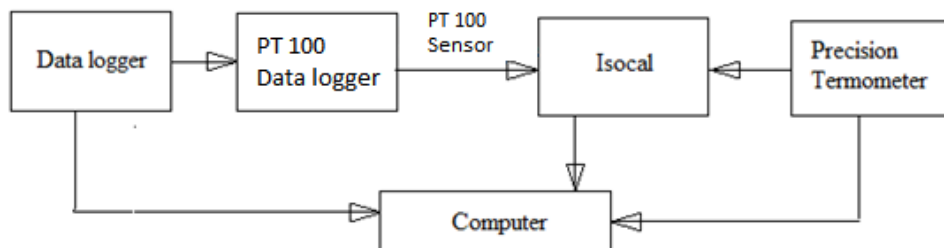


Figure A.1. Set up for calibration of PT 100 sensors

The equipment is properly grounded and the calibration is performed on 11 steps from 0° C to 100° C. It is assumed that bigger range for the calibration of the reference

thermocouples is unnecessary, because the laboratory temperature is maintained between $20 - 25^{\circ} C$.

For the air measurements inside the experimental box are used 97 thin type K thermocouples, which are calibrated on 10 steps for the range of $5^{\circ} C$ to $50^{\circ} C$. Figure A.2 presents a scheme of the set up. Additionally, the PT 100 sensors are positioned on equal distances along the length of the compensation box.

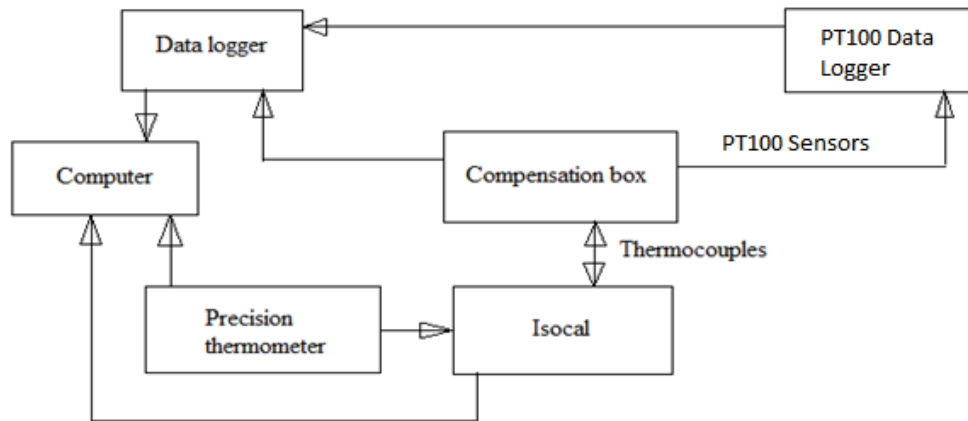


Figure A.2. Set up for calibration of thermocouples

A.2 Thermocouples location

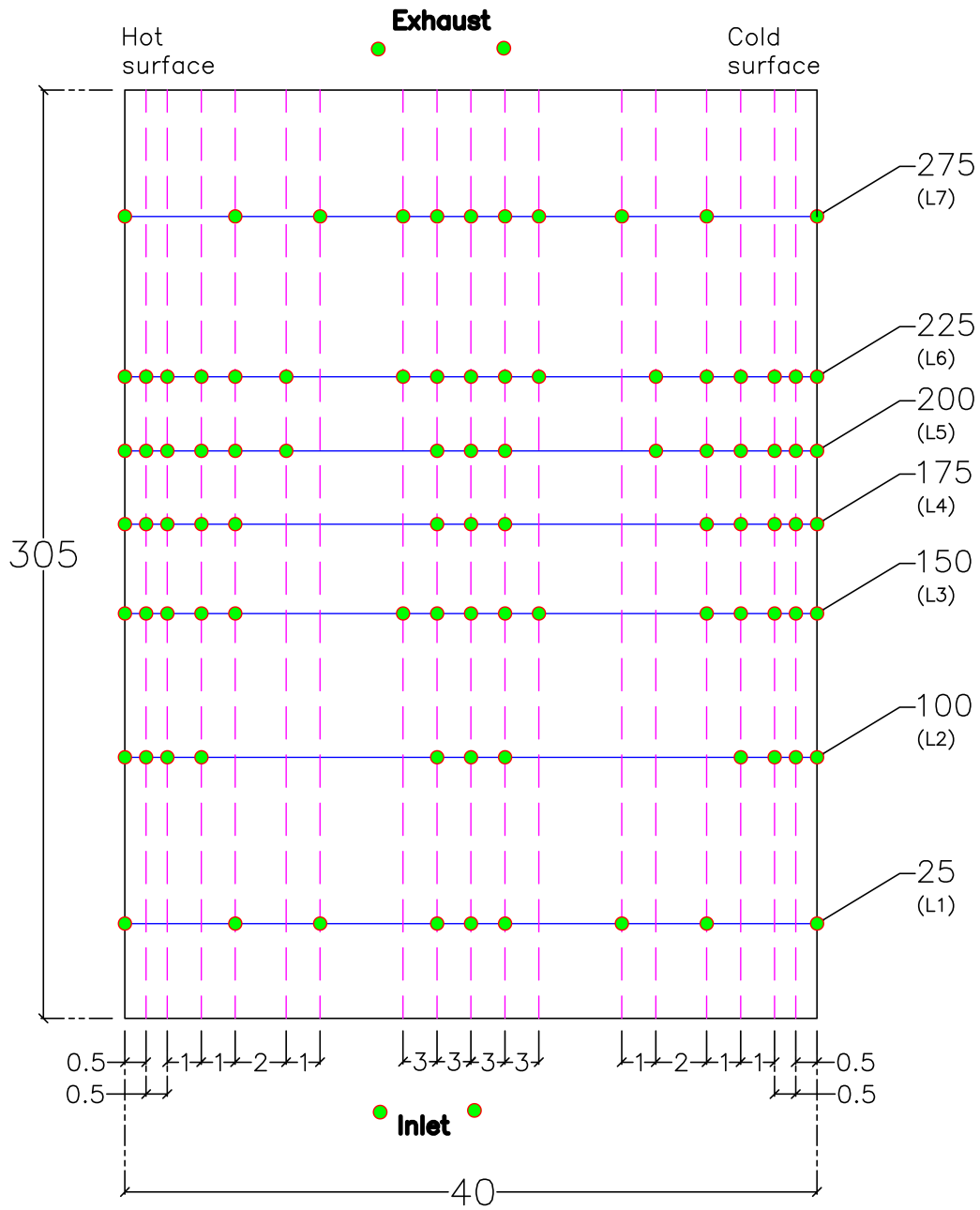


Figure A.3. Position of thermocouples inside the experimental box; dimensions are in cm

Velocity Measurements characteristics

B

B.1 Laser Doppler Anemometry Performance Principle

The following section is based on Dantec-Dynamics [2016].

A widely accepted tool for fluid dynamics investigations in fluids is the Laser Doppler Anemometer (LDA). It gives information about the flow velocity and direction and is suitable for applications with reversing flow, chemically reacting or high-temperature media and rotating machinery, where physical sensors are difficult or impossible to use. The measuring process requires a tracer particles within the flow. The method's particular advantages are: non-intrusive measurement, high spatial and temporal resolution, no need for calibration and the ability to measure in reversing flows. A basic configuration of a LDA is presented on figure B.1.

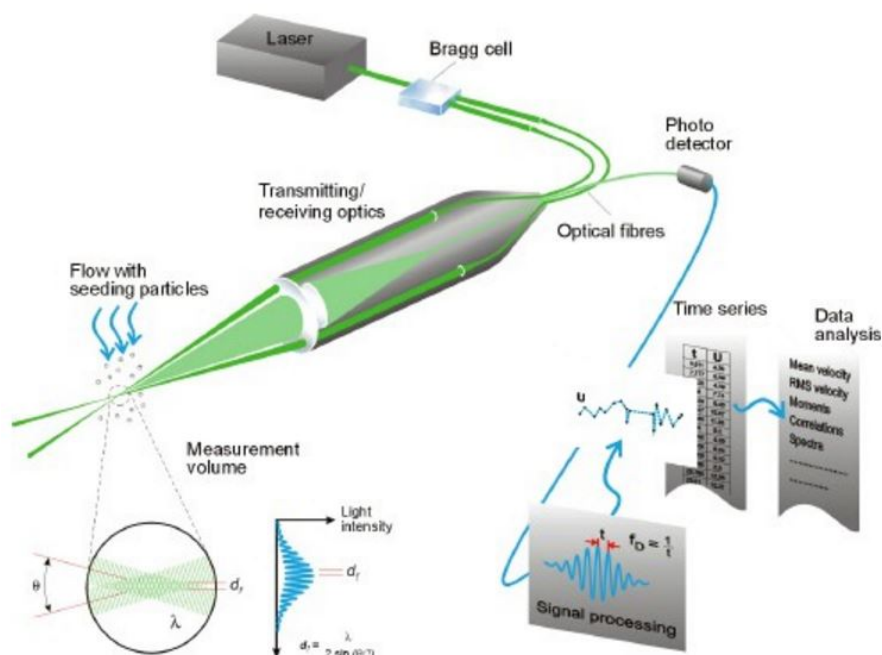


Figure B.1. Basic configuration of an LDA

An important part of an LDA system is the laser. It is a continuous wave laser, which works with a specific wave length. The beam goes through a beam splitter, which in this system is the Brag cell. It is a glass crystal with a vibrating piezo crystal attached. The vibration generates acoustical waves acting like an optical grid. As a result two beams of equal intensity with frequencies f_0 and f_{shift} are formed and focused into optical fibers bringing them to a probe.

The probe is the place where the parallel exit beams from the fibers are focused by a lens to intersect in the probe volume (measurement volume). It is typically a few millimeters long, where parallel planes of high light intensity, called fringes, are formed. The fringe distance d_f is defined by the wavelength (λ) of the laser light and the angle (Θ) between the beams:

$$d_f = \frac{\lambda}{2\sin(\Theta/2)} \quad (\text{B.1})$$

When a particle passes through the measuring volume a light proportional to the local light intensity scatters, which gives information about the flow velocity. The scattered light contains a specific Doppler frequency f_D which is converted to an electrical signal (Doppler burst) in the photo-detector. To remove the noise from ambient light and from other wavelengths an interference filter is mounted before the photo-detector. The output is sinusoidal signal with Gaussian envelope due to the intensity profile of the laser beams.

The signal processing is implemented in the signal processor, which determines the Doppler frequency (f_D) for each particle by using usually the robust Fast Fourier Transform algorithm. The Doppler frequency (f_D) provides information about the time for which a particle passes through the measuring volume:

$$t = \frac{1}{f_D} \quad (\text{B.2})$$

The fringe spacing (d_f) provides information about the distance traveled by the particle. As a result the velocity is calculated as distance divided by time:

$$V = d_f * f_D \quad (\text{B.3})$$

To evaluate the direction of the velocity is used the obtained by the Brag cell frequency shift (f_{shift}), which makes the fringe pattern to move at a constant velocity. Particles which are not moving will generate a signal of f_{shift} and particles with velocity V_{pos} and v_{neg} will generate signal frequencies f_{pos} and f_{neg} , respectively.

B.2 Orifice plate regression curve

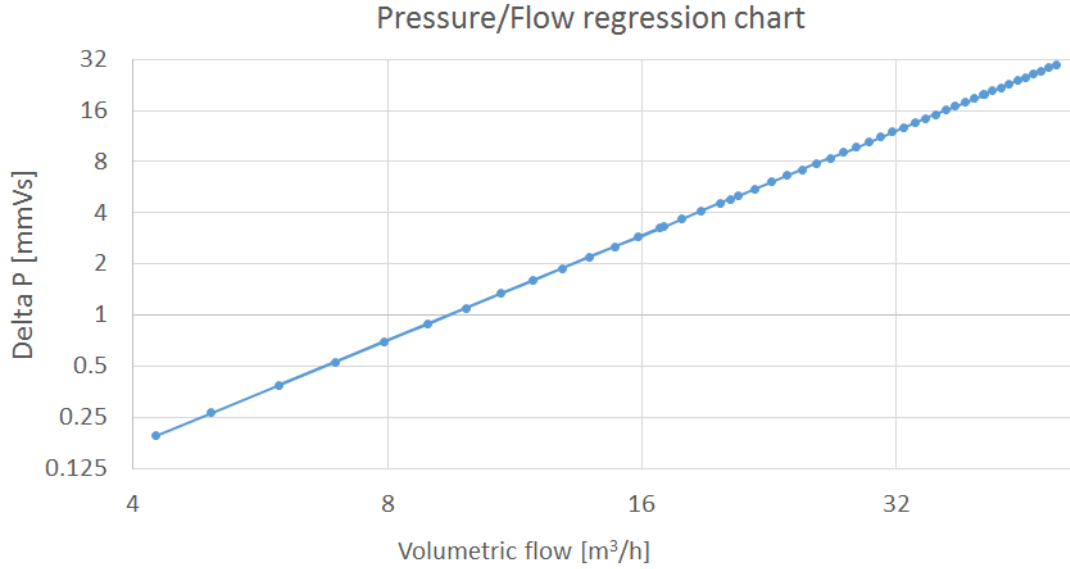


Figure B.2. Regression curve for orifice plate

The regression curve describes the flow variation with change of the pressure difference between both sides of the orifice plate. Both axes are logarithmic. The equations according to which is built the curve are presented below:

$$Q = 9.465 \cdot \Delta P^{0.4879} \quad (\text{B.4})$$

$$\Delta P = 0.00998071 \cdot Q^{2.04977} \quad (\text{B.5})$$

Since the pressure equations are derived for temperature of 20°C, a density correction is applied according to the following equation.

$$Q_{corrected} = Q_{measured} \sqrt{\frac{1.2}{\rho}}, [m^3/h] \quad (\text{B.6})$$

where:

Q	volumetric flow, [m^3/h]
1.2	fluid density at 20°C, [kg/m^3]
ρ	fluid density before the orifice plate, [kg/m^3]
ΔP	Pressure difference at the orifice plate [mmVs]

Experimental setup pictures

C



Figure C.1. Experimental setup(Hot box)



Figure C.2. YZ experimental plane



Figure C.3. LDA probe placement

Experimental results - Air-change rate variation

D

D.1 Temperature distributions

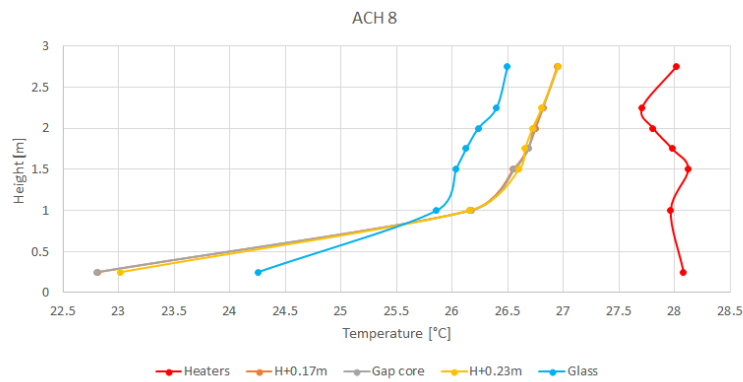


Figure D.1. Vertical temperatures distribution for Exp. 3 (ACH8)

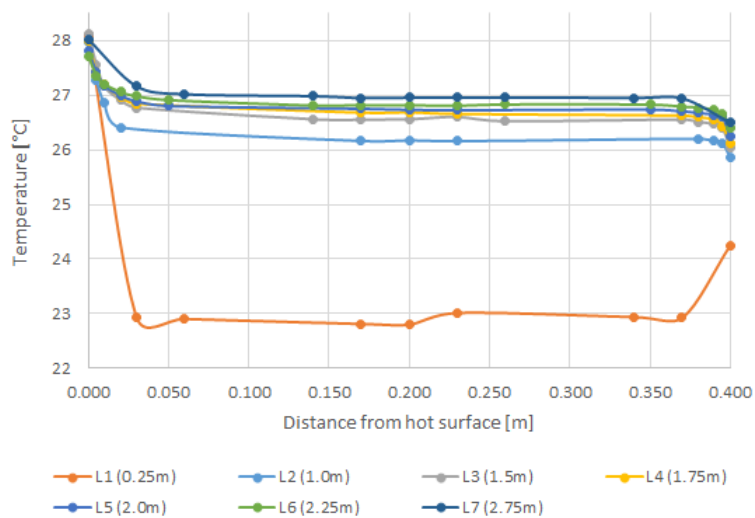


Figure D.2. Horizontal temperatures distribution for Exp. 3 (ACH8)

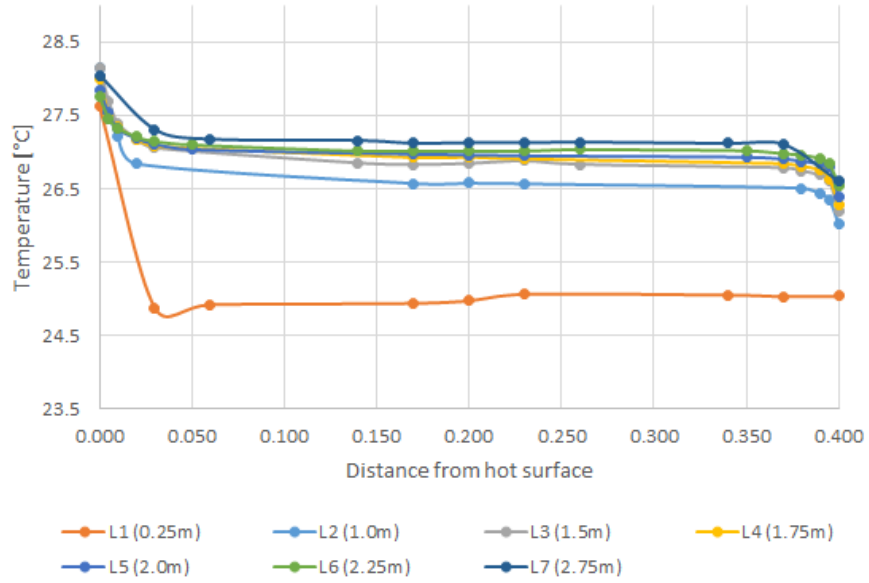


Figure D.3. Horizontal temperatures distribution for Exp. 2 (ACH3)

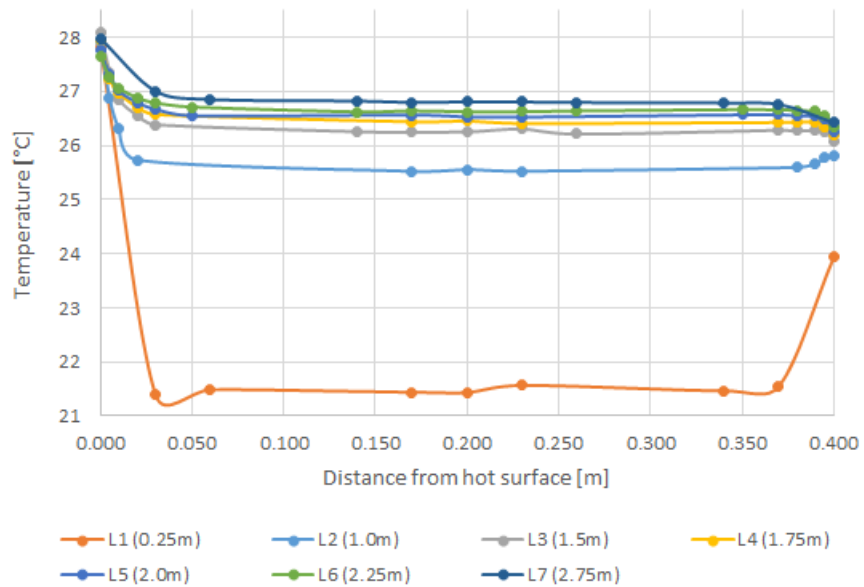


Figure D.4. Horizontal temperatures distribution for Exp. 4 (ACH12)

D.2 Velocities distributions

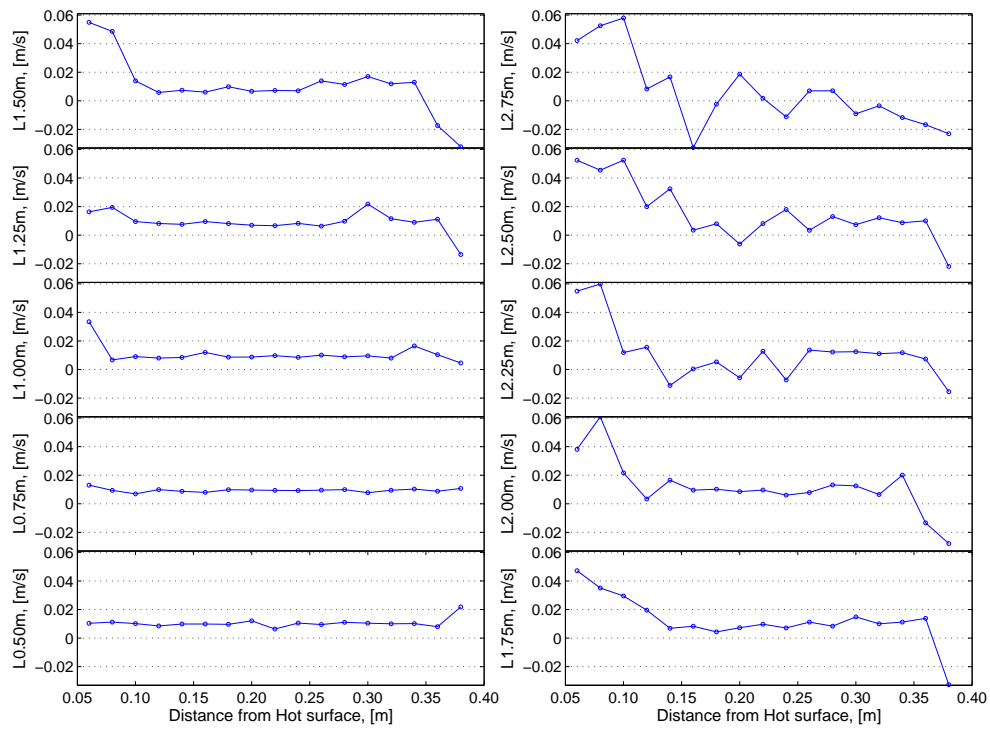


Figure D.5. Experiment 3 (ACH 8) velocity at all levels

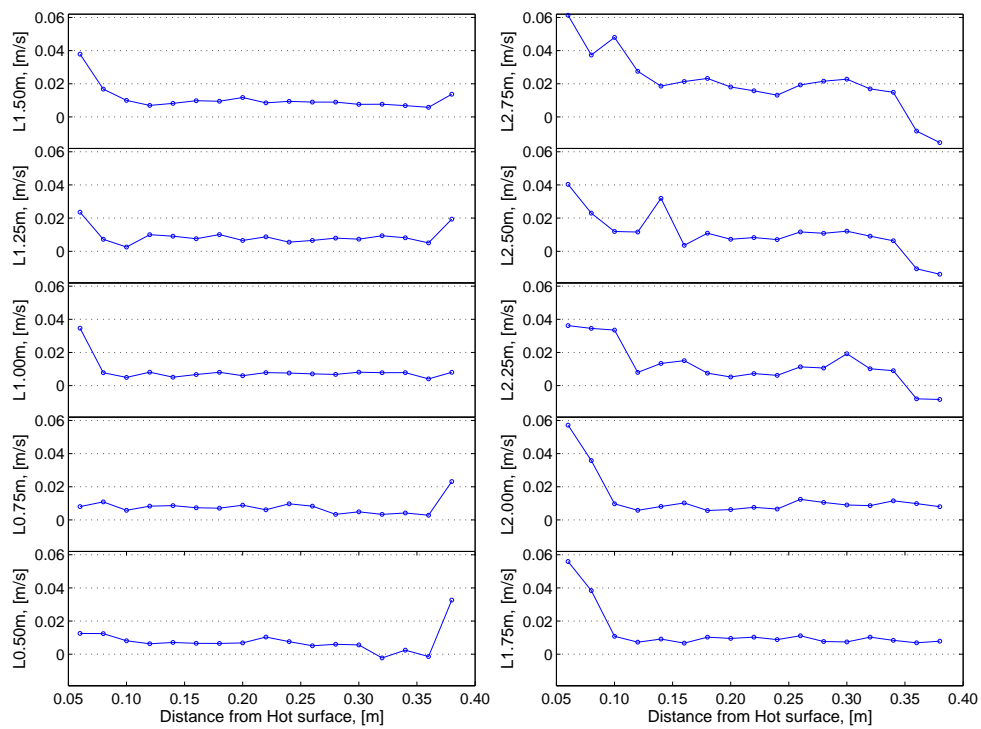


Figure D.6. Experiment 4 (ACH 12) velocity at all levels

D.3 Pressure difference histograms

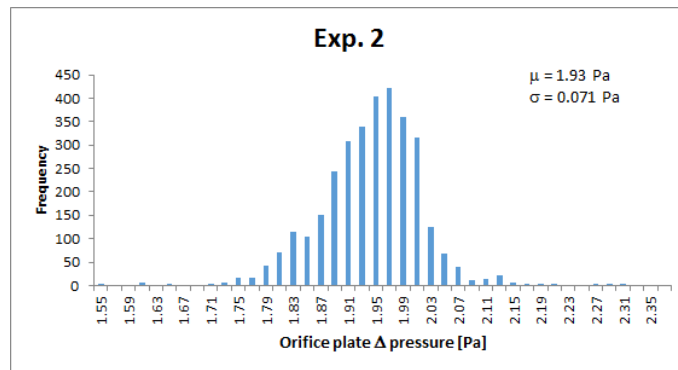


Figure D.7. Orifice pressure difference histogram Exp. 2

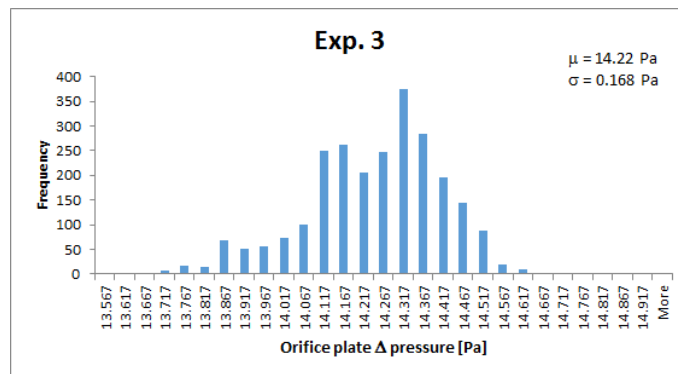


Figure D.8. Orifice pressure difference histogram Exp. 3

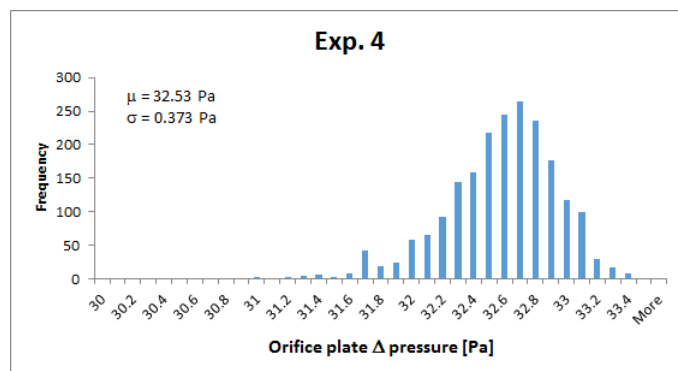


Figure D.9. Orifice pressure difference histogram Exp. 4

Experimental results - Hot surface temperature variation



E.1 Temperature distributions

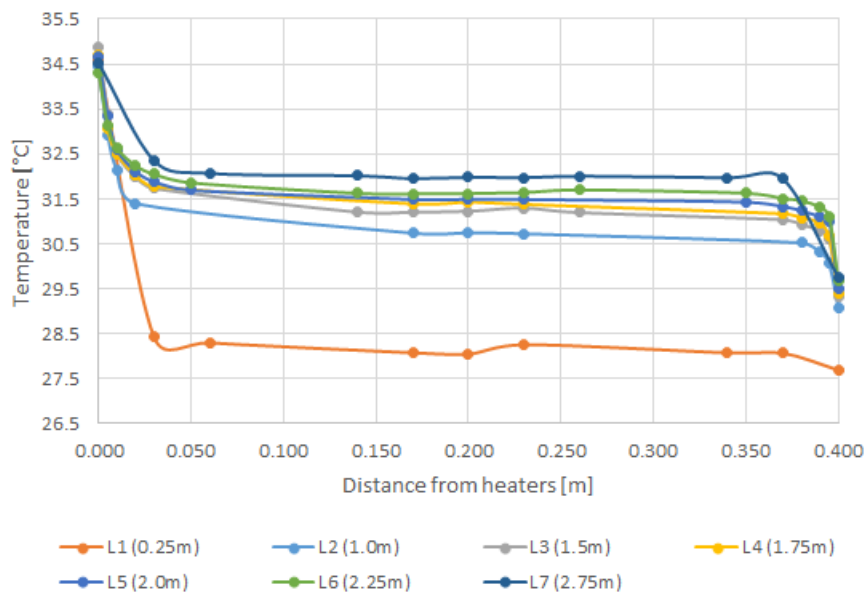


Figure E.1. Horizontal temperatures distribution for Exp. 6 (Hot surface temperature 35°C)

E.2 Velocities distributions

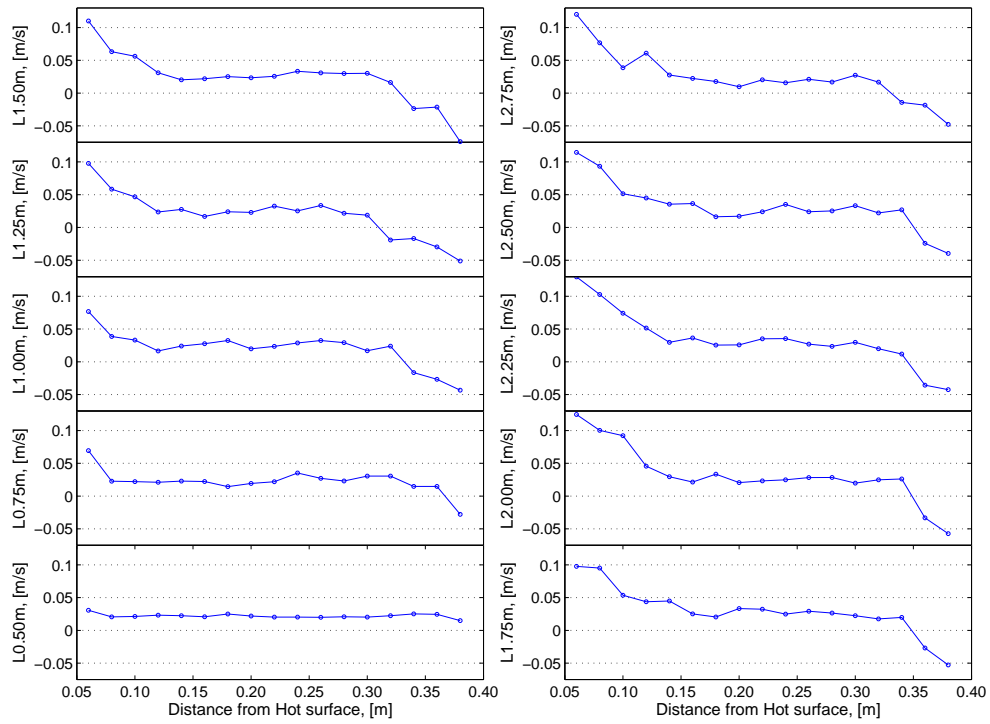


Figure E.2. Velocity distribution with height Exp. 7

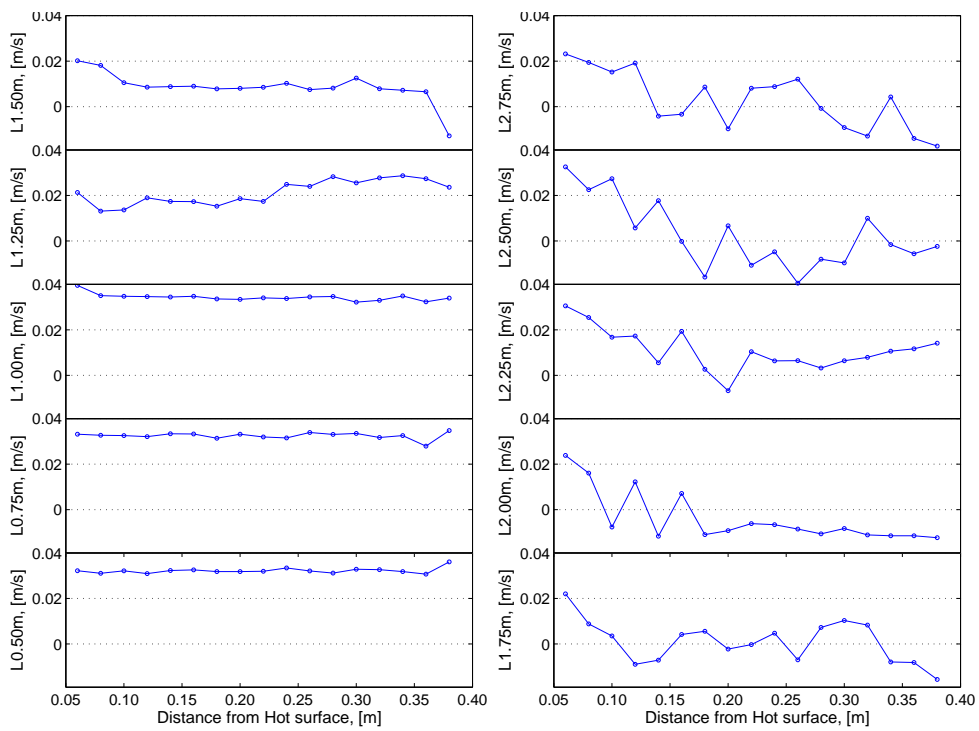


Figure E.3. Velocity distribution with height Exp. 5

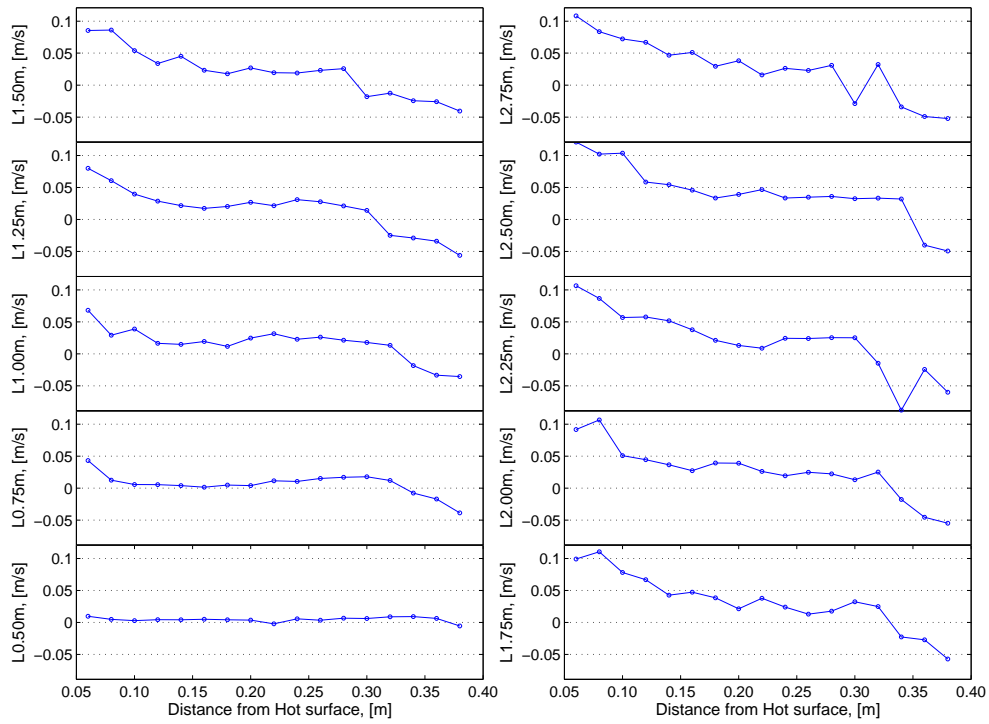


Figure E.4. Velocity distribution with height Exp.6

E.3 Pressure difference

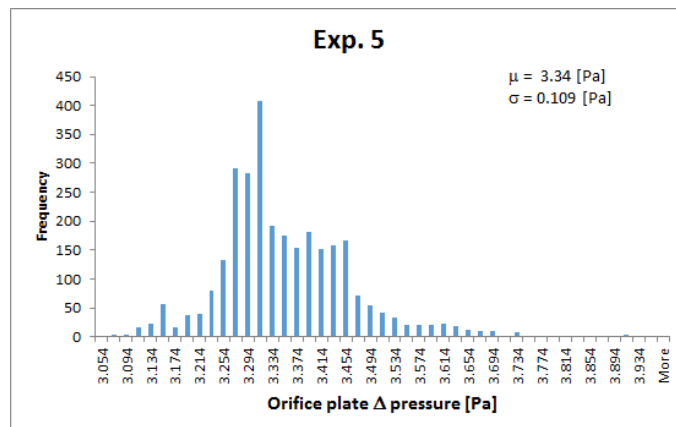


Figure E.5. Orifice pressure difference histogram Exp. 5

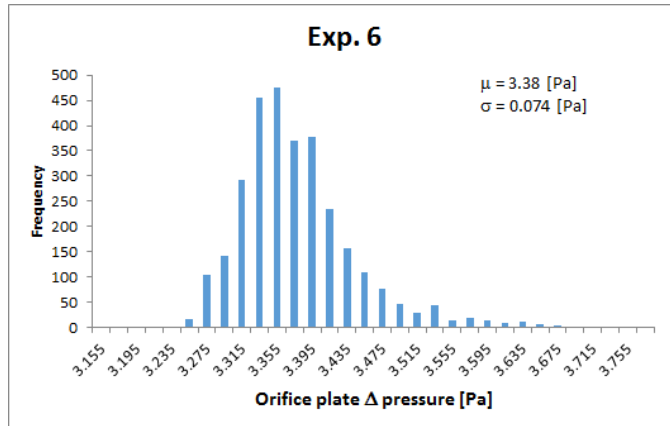


Figure E.6. Orifice pressure difference histogram Exp. 6

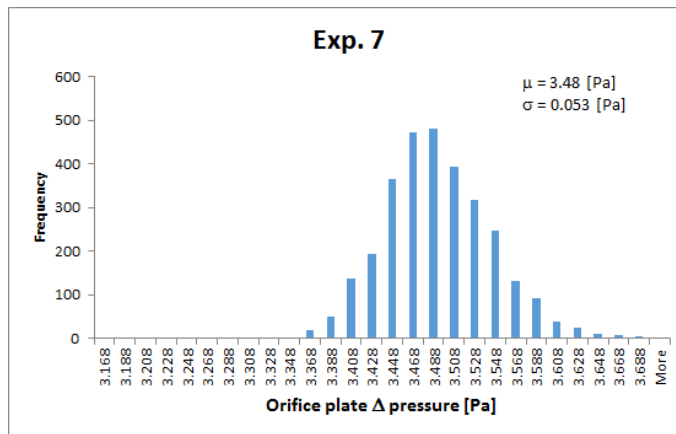


Figure E.7. Orifice pressure difference histogram Exp. 7

Experimental results - Inlet temperature variation

F

F.1 Velocities distributions

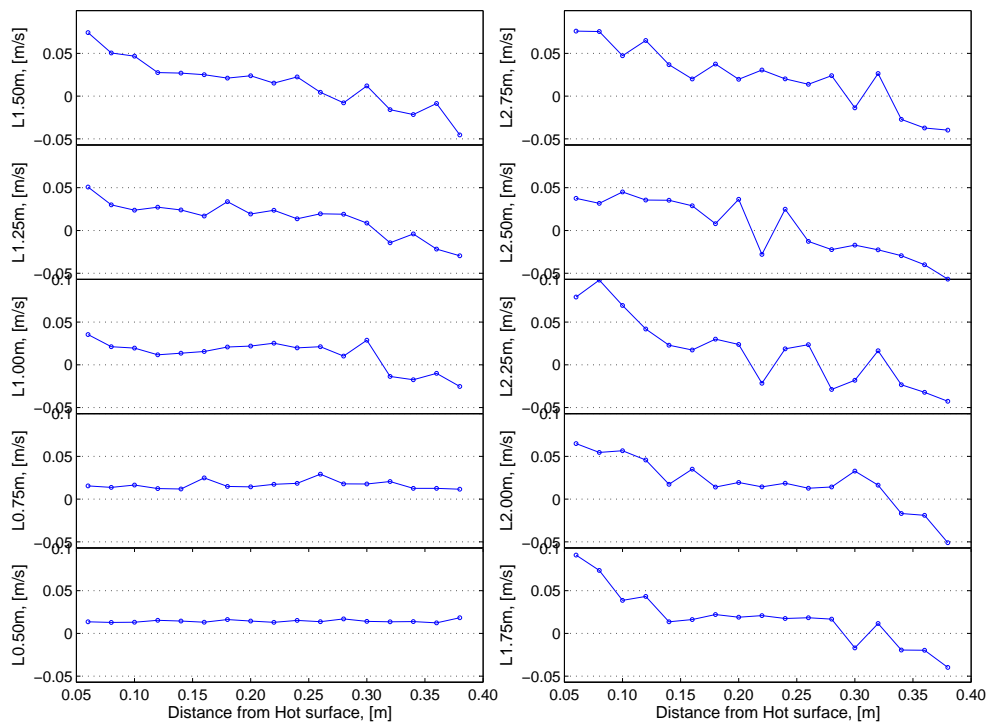


Figure F.1. Velocity distribution with height Exp. 8

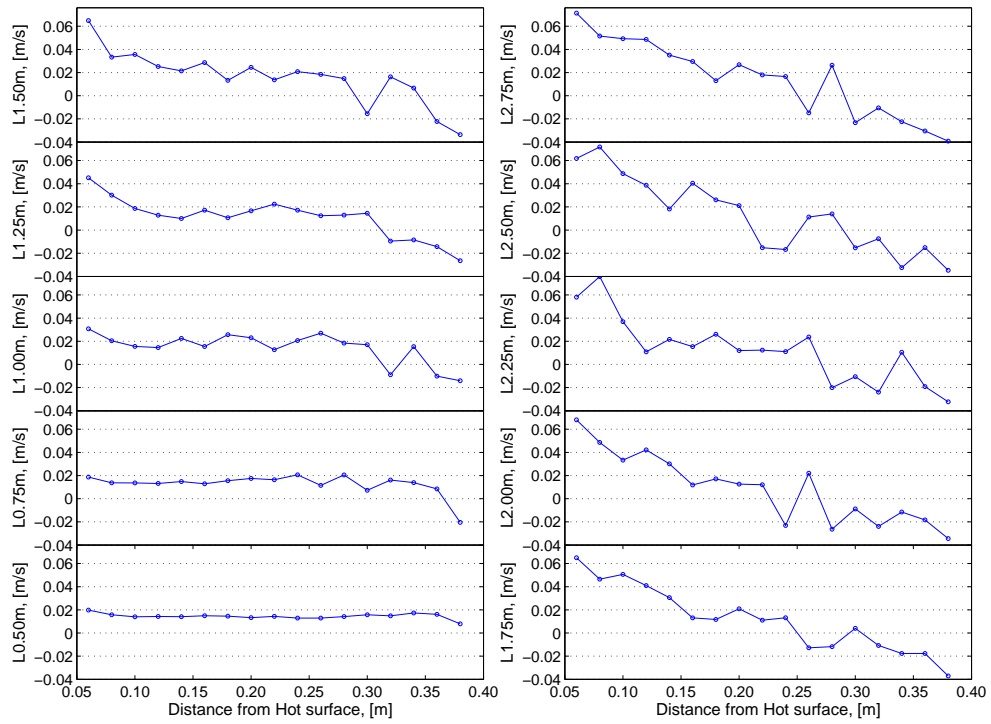


Figure F.2. Velocity distribution with height Exp. 9

F.2 Pressure difference

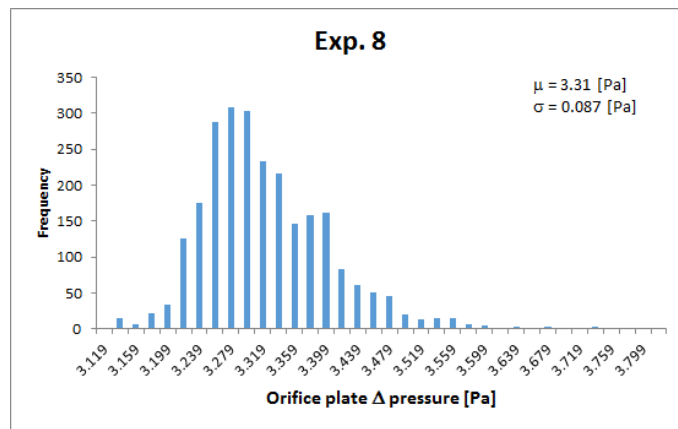


Figure F.3. Orifice pressure difference histogram Exp. 8

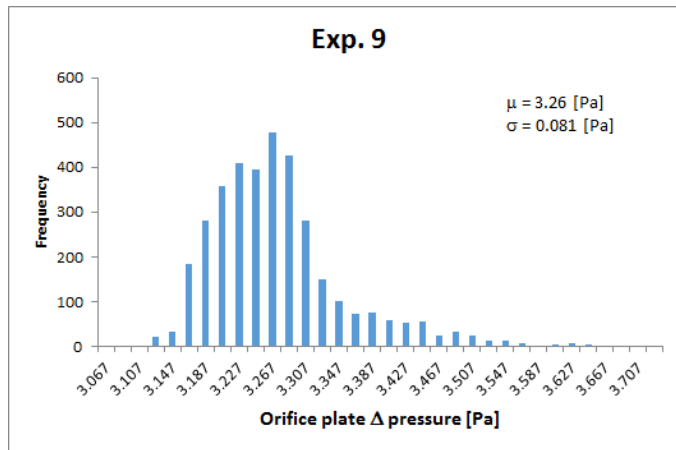


Figure F.4. Orifice pressure difference histogram Exp. 9

Dry air properties G

Table G.1. Properties of dry air used for calculations Rusev et al. [2002]

Temperature	Density, (ρ)	Specific heat capacity, (C_p)	Thermal conductivity (k)	Diffusivity of air (α)	Dynamic viscosity (μ)	Kinematic viscosity (ν)	Prandtl number
[°C]	[kg/m^3]	[$J/(kg.K)$]	[$W/(m.K)$]	[m^2/s]	[$N, s/m^2$]	[m^2/s]	-
-50	1,584	1013	2,04	1,27E-05	1,46E-05	9,23E-06	0,728
-40	1,515	1013	2,12	1,38E-05	1,52E-05	1,00E-05	0,728
-30	1,453	1013	2,2	1,49E-05	1,57E-05	1,08E-05	0,723
-20	1,395	1009	2,28	1,62E-05	1,62E-05	1,16E-05	0,716
-10	1,342	1009	2,36	1,74E-05	1,67E-05	1,24E-05	0,712
0	1,293	1005	2,44	1,88E-05	1,72E-05	1,33E-05	0,707
10	1,247	1005	2,51	2,01E-05	1,76E-05	1,42E-05	0,705
20	1,205	1005	2,59	2,14E-05	1,81E-05	1,51E-05	0,703
30	1,165	1005	2,67	2,29E-05	1,86E-05	1,60E-05	0,701
40	1,128	1005	2,76	2,43E-05	1,91E-05	1,70E-05	0,699
50	1,093	1005	2,83	2,57E-05	1,96E-05	1,80E-05	0,698
60	1,06	1005	2,9	2,72E-05	2,01E-05	1,90E-05	0,696
70	1,029	1009	2,96	2,86E-05	2,06E-05	2,00E-05	0,694
80	1,000	1009	3,05	3,02E-05	2,11E-05	2,11E-05	0,692
90	0,972	1009	3,13	3,19E-05	2,15E-05	2,21E-05	0,69
100	0,946	1009	3,21	3,36E-05	2,19E-05	2,31E-05	0,688
120	0,898	1009	3,34	3,68E-05	2,28E-05	2,55E-05	0,686
140	0,854	1013	3,49	4,03E-05	2,37E-05	2,78E-05	0,684
160	0,815	1017	3,64	4,39E-05	2,45E-05	3,01E-05	0,682
180	0,779	1022	3,78	4,75E-05	2,53E-05	3,25E-05	0,681

Electronic appendix **H**

In the electronic appendix can be found the following folders, which contain the plots and video files for all experiments.

- Experimental videos
- Horizontal temperature distributions
- Pressure difference plots
- Temperature contour plots
- Turbulence plots
- Velocity multi-levels
- Velocity contour plots
- Velocity fluctuation plots
- Velocity stability plots
- Velocity vector plots
- Vertical temperature distributions